

<https://doi.org/10.15388/vu.thesis.553>

<https://orcid.org/0000-0003-1949-6256>

VILNIUS UNIVERSITY

CENTER FOR PHYSICAL SCIENCES AND TECHNOLOGY

Darius Budrevičius

Synthesis and Characterisation of Lanthanide Phosphates for Biomedical Applications

DOCTORAL DISSERTATION

Natural Sciences,
Chemistry (N 003)

VILNIUS 2023

The dissertation was prepared between 2018 and 2023 (Vilnius University).

Academic supervisor – Prof. Dr. Ramūnas Skaudžius (Vilnius University, Natural Sciences, Chemistry – N 003).

This doctoral dissertation will be defended in a public meeting of the Dissertation Defence Panel:

Chairman – Assoc. Prof. Dr. Justina Gaidukevič (Vilnius University, Natural Sciences, Chemistry – N 003).

Members:

Prof. Dr. Kęstutis Baltakys (Kaunas University of Technology, Technological Sciences, Chemical Engineering – T 005),

Assoc. Prof. Dr. Inga Grigoravičiūtė (Vilnius University, Natural Sciences, Chemistry – N 003),

Prof. Dr. Rasa Pauliukaitė (Centre for Physical Sciences and Technology, Natural Sciences, Chemistry – N 003),

Dr. Sigita Trabesinger (Paul Scherrer Institut, Switzerland, Natural Sciences, Chemistry – N 003).

The dissertation shall be defended at a public/closed meeting of the Dissertation Defence Panel at 15 p.m. on 17 November 2023 in Inorganic Chemistry auditorium 141 of the Institute of Chemistry, Faculty of of Chemistry and Geoscience, Vilnius University.

Address: Naugarduko street 24, LT-03225 Vilnius, Lithuania

Tel. +370 52193105; e-mail: info@chgf.vu.lt

The text of this dissertation can be accessed at the libraries of Vilnius University and Center for Physical Sciences and Technology, as well as on the website of Vilnius University:

www.vu.lt/lt/naujienos/ivykiu-kalendorius

<https://doi.org/10.15388/vu.thesis.553>

<https://orcid.org/0000-0003-1949-6256>

VILNIAUS UNIVERSITETAS
FIZINIŲ IR TECHNOLOGIJOS MOKSLŲ CENTRAS

Darius Budrevičius

Lantanoidų fosfatų sintezė ir apibūdinimas biomedicinos tikslais

DAKTARO DISERTACIJA

Gamtos mokslai,
Chemija (N 003)

VILNIUS 2023

Disertacija rengta 2018 – 2023 metais Vilniaus universitete.

Mokslinis vadovas – prof. dr. Ramūnas Skaudžius (Vilniaus universitetas, gamtos mokslai, chemija – N 003)

Gynimo taryba:

Pirmininkė – **asoc. prof. dr. Justina Gaidukevič** (Vilniaus universitetas, gamtos mokslai, chemija – N 003).

Nariai:

prof. dr. Kęstutis Baltakys (Kauno technologijos universitetas, technologijos mokslai, chemijos inžinerija – T 005),

asoc. prof. dr. Inga Grigoravičiūtė (Vilniaus universitetas, gamtos mokslai, chemija – N 003),

prof. dr. Rasa Pauliukaitė (Fizinių ir technologijos mokslų centras, gamtos mokslai, chemija – N 003),

dr. Sigita Trabesinger (Paul Scherrer institutas, Šveicarija, gamtos mokslai, chemija- N003).

Disertacija ginama viešame Gynimo tarybos posėdyje 2023 m. lapkričio mėn. 17 d. 15 val. Vilniaus universiteto Chemijos ir geomokslų fakulteto Neorganinės chemijos auditorijoje.

Adresas: Naugardukog. 24, LT-03225,

Vilnius, Lietuva tel. +37052193108 ; el. paštas info@chgf.vu.lt.

Disertaciją galima peržiūrėti Vilniaus universiteto bei Fizinių ir technologijos mokslų centro bibliotekose ir VU interneto svetainėje adresu:

<https://www.vu.lt/naujienos/ivykiu-kalendorius>

LIST OF SYMBOLS AND ABBREVIATIONS

BET	Brunauer, Emmet, and Teller
BJH	Barrett, Joyner, and Halenda
CIE	Commission internationale de l'éclairage (International commission on illumination)
DMEM	Dulbecco's modified eagle medium
DOX	Doxorubicin hydrochloride
EDAX	Energy dispersive X-ray analysis
EMR	Electromagnetic radiation
EOG	Ethylene oxide gas
FBS	Fetal bovine serum
ICDD	International Centre for Diffraction Data
ICP-MS	Inductively coupled plasma mass spectrometry
IR	Infrared
IUPAC	International Union of Pure and Applied Chemistry
LED	Light emitting diode
Ln	Lanthanide
MCSAP-	Mono-capped square antiprism
MEM	Minimum essential medium eagle
MRI	Magnetic resonance imaging
MTT	3-(4,5-dimethylthiazol-2-yl)-2,5- diphenyltetrazolium bromide
NC	Negative control
NIR	Near infrared
NPL	National physics laboratory
PDF	Powder Diffraction File
PVP	Polyvinyl pyrrolidone
RE	Rare earth elements
REPO ₄	Rare earth phosphate
RM	Positive control
SEM	Scanning electron microscope
UV	Ultraviolet
XRD	X-ray diffraction
YAG	Yttrium aluminum garnet

TURINYS

INTRODUCTION.....	8
1. LITERATURE REVIEW.....	12
1.1. Crystal structures of materials.....	12
1.1.1. Crystal structure of rare-earth orthophosphates.....	13
1.1.2. Structure of GaPO ₄ doped with rare earth metals.....	15
1.2. Synthesizes methods of lanthanide orthophosphate nanoparticles.....	17
1.2.1. Sol-Gel synthesis methods.....	17
1.2.2. Sonochemical synthesis methods.....	19
1.2.3. Co-precipitation synthesis methods.....	21
1.2.4. Microwave-assisted hydrothermal synthesis methods.....	23
1.2.5. Solvothermal and hydrothermal synthesis methods.....	26
1.3. Basic of luminescence.....	29
1.3.1. Luminescences property of lanthanide orthophosphate.....	30
1.3.2. Luminescent application of lanthanide orthophosphate.....	32
1.3.3. Environmental application of lanthanide orthophosphate.....	34
1.3.4. Magnetic applications of lanthanide orthophosphate.....	36
2. EXPERIMENTAL PART.....	39
2.1. Chemicals and Reagents.....	39
2.1.1. Materials used for the synthesis.....	39
2.1.2. Control material of the cytotoxicity study.....	39
2.2. Synthesis and Processing.....	39
2.2.1. Synthesis and Processing of GdPO ₄ :15%Eu samples.....	39
2.2.2. Synthesis and Processing of Gd _{1-x} Eu _x PO ₄ and Gd _{1-x} La _x PO ₄ :15%Eu samples.....	40
2.2.3. Preparation of the extract and cytotoxicity test.....	41
2.2.4. Cytotoxicity test.....	41
2.3. Characterization Techniques.....	41
3. RESULTS AND DISCUSSIONS.....	43

3.1. Investigation of the optimal europium concentration in $Gd_{1-x}Eu_xPO_4 \cdot H_2O$	43
3.2. Investigation of the dependence of the $Gd_{0.85}Eu_{0.15}PO_4 \cdot H_2O$ nanoparticle size on the reactor volume	47
3.3. Effect of doping by lanthanum on structure and luminescence properties of $Gd_{0.85-y}La_yPO_4:15\%Eu$	53
3.4. Biological evaluation of $Gd_{0.85-y}La_yPO_4:15\%Eu$ samples	58
3.5. Investigation of synthesis conditions of monoclinic structure $Gd_{0.85-y}La_yPO_4:15\%Eu$ and study of luminescent properties.....	60
CONCLUSIONS.....	72
REFERENCES.....	73
SUMMARY IN LITHUANIAN	87
ACKNOWLEDGEMENTS	117
LIST OF PUBLICATIONS AND CONFERENCES PARTICIPATION..	118
CURRICULUM VITAE.....	119

INTRODUCTION

Due to the strong paramagnetic nature of gadolinium, Gd-based materials are commonly used in medicine as a magnetic resonance contrast agent and in other areas [1,2]. However, the use of some commercial chelated gadolinium contrast agents on patients with kidney problems was restricted by the World Health Organization back in 2009. It is because Gd^{3+} ions are highly toxic and, even in chelated form, there still is a risk of Gd^{3+} release into an organism [3,4]. While MRI is a powerful technique used for medical diagnosis, still new ways of improving imaging are needed. To improve the quality of the MRI, materials are being developed and are already being used to obtain T1 and T2 MRI together, as single-mode MRI does not always provide sufficient image quality. Multimodal materials suitable for bioimaging and MRI are also being developed. One such way is to combine the MRI with Luminescence measurements. Even now the development of materials suitable for multimodal imaging is being pursued. However, this is quite a difficult task, as materials that are used for medical purposes must fit extremely strict criteria. It is very important that materials used in medicine are non-toxic and biocompatible. While Gd^{3+} ions are known to be toxic to humans, some leeching was observed in the Gd-based complex compounds used as MRI contrast agents. $GdPO_4$ nanoparticles are non-toxic because Gd^{3+} ions are much less likely to be released into the human body [5]. Additionally, lanthanoids are suitable for the doping of $GdPO_4$ nanoparticles. Doping by europium particularly results in emission at ~ 577 nm, ~ 590 nm, ~ 615 nm, ~ 650 , and ~ 700 nm wavelengths and when considering the interest of the compounds for bioimaging it is quite desirable, since part of the emission, in this case, exist in a so-called first biological window, and is absorbed by the tissue to a much lesser extent [6]. Thus, Eu-doped $GdPO_4$ nanoparticles attract a lot of attention as an efficient single-phase multimodal nanoprobe with both luminescent and magnetic properties [7,8].

However, while europium is quite commonly used as a dopant in the preparation of various compounds as it exhibits excellent luminescence properties, even when it is introduced even at small concentrations, further optimization, and investigation are required. This is due to the fact that if the concentration of light emitting dopant introduced into the crystal structure is too large concentration quenching is often observed. In the case of europium, this boundary can change drastically depending on the initial host matrix. In the case of single-crystalline scintillator $Ca_2MgSi_2O_7$, the optimal concentration of doped Eu^{3+} is 10% for the most intensive photoluminescence and scintillation properties [9] and for $LiCaAlF_6:Eu$

single crystals optimal doping concentration of Eu^{3+} ion is 2% - 2.5% range [10]. Meanwhile, the most intense luminescence for magnetic dipole transition (${}^5\text{D}_0 \rightarrow {}^7\text{F}_1$) of Eu^{3+} doped GdPO_4 nanoparticles which were prepared by ethylene glycol route and subsequently heated is obtained at a concentration range of 5-7% of Eu^{3+} [11]. Furthermore, irrespective of the crystalline environment, the Eu^{3+} ion usually emits red light under UV excitation, however, there have been reports that in certain situations weak emission bands can also be obtained in the green and sometimes blue range [12–15]. It should be also noted that the intensity of luminescence also depends on the particle size and the length-to-width ratio, particle shape, and crystalline structure [16,17]. Additionally, particle shape is also important for potential practical applications. Recently, urchin-like $\text{GdPO}_4 \cdot \text{H}_2\text{O} : 5\text{Eu}^{3+}$ nanoparticles have been shown to penetration capability A549 lung cancer cells, exhibiting luminescence [18]. Even the scientists put efforts to determine the optimal concentration of Eu^{3+} for GdPO_4 samples, it is still an area of interest should be solved.

As mentioned before the crystal structure and particle morphology of the host lattice are very important to obtain high intensity luminescence. Recently it has been reported that 5% Eu^{3+} doped GdPO_4 nanoparticles with monoclinic crystalline structures have better luminescence properties as compared to nanoparticles with hexagonal or nanowires with monoclinic and hexagonal crystal structures [19]. Eu^{3+} doped GdPO_4 samples synthesized in a water medium all exhibited hexagonal crystalline structure which is stabilized by the incorporation of crystalline water, while the synthesis in an anhydrous medium yielded GdPO_4 nanoparticle with a monoclinic structure due to the absence of water. Samples synthesized in the anhydrous medium showed a more intense luminescence, which may have resulted from the difference in the crystal lattice. If the Eu^{3+} doped GdPO_4 nanoparticle with a hexagonal crystal structure is heated above 700 °C degrees, water is removed, and the crystal structure changes to monoclinic resulting in increased luminescence intensity. However, in this case not only the crystal structure is changed but most likely also the crystallinity and the size of the particles of the samples, as such it is difficult to attribute the improvement of luminescence properties to one of these phenomena, as they all can affect it [20]. Furthermore, in most cases it is not desirable to anneal the samples, as it leads to particle size growth and the preparation in anhydrous mediums can be complicated, as such over ways of changing the crystal structure are needed. It is known that lanthanum phosphate can be obtained in two crystalline structures: a hydrated hexagonal rhabdophane type and a monoclinic monazite-type [21]. The monazite-type Eu^{3+} , Tb^{3+} -co-doped

LaPO₄·nH₂O nanorods demonstrate higher photoluminescent efficiency than the LaPO₄·nH₂O rhabdophane-type nanorods co-doped with the same amount of Eu³⁺, Tb³⁺ [22]. It is known that the most common GdPO₄ nanoparticles are the hydrates meanwhile LaPO₄ are more commonly found in anhydrate. Stabilizing monoclinic anhydrate of GdPO₄ by La³⁺ ions could lead to the improvement of the luminescent properties of phosphor in general.

Taking all this into account, in the present research we investigate the optimal concentration of Eu³⁺ resulting in more intensive emission of the samples and Gd³⁺ ions as well as attempt to stabilize the monoclinic monazite type structure by means of La³⁺ doping and analyze their effects on crystal structure, luminescence properties, and cytotoxicity.

The aim is to develop an anhydrous of lanthanide phosphate with magnetic properties that can be used for multimodal imaging.

The tasks of this research are the following:

- to determinate and investigate the optimal Eu³⁺ concentration;
- to control the size of nanoparticles and to investigate nano parts' size effect on luminescence;
- to carry out the synthesis of Eu³⁺-doped GdPO₄ nanoparticles to obtain the desired crystal structure;
- to characterize the crystal structure, luminescence properties, magnetic behavior, toxicity of the synthesized particles.

Various characterization techniques, such as X-ray diffraction, spectroscopy, and magnetic measurements, have been employed in this research. We have analyzed the effect of particle size, length-to-width ratio, shape, and crystalline structure on the luminescence properties of the nanoparticles. We have explored controlling these particle characteristics to enhance the performance of the nanoparticles for bioimaging applications. The cytotoxicity of the Eu³⁺-doped GdPO₄ nanoparticles has been evaluated to ensure their biocompatibility and non-toxicity. This analysis is crucial for determining the suitability of the nanoparticles for biomedical applications.

Overall, the research has aimed to contribute to the development of lanthanide phosphate nanoparticles with optimized luminescent and magnetic properties for use in multimodal bioimaging, while also considering their crystal structure, particle morphology, and potential cytotoxicity.

Novelty and originality of the work:

The novelty of this research is that the optimal amount of Eu^{3+} for GdPO_4 nanoparticles synthesized by the hydrothermal method was determined to obtain maximum luminescence emission intensity. It was also demonstrated for the first time that the size of nanoparticles of $\text{Gd}_{0.85}\text{Eu}_{0.15}\text{PO}_4 \cdot \text{H}_2\text{O}$ can be controlled by varying the filling volume of the hydrothermal reactor. For the first time, by hydrothermal synthesis, without using additional processing of the material after synthesis (heating), it was obtained single-phase monoclinic crystal structure of $\text{La}_{0.61}\text{Gd}_{0.24}\text{PO}_4:15\%\text{Eu}$ and $\text{La}_{0.75}\text{Gd}_{0.1}\text{PO}_4:15\%\text{Eu}$.

Statement for defense:

- In order to achieve the best luminescence properties of nanoparticles of gadolinium phosphate, the amount of doped Eu^{3+} is 15%.
- The size of the Eu^{3+} doped GaPO_4 nanoparticles depends on the filling volume of the hydrothermal reactor.
- During synthesis in a hydrothermal reactor, the PO_4^{3-} precursor affects the final product, its crystalline structure and morphology.

The particles synthesized in this work have both magnetic and luminescent properties and are non-toxic, so have the potential to be used for multimodal imaging.

1. LITERATURE REVIEW

1.1. Crystal structures of materials

Before starting the discussion about the structure of the material studied in this research, the basics should be remembered. We often find symmetry in the environment around us. Consideration of symmetry often simplifies complex matters, including problems related to molecular structure. In the sense of mathematical symmetry, a molecule has symmetry if it has two or more orientations in space that are inseparable, and the criteria for evaluating them are based on symmetry elements and symmetry operations. The symmetry of a molecule can be point, axis, or mirror plane, when the molecule is moved about a point, axis, or plane to a position that is indistinguishable from its original position. When we analyze the symmetry elements of a molecule, usually we will find more than one symmetry element, (axis of symmetry, plane of symmetry) the set of these symmetry elements is called a symmetry group or point group. Symmetry groups can be divided. The point groups with a large number of characteristic symmetry elements are groups with very high symmetry. Groups with low symmetry are that possess only one or two symmetry elements. When we have a molecule that has symmetry only the n -fold axis of rotation, such groups are called: groups with an n -fold rotational axis, C_n . If, in addition to the C_n axis, there is a horizontal plane perpendicular to that axis, the molecule is said to have C_{nh} symmetry. If the molecule has an nC_2 axis perpendicular to the principal axis (C_n), and then they are classified as dihedral groups. There are no mirror planes, then the molecule belongs to group D . If there is a mirror plane perpendicular to the main axis results in the D_{nh} groups [23,24].

Crystal symmetry is not only the symmetry of individual point groups of the molecules that make up the crystals, but also the translational symmetry of these molecules in the crystal. In the simplest case, if we took a repeating row of identical points, and we would consider the point to be a lattice point, it could be called a one-dimensional crystal. Likewise, in a three-dimensional crystal, a stacked array of unit cells, the repeating units of the system display translational symmetry. In crystallography the most straightforward array of points from which a crystal can be created is called a unit cell. There are a total of seven basic shapes of unit cells. They all consist of parallelepipeds with six side-parallel pairs. Crystal systems, based on their characteristic symmetry and relationships between the unit cell edges and angles of the crystal, are divided into: triclinic, monoclinic, orthorhombic, tetragonal, trigonal, hexagonal, cubic. Space lattices (Bravais

lattices) are assigned to these crystal systems: P (primitive), I (body-centered), F (face-centered), C (face-centered in one set of faces), and R (rhombohedron). A total of fourteen Bravio cells are possible [24,25].

1.1.1. Crystal structure of rare-earth orthophosphates

The rare earth phosphate minerals, which have a general formula of $REPO_4 \cdot nH_2O$, belong to four different structural types, mainly depending on their hydration level and the atomic mass of the included rare earth elements (i.e. light or heavy RE) [26]. Among them, monazite $LnPO_4$ (hexagonal, $P2_1/n$), typically crystallizing with $Ln = La-Tb$ [23], is probably the most widespread in nature and therefore well-documented. Monazite is one of the main ores used for lanthanide extraction and naturally contains high amounts of uranium and thorium (up to 15% by mass), mostly due to substitutions with divalent elements such as calcium [27]. For heavy rare earth elements, i.e. $Ln=Gd-Lu$, as well as yttrium and scandium, the anhydrous $LnPO_4$ phase adopts a zircon-type structure (tetragonal, $I41/amd$) [28], forming xenotime. The latter often coexists with monazite in granitic and metamorphic rocks [29]. On the other hand, minerals with hydrated counterparts are not commonly found in nature. Rhabdophane $LnPO_4 \cdot 0.667H_2O$ (monoclinic, $C2$) [30], which is a hydrated form of rare-earth phosphate, is mostly found in the upper part of the earth's crust and is less stable than monazite [30]. Therefore, rhabdophane is frequently present in bauxite, laterites, and hydrothermal systems as one of the main carriers of light rare-earth elements, while monazite dominates in silicic rocks that are magmatic and metamorphic in origin [31]. Churchite, with the ideal formula $YPO_4 \cdot 2H_2O$ (monoclinic, isostructural to gypsum), is most commonly reported to contain heavy rare-earth elements like dysprosium and erbium. It is found in association with limonite deposits and laterites [32].

The crystal structure of rare-earth orthophosphates varies depending on the size of the rare earth element and the temperature and pressure conditions during synthesis. Generally, $REPO_4$ compounds adopt a tetragonal crystal structure with the space group $I41/amd$, which belongs to the zircon structure type.

In the crystal structure, each rare earth ion is coordinated to eight oxygen atoms, forming a distorted cube-like structure known as a rare earth oxide polyhedron. Each phosphate ion (PO_4^{3-}) is tetrahedrally coordinated to four oxygen atoms, with each oxygen atom shared with a neighboring tetrahedron, forming a three-dimensional network. The rare earth oxide

polyhedra and PO_4^{3-} tetrahedra share oxygen atoms, linking together to form the overall crystal structure.

The specific arrangement of the rare earth oxide polyhedra and PO_4^{3-} tetrahedra in the crystal structure depends on the size of the rare earth element. Larger rare earth ions, such as cerium and yttrium, tend to form more distorted polyhedra, resulting in a lower symmetry crystal structure.

Rare-earth orthophosphates have a variety of properties, including high thermal stability, chemical resistance, and luminescent behavior, which make them useful in a range of applications, such as in solid-state lighting, phosphors, and catalysts. The crystal structure of these materials is important for understanding their properties and potential applications. Rare earth phosphates constitute a class of inorganic compounds containing a rare earth element (e.g., cerium, neodymium, or europium) along with phosphorus (P) and oxygen (O). The structural and property variations of rare earth phosphates arise from the specific rare earth element and synthesis conditions. Orthophosphates composed of PO_4^{3-} tetrahedra, manifest as natural apatites and monazites. Lanthanoid phosphates serve as excellent host matrices for other lanthanoid ions, facilitating the creation of diverse luminescent colors [33]. These phosphates possess favorable matrix characteristics, including low synthesis temperatures, high luminescence efficiency, economical raw materials, and robust stability [34]. Lanthanoid orthophosphates, marked by distinct electronic, magnetic, and optical properties mainly attributed to the lanthanoid element [35], exhibit four crystal structures: hexagonal, tetragonal, orthorhombic, and monoclinic. Their chemical formula is expressed as $\text{LnPO}_4 \cdot n\text{H}_2\text{O}$, where $n = 0-3$, and Ln^{3+} represents the lanthanoid ion [36]. While the oxidation state of lanthanoid elements generally stands at +3, selected lanthanides, like Sm, Eu, Tm, and Yb, can be reduced to +2, and others, such as Ce, Pr, Nd, Tb, and Dy, can be oxidized to +4. The novel hexagonal structure of lanthanide phosphates constitutes a low-temperature phase that can transition to a monoclinic phase at higher temperatures, whereas the tetragonal phase maintains its structure after heating to 900 °C. pH adjustments in the synthesis medium allow control over this phase transition. Lanthanoid orthophosphates, characterized by minimal water solubility and high thermal stability [37], have their structure influenced by the ionic radius of the lanthanoids. For instance, ionic radii pertinent to this study include 1.160 Å (lanthanum), 1.066 Å (europium), and 1.053 Å (gadolinium) [38]. The crystal structure of pure lanthanoid orthophosphates experiences changes as the ionic radius of Ln decreases, resulting in a hexagonal structure for lanthanoids from La to Dy following hydrothermal treatment, and a

tetragonal structure for lanthanoids from Ho to Lu and Y. Heat treatment at high temperatures (900 °C) can transform synthesized hexagonal crystal structure orthophosphates of lanthanides into products characterized by a monoclinic crystal structure [37,39].

1.1.2. Structure of GaPO₄ doped with rare earth metals

Lanthanide orthophosphates exist in five polymorphic form namely, monazite (monoclinic structure), xenotime (tetragonal structure), rhabdophane (hexagonal structure), churchite (monoclinic) and orthorhombic symmetries. [40], It is known that only Gd and Lu with Y can be obtained, crystallized in all four crystalline phases, depending on various conditions [41,42].

The crystal structure of GdPO₄ is in the monoclinic space group P2₁/n, with a single Gd³⁺ ion and one PO₄³⁻ anion in the asymmetric unit. The phosphate anion is tetrahedrally coordinated without any significant distortion, while the Gd³⁺ ion is nine-coordinate and best described as a severely distorted mono-capped square antiprism. The arrangement of polyhedra in the crystal structure is complex but can be described as chains of alternating PO₄³⁻ and GdO₉ polyhedra, which are parallel to the [100] direction in the standard P2₁/n setting. These chains are cross-linked via bridging oxygen atoms between the Gd³⁺ ions, resulting in each Gd³⁺ being coordinated to seven PO₄³⁻ tetrahedra, with five of them vertex-sharing and the remaining two edge-sharing. Additionally, each Gd³⁺ ion shares common edges with six neighboring Gd³⁺ cations [43].

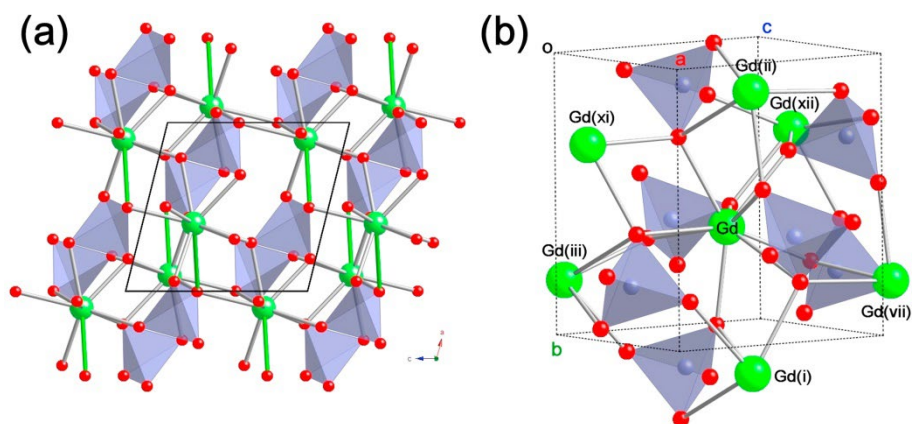


Fig. 1. (a)The crystal structure of GdPO₄ as viewed along the [010] direction; (b) the secondary coordination sphere of the Gd³⁺ ion in GdPO₄.

Each ion is coordinated to seven PO_4^{3-} tetrahedra and has six edge-sharing interactions with neighboring Gd^{3+} ions. Green: Gd; red: O; light grey: P. Green struts represent the bond between Gd^{3+} ions and the capping oxygen atoms of the MCSAP, all other covalent bonds are shown in grey [43].

The rhabdophane phase is attributed a hexagonal structure with a space group of P6_622 , but later it was revised to be trigonal P3_121 . However, in the literature and reference books, GdPO_4 with the P3_121 space group is assigned and referred to as a hexagonal crystal structure. In this structure, each Gd^{3+} ion is bonded to 8 oxygen atoms of a phosphate group, forming GdO_8 polyhedrons. These polyhedrons share their edges with four other GdO_8 polyhedrons and two PO_4^{3+} tetrahedrons, creating a building block. The trigonal rhabdophane structure consists of infinite chains of these building blocks and phosphate tetrahedrons that are connected together along the c axis, forming zeolitic channels that also run along the c axis. These channels are known to contain crystalline water.

The crystal structures of churchite materials ($\text{REPO}_4 \cdot 2\text{H}_2\text{O}$; RE = Gd to Lu) were determined through powder X-ray diffraction after being synthesized through a low-temperature precipitation route. The results showed that churchite materials crystallize in the monoclinic crystal system (space group C2/c). The enthalpies of formation of churchite-type $\text{REPO}_4 \cdot 2\text{H}_2\text{O}$ (RE = Gd to Yb) were found to be more negative than their anhydrous counterparts, which have a xenotime structure. This suggests that the formation of churchite is more exothermic than xenotime. However, due to the presence of water molecules, the churchite materials are likely to have a more negative entropy of formation, resulting in a less negative Gibbs free energy of formation than the xenotime structure. This implies that churchite materials are expected to be stable at lower temperatures. For GdPO_4 and $\text{GdPO}_4 \cdot n\text{H}_2\text{O}$ materials, which could adopt different crystal structures, monazite was found to have the most negative Gibbs free energy of formation from oxides. This suggests that monazite is the most stable among the discussed structures, with the following order of stability : Gd-churchite < Gd-rhabdophane < Gd-xenotime < Gd-monazite [42].

The crystal structure of GaPO_4 doped with rare earth metals depends on the specific dopant and its concentration. In general, the dopant ions will substitute for Ga^{3+} ions in the GaPO_4 crystal lattice, introducing defects or distortions in the crystal structure. When Eu^{3+} ions are doped into GaPO_4 , the crystal structure the unit cell parameters and angles may change slightly. The Eu^{3+} ions occupy substitutional sites in the crystal lattice, replacing some of the Ga^{3+} ions. The Eu^{3+} ions have a slightly larger ionic radius (1.07

Å) than the Ga³⁺ ions (1.06 Å) [38], which can cause local distortions in the crystal lattice around the dopant ion.

The GdPO₄ can exist in various crystal structures, including hexagonal, tetragonal, and monoclinic, depending on synthesis factors such as solution acidity, solvent, and/or annealing temperature. The transformation of hexagonal GdPO₄ nanorods to monoclinic or obtaining monoclinic GdPO₄ nanoparticles has considerable attention due to the strong correlation between the optical properties of GdPO₄:Eu³⁺ and the symmetry around Eu³⁺ and crystal structure [44].

The incorporation of rare earth metals into GdPO₄ can modify the properties of the material, such as its optical and magnetic properties. For example, rare earth-doped GdPO₄ can exhibit luminescent behavior, making it useful in applications such as phosphors, solid-state lighting, and optical devices [45–48]. The crystal structure of GdPO₄ doped with rare earth metals is important for understanding how these materials interact with light and other substances and for optimizing their performance in various applications. The specific crystal structure of GdPO₄ doped with rare earth metals will depend on the specific dopant and its concentration, as well as the synthesis conditions and post-treatment methods used to prepare the material [49–52].

Overall, the crystal structure and chemical stability of GdPO₄ make it a versatile platform for doping with a range of elements, including rare earth metals, and tailoring its properties for various applications. It should be noted that the luminescence properties of Eu³⁺-doped GdPO₄ depend on the crystal structure. Studies have shown that the emission intensity of Eu³⁺-doped GdPO₄ with a monoclinic crystal structure is significantly higher compared to that of Eu³⁺-doped GdPO₄ with a hexagonal crystal structure [46,53,54]. Therefore, to obtain the best luminescent properties of Eu³⁺-doped GdPO₄, the synthesis of pure-phase monoclinic crystal structure nanoparticles is the primary objective.

1.2. Synthesizes methods of lanthanide orthophosphate nanoparticles

1.2.1. Sol-Gel synthesis methods

Sol-gel synthesis is a versatile method used to produce inorganic materials, including nanoparticles, with controlled composition, size, and morphology. The sol-gel process involves the conversion of a solution or "sol" of metal-organic compounds or metal salts into a gel-like state by a

hydrolysis and condensation reaction. The resulting gel can then be dried and calcined to form a solid material, including nanoparticles.

The sol-gel synthesis method involves several steps, preparation of precursor solution: In first step, metal-organic compounds or metal salts are dissolved in a solvent, typically an alcohol or water, to form a solution. The precursor solution is usually stabilized with a weak acid or base to prevent premature hydrolysis. In the second step, hydrolysis is carried out. The precursor solution is slowly mixed with a hydrolyzing agent, typically water or an acid or a base, to initiate the hydrolysis reaction. The hydrolysis reaction causes the metal-organic compounds or metal salts to form metal-oxygen bonds, resulting in the formation of a colloidal solution or "sol." As the hydrolysis reaction continues, the sol gradually transforms into a three-dimensional network or "gel" of metal-oxygen clusters. The gelation process can be influenced by several factors, such as pH, temperature, and the concentration of the precursor solution and hydrolyzing agent. After gelation, the resulting gel is left to age for several hours or days to allow further condensation and solidification of the metal-oxygen clusters. Drying and calcination are carried out in the last stage of synthesis. The aged gel is dried to remove the solvent and then calcined at high temperatures to remove any remaining organic components and form a solid material [55,56].

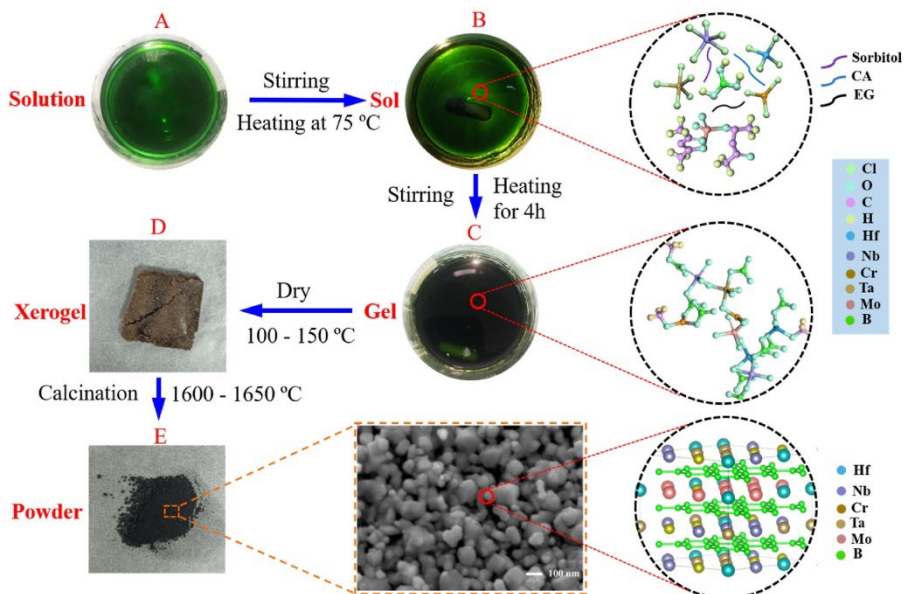


Fig. 2. Schematic illustration for the synthesis process of diboride powders via sol-gel method [57].

Sol-gel synthesis has several advantages for nanoparticle synthesis. The sol-gel method allows for precise control over the composition of the nanoparticles by adjusting the precursor solution composition and concentration. The sol-gel method can produce nanoparticles with controlled size and morphology by adjusting reaction parameters such as the concentration of precursor solution. The influence of the concentration of reactants on the morphology and size of lanthanum phosphate (LaPO_4) nanoparticles was examined and reported. The changes in nanoparticle shape were explained by the mechanism of spherical diffusion growth. It was observed that decreasing the reactant concentration, from high (100 mol/m^3) to very low (0.125 mol/m^3), resulted in a gradual transformation of nanoparticle morphology from long nanorods to nanospheres [58]. This synthesis method is also applicable for synthesizing doped nanoparticles. Previous reports have shown that the resulting LaPO_4 crystallizes in a single-phase monoclinic structure with rod-shaped nanoparticles of approximately 50 nm in length. The doping of europium ions into the monoclinic LaPO_4 crystal lattice was found to be highly effective using the same method. Additionally, these synthesis methods are simple, cost-effective, and can be easily extended to other rare earth phosphates [59]. Although the successful synthesis of nanoparticles by the sol-gel method and the ability to control the morphology of the particles are reported, the resulting particles are agglomerated and exhibit a large size dispersion [58–61]. It is worth noting that the reaction time is comparatively extended, and the use of organic solvents could pose risks to human health.

1.2.2. Sonochemical synthesis methods

Sonochemistry, which involves the use of high-frequency sound waves, has emerged as an effective method for synthesizing nanomaterials due to its ability to induce a range of physical and chemical phenomena such as cavitation, acoustic streaming, and high shear stress. Here are the general steps involved in sonochemical synthesis of lanthanide orthophosphate nanoparticles [62].

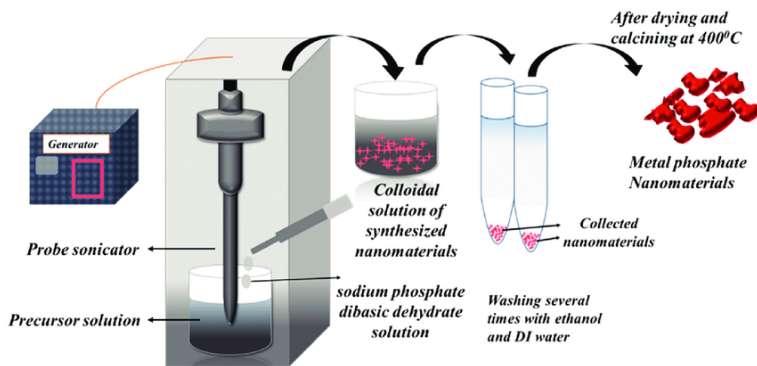


Fig. 3. Schematic representation for synthesis through sonochemical method [63].

Preparing a precursor solution, lanthanide and phosphate precursors (e.g. lanthanide nitrate and ammonium phosphate) are dissolved in a suitable solvent (e.g. water or ethanol) to form a clear solution. Sonochemical treatment, the precursor solution is subjected to ultrasonic irradiation using a high-frequency transducer, typically at a frequency of 20-100 kHz. The ultrasonic waves generate cavitation bubbles in the solution, which collapse to create high temperatures and pressures at the bubble-liquid interface, leading to rapid nucleation and growth of nanoparticles. After the sonochemical treatment, the solution is aged at room temperature for several hours to allow the nanoparticles to grow and stabilize. The nanoparticles are then washed with a solvent (e.g. water or ethanol) to remove any unreacted precursors or impurities. Finally, the nanoparticles are dried and calcined at high temperatures (e.g. 700-1000 °C) to remove any residual solvent and to stabilize the crystal structure of the nanoparticles [62,64–66].

The sonochemical process, a simple technique that can be carried out under ambient conditions, has been proven to be effective for obtaining novel materials and preparing nanomaterials with unique morphologies and unusual properties [65]. This process involves the propagation of pressure waves that generate bubbles in a liquid medium through formation, growth, and implosive collapse. These bubbles create localized hotspots with extreme conditions such as high temperatures (>5000 K), pressures (>20 MPa), and cooling rates (10^{10} Ks $^{-1}$) during acoustic cavitation. As a result, sonication provides an ideal environment for the preparation of nanomaterials. This method offers several advantages, including rapid reaction rates, controllable reaction conditions, and the ability to produce materials with uniform shapes, narrow size distributions, and high purities. Uniform nanoparticles of various lanthanide orthophosphates (LnPO $_4$),

including La, Ce, Pr, Nd, Sm, Eu, Gd, Tb, Dy, and Ho, have been successfully synthesized using a simple and efficient method involving ultrasonic irradiation of inorganic salt aqueous solution without the need for surfactants or templates. This synthesis process is fast, facile, and conducted under ambient conditions [64,66].

Sonochemical synthesis has several advantages over conventional synthesis methods, such as lower reaction times, reduced energy consumption, and improved control over particle size and morphology. However, the method requires specialized equipment and careful optimization of reaction parameters such as precursor concentration, sonication time and intensity, and aging time to achieve optimal results.

1.2.3. Co-precipitation synthesis methods

As one of the most classical wet chemical synthetic method, co-precipitation refers to the simultaneous precipitation process of several ions, with the formation of target nanosized compounds. Despite the easy operation, particular attention should be paid to the precipitation rate difference of various ions. To address the problem, coordinating surfactants and/or cosolvents are usually added into the reaction system to mediate the synchronicity of coprecipitation process. Co-precipitation synthesis can be performed in aqueous solution and organic solution. It is important to note that nanoparticles synthesized through co-precipitation in aqueous solution often exhibit relatively low crystallinity [67]. Subsequent heat treatment is commonly required to enhance the crystallinity of the final products. Co-precipitation synthesis is a versatile and widely used method for the preparation of various types of nanoparticles. The method involves simultaneous precipitation of two or more metal ions in the presence of a precipitating agent, usually a base such as sodium hydroxide or ammonium hydroxide. The process can be performed under various conditions, such as temperature, pH, and stirring rate, which can affect the properties of the resulting nanoparticles [68].

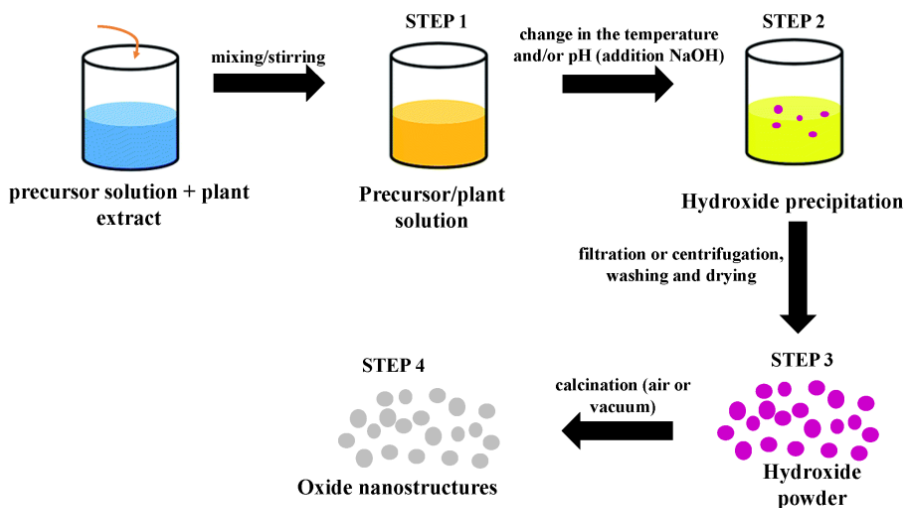


Fig. 4. Schematic diagram of the co-precipitation method [69].

The co-precipitation synthesis method contains several steps. The first step is preparation of precursor solutions. The metal salts are dissolved in a solvent to form a precursor solution. The solvent used can be water or an organic solvent, depending on the solubility of the metal salts. The second step is an addition of precipitating agent. The precipitating agent is added to the precursor solution under controlled conditions such as temperature, pH, and stirring rate. The addition of the precipitating agent induces the formation of a gel-like precipitate. After that the aging is the following step. The precipitate is aged at a certain temperature to allow for the formation of nanoparticles. Then washing and drying are needed. The nanoparticles are washed with a suitable solvent to remove any impurities and dried at a low temperature. Finally the synthesis ends by calcination process. The dried nanoparticles are calcined at a high temperature to remove any residual impurities and to induce the desired phase transformation.

The co-precipitation method can produce nanoparticles with various sizes, shapes, and compositions. The size and morphology of the nanoparticles can be controlled by adjusting the reaction parameters such as temperature, pH, and stirring rate. The composition of the nanoparticles can be controlled by adjusting the ratio of the metal salts in the precursor solution. Was reported the nanoparticles of neodymium orthophosphate (NdPO_4) were synthesized using a straightforward wet coprecipitation method. The nanoparticles of neodymium orthophosphate (NdPO_4) obtained in this study were found to belong to the monoclinic phase of the monazite structure, with lattice parameters of $a = 0.673(4)$ nm, $b = 0.695(7)$ nm, $c =$

0.641(6) nm, and $\beta = 103^{\circ}68'$. The crystallite size was determined to be 30.8 nm. Particle size analysis confirmed that the synthesized material was in the nanoscale range. Electron microscopic studies revealed that the particles were spherical in shape with a grain size of 92 nm. Elemental analysis using energy dispersive X-ray analysis (EDAX) confirmed the presence of major elements in the synthesized composition. Thermal analysis showed two decomposition stages of NdPO_4 , corresponding to endothermic peaks, indicating the removal of water molecules and the transformation from an amorphous to crystalline phase. The structural transition from a hexagonal to monoclinic phase occurred above 800 °C [70]. The co-precipitation method has several advantages over other nanoparticle synthesis methods. First, it is a simple and low-cost method that can be easily scaled up for large-scale production. Second, it can produce nanoparticles with high purity, which is important for many applications. Third, it allows for precise control over the composition, size, and morphology of the nanoparticles. Fourth, it can produce nanoparticles with a narrow size distribution, which is important for many applications that require uniform particle size. Disadvantages of this method include its inapplicability to uncharged species, potential precipitation of trace impurities with the product, time-consuming nature, challenges in achieving batch-to-batch reproducibility, and limitations when reactants exhibit significant differences in precipitation rates [62].

1.2.4. Microwave-assisted hydrothermal synthesis methods

Microwave radiation is not located in the most energetic region of the electromagnetic spectrum, but rather falls between radio frequencies and infrared (IR) radiation, with frequencies ranging from approximately 300 MHz (0.3 GHz) to 300 GHz. Most commercial devices operate at a standard frequency of 2.45 GHz [71]. The corresponding wavelengths of microwave radiation, ranging from 1 meter to 1 centimeter, indicate that microwaves do not interact with matter at the atomic or molecular levels [72]. The existence of electromagnetic waves was predicted by Maxwell's equations formulated in 1873, but experimental verification was not achieved until much later, in the 1880s, by Heinrich Hertz, who was able to produce and detect microwave radiation (around 1 GHz) using a rudimentary generator [71]. The use of microwave-assisted methods for material synthesis started in the 1950s, but widespread acceptance has been gained mainly in the last two decades. In this method, microwave radiations directly transfer energy to materials by heating the movable electric charges using electromagnetic

radiation (EMR) [68,73,74]. This conversion of electromagnetic energy to thermal energy results in temperature increases ranging from 100 to 200 °C, using frequencies between 1 and 2.5 GHz [75,76]. One of the advantages of this method is the shorter reaction time, allowing for the completion of time-consuming reactions within a few minutes. Additionally, this method is capable of producing nanoparticles with narrow size distributions and small particle sizes [68]. The microwave hydrothermal method is a relatively new approach developed in recent years for powder preparation. It utilizes microwaves for heating, following the principles of the hydrothermal method, but it differs from traditional hydrothermal synthesis. The microwave hydrothermal method combines the advantages of microwaves and water heat, acting as a hybrid of the hydrothermal and microwave methods. Unlike the conventional hydrothermal method, which relies on conduction for heating, the microwave hydrothermal heating method utilizes microwaves to heat the sample. This allows for uniform heating throughout the sample, even at greater depths, without the limitations of heat conduction and temperature differences. As a result, the reaction speed is significantly improved. [77].

The microwave-assisted hydrothermal synthesis process can be described in several steps. Preparation of precursor solutions is the first step. The metal salts are dissolved in a suitable solvent to form a precursor solution. The solvent used can be water or an organic solvent, depending on the solubility of the metal salts. Mixing the precursor solutions is the second step. The precursor solutions are mixed together under controlled conditions such as temperature and stirring rate. Then the microwave irradiation is applied. The mixture is then placed in a microwave reactor and irradiated under controlled conditions. Microwave radiation causes the solvent to heat up rapidly, which enhances the reactivity of the precursors. After that the hydrothermal treatment is needed. After the irradiation step, the mixture is subjected to hydrothermal treatment under controlled conditions of temperature and pressure. Hydrothermal processing promotes the formation of nanoparticles and also helps to control the size, shape, and crystallinity of the nanoparticles. Washing and drying finish the process of the synthesis. The nanoparticles are washed with a suitable solvent to remove any impurities and dried at a low temperature. In some cases, calcination is performed at a high temperature to remove any residual impurities and to induce the desired phase transformation [78].

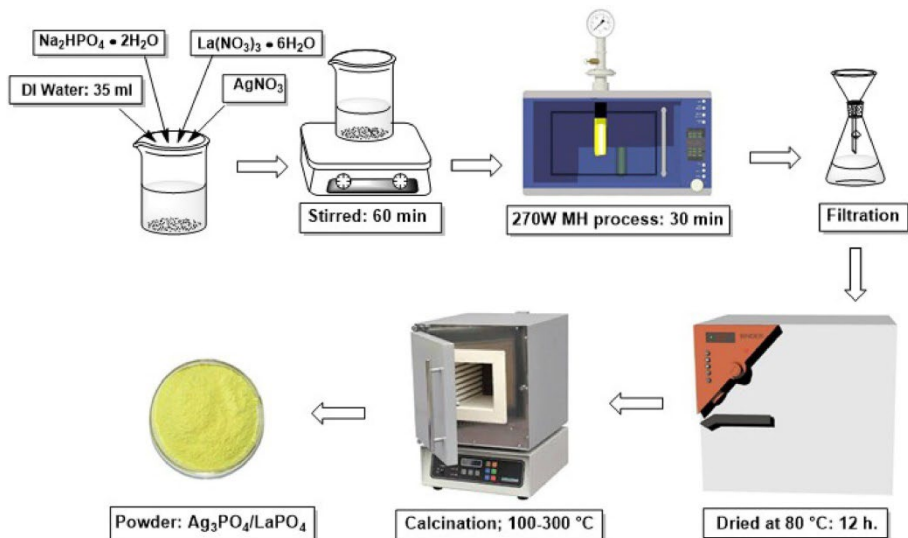


Fig. 5. Schematic diagram of microwave-hydrothermal synthesis for preparation of $\text{Ag}_3\text{PO}_4/\text{LaPO}_4$ composites [79].

However, it is reported that the hexagonal structured $(\text{Gd}, \text{Eu})\text{PO}_4$ urchin-like hollow spheres and cubic Ag_3PO_4 , monoclinic LaPO_4 samples were successfully synthesized by a simple microwave method in the absence of any templates or surfactants in the reaction system, and the effects of subsequent calcination on the structure [79,80]. Calcination can be used to change the crystal structure, for examples-synthesized $\text{La}_{1-x}\text{Tb}_x\text{PO}_4 \cdot n\text{H}_2\text{O}$ nanorods as rhabdophane-type structure and of the calcined $\text{La}_{1-x}\text{Tb}_x\text{PO}_4$ as monazite-type structure. Both the samples of rhabdophane-type and monazite-type structures nanorods are well-shaped, contain no linear or planar defects, and have high morphological uniformity [81].

The study showed that Rhabdophane-type Eu^{3+} , Tb^{3+} -codoped $\text{LaPO}_4 \cdot n\text{H}_2\text{O}$ single-crystal nanorods with different compositions were produced by hydrothermal synthesis using microwaves. The thermal stability of the nanorods was not affected by the Eu^{3+} , Tb^{3+} codoping, as they formed substitutional solid solutions where Eu^{3+} and Tb^{3+} replaced La^{3+} in the crystal lattice. Additionally, monazite-type Eu^{3+} , Tb^{3+} codoped LaPO_4 single-crystal nanorods were obtained by calcining the rhabdophane-type counterparts at moderate temperature in air, and they were found to be thermally stable [22].

Compared to the traditional hydrothermal method, the microwave hydrothermal method offers several advantages. It exhibits a rapid heating speed, facilitates sensitive reactions, and ensures a uniformly heated system. This enables the rapid synthesis of nanoparticles with a narrow particle size distribution and uniform morphology. Consequently, the microwave

hydrothermal method is well-suited for reactions with high temperature differences and long reaction times. It can efficiently prepare samples that require extended reaction times or are sensitive to temperature differences. It can be used to synthesize a wide range of nanoparticles, including metal oxides, sulfides, and hydroxides. The primary drawback is that the method requires special equipment. And quick heating of the reaction mixture lead to a rapid buildup of solvent vapor pressure, which poses a higher risk of explosion and potential equipment damage [73,82,83].

1.2.5. Solvothermal and hydrothermal synthesis methods

Solvothermal synthesis is a method of synthesizing nanoparticles using a organic solvent under high pressure and high temperature. The method involves dissolving precursors in a solvent and heating the mixture under high pressure and temperature to induce the formation of nanoparticles. The solvent used can be an organic solvent, depending on the solubility of the precursors. Meanwhile hydrothermal synthesis is a method of synthesizing nanoparticles or bulk materials under high pressure and high temperature conditions in an aqueous solution.

The synthesis process is carried out by the few steps. The precursor solutions are prepared first. The metal salts are dissolved in a suitable solvent to form a precursor solution. The solvent used can be water or an organic solvent, depending on the solubility of the metal salts. The reaction mixture is prepared. The precursor solutions are mixed together under controlled conditions such as temperature and stirring rate. The pH value of the solution can be modified, depending on the synthesis conditions, by adding acid or alkali to the prepared solution. Excipients can also be used. With the assistant of PVP synthesized rod-like $\text{GdPO}_4:\text{Er}^{3+}/\text{Yb}^{3+}$ pure hexagonal phase through a hydrothermal process [12], or tartaric acid can be used as a coordinating/capping agent for synthesizing $\text{GdPO}_4 \cdot n\text{H}_2\text{O}$ nanoparticles [84]. Heating under high pressure is the third step. The mixture is then transferred to a hydrothermal reactor, which is typically made of stainless steel and is capable of withstanding high pressure and temperature. The reactor can also have a Teflon liner which is inert to chemical effects. The reaction vessel is sealed and when heated under high pressure, usually above the boiling point of the solvent. The high pressure and temperature create a supercritical state of the solvent, which enhances the reactivity of the precursors. The mixture is subjected to solvothermal/hydrothermal treatment under controlled conditions of temperature and pressure.

Solvothermal/hydrothermal processing promotes the formation of nanoparticles and also helps to control the size, shape, and crystallinity of the nanoparticles. The synthesis process is finished by washing and drying. After the solvothermal/hydrothermal treatment, the reactor is cooled to room temperature and the nanoparticles are washed with a suitable solvent to remove any impurities and dried at a low temperature. The dried nanoparticles can be calcined at a high temperature to remove residual impurities and induce the desired phase transformation.

It was reported that the synthesis of lanthanide phosphates LnPO_4 crystals was achieved using a simple hydrothermal process [85]. The crystal structure of the synthesized LnPO_4 depends on the ionic radius of the lanthanide ions, with hexagonal or tetragonal structures observed. Hexagonal LnPO_4 (La, Ce, Pr, Nd, Sm, Eu, Gd, Tb, and Dy) samples show a wire-like morphology, while tetragonal LnPO_4 (Ho, Er, Tm, Yb, Lu, Y) samples consist of irregularly shaped particles. The hexagonal structured (La-Tb) PO_4 nanowires/nanorods undergo a transition to monoclinic monazite upon calcination, while retaining their morphology. Similarly, hexagonal DyPO_4 nanowires transform to tetragonal DyPO_4 nanowires after calcination. The as-synthesized LnPO_4 products consist mainly of nanowires/nanorods with diameters of 5-120 nm and lengths ranging from several hundreds of nanometers to several micrometers [37].

This is a useful method for synthesizing nanoparticles that can be used in biological and in biomedicine applications. By carefully selecting solvents and adjusting various factors such as temperature, pressure, pH, aging time, concentration of reactants, and reaction time, it is possible to create nanoparticles with specific sizes, shapes, and surface characteristics [84]. The successful synthesis was performed of monoclinic LaPO_4 and hexagonal $\text{LaPO}_4 \cdot 1.5\text{H}_2\text{O}$ nanocrystals with Eu^{3+} doping using a hydrothermal method demonstrates that the structure and shape of these nanocrystals are highly dependent on the pH and temperature of the growth solution. In other words, these factors play a critical role in determining the final structure and morphology of the LaPO_4 nanocrystals [36]. This method is particularly effective at creating very uniform nanoparticles without the need for post-annealing treatments, even at relatively low temperatures. Many different types of materials have been prepared using this method, including single crystals, nano particles, zeolites, oxides, doped metals, selenides, and sulphides. As a result, this method has become popular among researchers as an alternative to traditional methods.

The Solvothermal/hydrothermal method can produce nanoparticles with various sizes, shapes, and compositions. The size and morphology of the

nanoparticles can be controlled by changing and choosing the aforementioned synthesis conditions. The composition of the nanoparticles can be controlled by adjusting the ratio of the metal salts in the precursor solution. By adjusting the pH and molar ratio of gadolinium and phosphate, the size and shape of GdPO₄ nanoparticles can be manipulated. When the pH of the reaction medium was increased from 4 to 11, the width of GdPO₄ nanoparticles decreased from 93 to 23 nm, and the length decreased from 635 to 99 nm. Similarly, when the molar ratio of Gd to P was changed from 1:7.5 to 1:50, the width increased from 19 to 60 nm, and the length decreased from 154 to 128 nm. Interestingly, the size and distribution of Eu³⁺-doped nanoparticles remained relatively unchanged, regardless of the concentration of Eu³⁺ [86].

The successful preparation of various GdPO₄:5%Eu³⁺ micro/nanomaterials with different crystal structures and morphologies using a one-step solvothermal method. The materials were synthesized using only gadolinium and phosphoric acid sources and ethanol as solvents without any surfactants or templates. The ratio of phosphoric acid to gadolinium sources was adjusted to regulate the morphology of the products, resulting in the formation of seven different shapes. Monoclinic crystal structures: square, pillow, star, carambola shape and hexagonal crystal structures: hollow cylinder, drum, jujube shape [87].

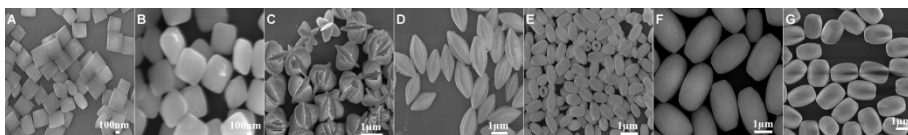


Fig. 6. SEM images of the GdPO₄:5%Eu³⁺ samples synthesized with different volume-mass ratios of H₃PO₄ to RE(NO₃)₃·6H₂O: (A) 2, (B) 8, (C) 16, (D) 24, (E) 32, (F) 40 and (G) 48 mL/g [87].

In summary, solvothermal/hydrothermal synthesis are methods used to create nanoparticles by dissolving precursors in a solvent and subjecting them to high pressure and temperature. This method has several advantages over other nanoparticle synthesis methods. First, it can produce nanoparticles with high purity and crystallinity, which is important for many applications. Second, it allows for precise control over the size, morphology, and composition of the nanoparticles. Third, it can produce nanoparticles with a narrow size distribution, which is important for many applications that require uniform particle size. Fourth, it can be used to synthesize a wide range of nanoparticles. The solvothermal/hydrothermal process promotes the

formation of nanoparticles and allows for the production of uniform particles without the need for post-annealing treatments. For my work, I chose the solvothermal/hydrothermal method to synthesize doped GdPO₄ nanoparticles. This method provides high purity and crystallinity, precise control over particle characteristics, and the ability to create nanoparticles with a narrow size distribution. Although the conditions for the synthesis of doped GdPO₄ synthesized in this work are still not perfected and fully investigated. Currently, there are a number of publications with works aimed at improving the synthesis method of GdPO₄ nanoparticles. It is a versatile approach that has been successfully applied to various materials, including single crystals, oxides, zeolites, and doped metals. The solvothermal/hydrothermal method is particularly useful in biological and biomedical applications due to its ability to create nanoparticles with specific sizes, shapes, and surface characteristics. These benefits make it a popular choice among researchers as an alternative to traditional synthesis methods. The hydrothermal synthesis method is an effective and versatile method for the preparation of nanoparticles with controlled size, composition, and morphology.

1.3. Basic of luminescence

Luminescence is a phenomenon in which a material emits light after being stimulated by an external energy source. The energy source can be a variety of different types, including heat, light, or electricity. When the material absorbs energy, its electrons become excited and move to higher energy levels. When the electrons return to their original energy level, they emit the excess energy as light [88].

Fluorescence is a type of luminescence that occurs when a material absorbs energy from a light source and then emits that energy as light almost immediately. This type of luminescence is widely used in various applications, including in fluorescent lighting, medical imaging, and materials science. For example, fluorescent dyes are often used in biological imaging applications to visualize specific molecules or structures within cells [89].

Phosphorescence is similar to fluorescence, but the emission of light occurs over a longer period of time. In this case, the excited electrons remain in their higher energy state for a longer period before emitting the excess energy as light. This type of luminescence is often observed in materials

such as glow-in-the-dark materials, which continue to emit light after the external energy source is removed [90].

Chemiluminescence is another type of luminescence that occurs as a result of a chemical reaction. This type of luminescence is commonly used in analytical chemistry, particularly in the detection of trace amounts of substances. For example, luminol is a chemical compound that emits light when it reacts with certain substances, such as blood. This property is used in forensic science to detect blood at crime scenes [91].

Luminescence is a fascinating phenomenon that is widely used in a variety of scientific and technological applications. Its ability to convert energy from one form to another and emit light has led to many innovative developments, and it continues to be an important area of research in materials science, chemistry, and physics [92].

1.3.1. Luminescence properties of lanthanide orthophosphate

Rare earth phosphates, also known as LnPO_4 , are characterized by low solubility, high thermal stability, high refractive index, and a high concentration of luminescent centers in Eu^{3+} etc. ions. These properties make LnPO_4 materials attractive for research and have led to extensive investigation [37]. Europium ions (Eu^{3+}) doped in phosphors exhibit excellent red luminescence in various host lattices. They serve as active luminescence centers due to their abundant transitions, the narrow orange emission at around 594 nm ($^5\text{D}_0 \rightarrow ^7\text{F}_1$) and red emission at about 690 nm ($^5\text{D}_0 \rightarrow ^7\text{F}_4$) falling into the human tissue transparency windows [6,13]. Under UV excitation, Eu^{3+} ions are well-known for acting as red-emitting activators through their $^5\text{D}_0 \rightarrow ^7\text{F}_J$ ($J = 0, 1, 2, 3, 4$) transitions [93–95]. Additionally, higher excited states such as $^5\text{D}_1$ (green), $^5\text{D}_2$ (green, blue), and $^5\text{D}_3$ (blue) can also produce emissions when Eu^{3+} ions are situated in a suitable host material with low photon energy. This suggests the potential for generating white light emission by doping the appropriate amount of Eu^{3+} into a specific material. However, there is a scarcity of studies that specifically focus on achieving white light emission using phosphors doped solely with Eu^{3+} ions [96–99]. The luminescent properties of lanthanide orthophosphates are a result of the unique electronic structure of the lanthanide ions. Lanthanide ions have partially filled 4f orbitals, which are shielded from the surrounding environment by the filled 5s and 5p orbitals. The 4f orbitals are thus relatively unperturbed by the chemical environment, and the transitions between the 4f energy levels give rise to the characteristic

sharp and narrow emission bands in the visible and near-infrared regions of the electromagnetic spectrum [100]. Trivalent lanthanide ions, which have a gradual filling of the 4f orbitals from $4f^0$ (for La^{3+}) to $4f^{14}$ (for Lu^{3+}) have interesting photoluminescence properties and emit light in different colors depending on the type of ion. For example, Eu^{3+} emits red light [93], Tb^{3+} emits green light [101], Sm^{3+} emits orange light [102], and Tm^{3+} emits blue light [103]. Some lanthanide ions also show near-infrared luminescence, such as Yb^{3+} [104], Nd^{3+} [105], and Er^{3+} [106]. Gd^{3+} emits in the ultraviolet region [107]. When discussing the light emission by lanthanide ions, the term "luminescence" is often used instead of "fluorescence" or "phosphorescence." This is because fluorescence and phosphorescence are used to describe light emission by organic molecules and incorporate information about the emission mechanism. In the case of lanthanides, the emission is due to transitions within the 4f shell, which are intraconfigurational f-f transitions. The partially filled 4f shell of lanthanide ions is well-shielded from its environment by the closed $5s^2$ and $5p^6$ shells. This means that the ligands in the first and second coordination sphere have only a limited effect on the electronic configurations of trivalent lanthanide ions. This shielding is responsible for the specific properties of lanthanide luminescence, particularly for the narrow-band emission and long lifetimes of the excited states [108]. However, Ce^{3+} is a special case because it emits intense broadband emission due to allowed f-d transitions. The position of the emission maximum strongly depends on the ligand environment of the Ce^{3+} ion. Different types of luminescence are defined depending on the method of excitation, including photoluminescence (emission after excitation by irradiation with electromagnetic radiation), electroluminescence (emission by recombination of electrons and holes under the influence of an electric field), chemiluminescence (nonthermal production of light by a chemical reaction), or triboluminescence (emission observed by applying mechanical stress to crystals or by fracture of crystals) [108,109].

The luminescence of lanthanide orthophosphates can be enhanced by a variety of factors, including the crystal structure, particle size, morphology, and surface chemistry of the nanoparticles [21,110,111]. The monazite-type nanorods with the same Eu^{3+} , Tb^{3+} -codoping content have a greater efficiency in photoluminescence compared to the rhabdophane-type nanorods. The $\text{La}_{0.97999}\text{Eu}_{0.02}\text{Tb}_{0.00001}\text{PO}_4$ nanorods exhibit the highest photoluminescence emission. It was observed that in $\text{La}_{0.99999-x}\text{Eu}_x\text{Tb}_{0.00001}\text{PO}_4$, energy transfer from Tb^{3+} to Eu^{3+} does not occur, and a minimum content of 1 mol% Tb^{3+} is required for an efficient energy transfer

in the codoped systems [22]. For example, the luminescence of lanthanide orthophosphates can be increased by reducing the particle size, which can lead to increased surface area and improved energy transfer between the lanthanide ions [94]. Similarly, doping the lanthanide orthophosphate with other elements can also enhance the luminescence properties by introducing additional energy transfer pathways.

Lanthanide orthophosphates can exhibit several different types of luminescence, including fluorescence, phosphorescence, and upconversion luminescence. Fluorescence is the emission of light when an excited electron relaxes back to its ground state, while phosphorescence is a type of delayed fluorescence in which the excited electron relaxes back to its ground state over a longer period of time. Upconversion luminescence is a process in which multiple low-energy photons are absorbed and converted into a single high-energy photon [112]. This phenomenon occurs in lanthanide-doped materials and is useful in applications such as solar cells and bioimaging [113,114].

The long luminescence lifetime of lanthanide orthophosphates, typically ranging from microseconds to milliseconds, is another important property that makes them useful in various applications. The long lifetime allows for time-resolved imaging and reduces background fluorescence, leading to improved imaging contrast. Additionally, the luminescence of lanthanide orthophosphates is often resistant to photobleaching, making them attractive alternatives to organic dyes in biological imaging applications [115].

In summary, the luminescent properties of lanthanide orthophosphates are a result of the unique electronic structure of the lanthanide ions and can be enhanced by controlling the crystal structure, particle size, morphology, and surface chemistry of the nanoparticles. These materials have a range of applications in fields such as lighting, optical devices, and biomedical imaging.

1.3.2. Luminescent application of lanthanide orthophosphate

Lanthanide orthophosphate nanoparticles can exhibit enhanced luminescence and tunable emission wavelengths, making them useful for a variety of optical applications such as sensors, lighting, and display technologies [37,116]. Lanthanide orthophosphate nanoparticles have potential for use in biomedical applications such as drug delivery, imaging, and cancer therapy due to their biocompatibility, low toxicity, and ability to target specific cells or tissues [67,117,118]. Lanthanide-doped phosphors are

widely used in solid-state lighting applications due to their high efficiency, color tunability, and long lifetime. For example, cerium-doped yttrium aluminum garnet (YAG:Ce) is used in white LEDs [119], while terbium-doped aluminum oxide ($\text{Tb}^{3+}:\text{Al}_2\text{O}_3$) is used in green LEDs [120]. Lanthanide-doped phosphors are also used in fluorescent lamps to improve their color rendering index and reduce energy consumption [121], recently, scientists are working to produce micro LEDs. Therefore, it is difficult to overestimate the influence of lanthanoid luminescence on the development of lighting [100,122]. Lanthanide orthophosphates have a wide range of applications in various fields, including lighting, optical devices, catalysis, and biomedical imaging. Lanthanide orthophosphates also have potential applications in optical devices, such as waveguides, optical amplifiers, and lasers. For example, YbPO_4 nano-cylinders can be used as gain media in fiber amplifiers and lasers [123]. There are methods developed that involve synthesizing nanoparticles of $\text{Al}_2\text{O}_3:\text{Er}^{3+}$ or $\text{AlPO}_4:\text{Yb}^{3+}/\text{Er}^{3+}$. These nanoparticles are then integrated into silica preforms and subsequently drawn into fibers [124,125]. Comparing fibers with identical Opto-geometrical parameters, it has been demonstrated that the nanoparticle-based fibers consistently outperform standard fibers in terms of amplification factor [126], laser efficiency [127], and resistance to ionizing radiation [128]. Lanthanide-doped waveguides are also being investigated for their potential applications in optical communication and sensing [129,130].

It is important to note that alloyed lanthanide orthophosphates significantly broaden the range of applications. Scientists have the opportunity to combine different lanthanide elements, thereby extracting unique properties of the synthesized materials and applying them in various relevant fields. For instance, doping GdPO_4 with Er^{3+} , Yb^{3+} , and Eu^{3+} enables the development of materials with dual excitation and dual emission nano phosphors. These phosphors exhibit broad UV and IR excitation, making them suitable for potential utilization in solar spectrum conversion and bioimaging applications [131]. The studies demonstrate that it is possible to generate white light using a single matrix containing three distinct luminescent centers. Tunable white light photoluminescence can be achieved from a single-phase phosphor of GdPO_4 codoped with Tm^{3+} , Tb^{3+} , and Eu^{3+} [132]. Lanthanides possess unique properties due to their 4f electrons. The 4f orbitals can contain up to seven unpaired electrons that have strong angular momentum, leading to effective spin-orbit coupling and significant paramagnetic properties, with the exception of La^{3+} and Lu^{3+} . The magnetic moments, magnetic susceptibilities, and electronic relaxation time of Ln^{3+} are determined by their 4f electron configurations, which vary

significantly along the series [133,134]. The symmetric electron ground state of Gd^{3+} results in weak spin-orbit coupling, leading to a long electronic relaxation time. In contrast, the asymmetric electron ground states of Tb^{3+} , Dy^{3+} , Ho^{3+} , and Er^{3+} result in a short electronic relaxation time but larger magnetic moments and magnetic susceptibilities. Furthermore, lanthanides are appealing for optical applications due to their large quantum numbers ($n = 4, l = 3$), which provide them with rich spectroscopic terms [135]. While intraconfigurational transitions are typically forbidden for Ln^{3+} , the inclusion of eigenstates permits partially allowed intraconfigurational transitions, granting favorable optical properties to Ln^{3+} activated materials. These properties include exceptional photostability, significant Stokes/anti-Stokes shifts, extended luminescent lifetimes, and precise-band emissions [100,108].

Nanorods of gadolinium orthophosphate co-doped with light-emitting lanthanide ions were synthesized through a hydrothermal method. These nanorods exhibited efficient downconversion luminescence from Ce/Tb or Eu^{3+} doping, and upconversion luminescence from Yb/Er co-doping. This provides an optical modality for the nanoprobe. $GdPO_4:1\%Er^{3+}, 10\%Yb^{3+}, 5\%Eu^{3+}$ nanorods show strong orange-red emission under both UV and NIR light, and are used to fabricate luminescent security ink for anti-counterfeiting applications. These security patterns are white in color under day light, but exhibit orange-red color under UV and/or NIR light, and are stable under light, humidity, and temperature without degradation of color intensity. The $GdPO_4:1\%Er^{3+}, 10\%Yb^{3+}, 5\%Eu^{3+}$ nanorods are considered to have potential for anti-counterfeiting with high security features [50].

1.3.3. Environmental application of lanthanide orthophosphate

The safe disposal of nuclear waste is a significant concern for the nuclear industry and the general public. Geological repositories are considered the most viable option for the long-term disposal of nuclear waste, as they provide a natural barrier to isolate the waste from the biosphere. The multiple barrier approach involves storing the nuclear waste in canisters made of materials that can withstand corrosion and degradation over long periods of time, which are then placed in a geological repository that provides a barrier against the release of radioactive material. $REPO_4$ are considered promising materials for nuclear waste immobilization [136].

However, even with the multiple barrier approach, the possibility of a failed canister situation still exists. In such a scenario, groundwater present

near the repository may penetrate the waste containment system and eventually come in contact with the nuclear waste material. This could lead to the release of radioactive elements and contamination of the surrounding environment. Therefore, it is crucial to assess the durability of the materials used in the waste containment system to ensure that they can effectively contain the nuclear waste. Rare-earth phosphate materials, such as monazite, xenotime, and rhabdophane, have been proposed as potential host matrices for the immobilization of actinides. Actinides are highly radioactive elements, such as uranium and plutonium, that are present in nuclear waste. Monazite and xenotime are abundant rare-earth minerals that contain varying amounts of actinides incorporated within their crystal structure. These minerals are proposed as a potential host matrix for the immobilization of actinides because of their low solubility, high thermal stability, and chemical durability. Rhabdophane, on the other hand, is a hydrous rare-earth mineral that forms on the surface of chemically altered monazite mineral and is proposed to act as a protective barrier by preventing the release of actinides to the biosphere. To assess the chemical durability of rare-earth phosphate materials, this study conducted leaching experiments on monazite-type, xenotime-type, and rhabdophane-type materials. The materials were exposed to deionized water for a period of seven months, and the concentration of the leached elements in the water solution was determined using inductively coupled plasma mass spectrometry (ICP-MS). The results showed that the leaching rates of the rare-earth phosphate materials were low, indicating their chemical durability. Analysis showed that the long-range and local structures of monazite-, xenotime-, and rhabdophane-type materials remain unaffected after exposure to water for seven months. In conclusion, the study suggests that rare-earth phosphates, specifically LaPO_4 , YbPO_4 , and $\text{GdPO}_4 \cdot \text{H}_2\text{O}$, are suitable for use in nuclear waste storage systems. These materials show excellent chemical durability and can effectively contain actinides, which are present in nuclear waste. The results of this study contribute to the ongoing efforts to develop safe and effective methods for the disposal of nuclear waste [137,138].

Lanthanide orthophosphates can be used as heterogeneous catalysts in various chemical reactions, such as the conversion of alcohols to aldehydes, dehydration of alcohols, and selective oxidation of alcohols. The unique chemical properties of lanthanide ions, such as their Lewis acid-base character and redox properties make them effective catalysts in these reactions. Rod-shaped nanocrystalline lanthanum phosphate with an average length of 40 nm, synthesized using a room-temperature aqueous sol-gel process, ammonia temperature-programmed desorption measurements

indicate that the density of Lewis acid sites in this material is four times higher than in any previously reported lanthanum phosphate. The sample has demonstrated catalytic activity as a Lewis-acid catalyst in an acetal-formation reaction, achieving a yield of 85% [139]. As well as photocatalyst energy gaps of Ag_3PO_4 and LaPO_4 containing in the $\text{Ag}_3\text{PO}_4/\text{LaPO}_4$ composites without high temperature calcination were 2.37 eV and 4.23 eV, respectively. Their photocatalytic efficiency in degrading treatment of methyl orange was the highest of 94.0% within 20 min and 95.7% within 60 min controlled by Schottky interface, energy gap, specific surface area, pH of solution, dye concentration and catalytic content [79].

1.3.4. Magnetic applications of lanthanide orthophosphate.

Lanthanides are also of interest because of their magnetic properties and their potential applications the magnetic properties of lanthanide ions have certain advantages that differ from those of other types of magnetic carriers, such as transition metal ions and organic radicals. Lanthanide ions have both large spin and orbital moments due to the internal nature of their valence f orbitals. However, unlike transition metal ions, all paramagnetic lanthanide ions except for Gd(III) and Eu(II) with f^7 electron configuration have orbitally degenerate ground states that are split by spin-orbit coupling and ligand field effects. Because of this, the magnetic properties of lanthanide-containing materials are heavily influenced by the large spin-orbit coupling and orbital magnetic moment contribution. However, studying the magnetic properties of lanthanides is difficult because their unpaired f electrons are highly contracted and energetically shielded by outer 5d and 6s shells. As a result, the direct magnetic interaction between $4f^7$ - $4f^7$ electrons is weak, and the coupling constant J is normally smaller than 1 cm^{-1} . Unlike in rare-earth intermetallic compounds, where the magnetic interaction is mediated by the spin polarized 4f localized electrons and conduction electrons, in lanthanides, the magnetic interaction is mediated by the spin polarized 5d and 6s valence electrons. The $4f^7$ exchange field can be treated as a kind of contact effect that only exerts its influence on the orbitals centered on the Gd atom. This local character of the $4f^7$ exchange field can be treated by a simple perturbative molecular orbital model and accounts for the perturbation of the $4f^7$ cores exerting on electrons that reside in molecular orbitals with 5d and 6s characters [133].

Lanthanide orthophosphates are being investigated for their potential applications as contrast agents in biomedical imaging techniques, such as

magnetic resonance imaging (MRI) and fluorescence imaging [5,140]. The long luminescence lifetime and narrow emission bands of lanthanide-doped nanoparticles make them attractive candidates for imaging applications, especially in biological systems. Syntheses were performed of $\text{GdPO}_4:5\%\text{Eu}^{3+}$ micro/nanoparticles using solvothermal synthesis. The study aimed to explore the effects of crystal structure and morphology on the luminescence and MRI tracing properties of gadolinium phosphate in the same synthetic system. The researchers found that by adjusting the ratio of H_3PO_4 to $\text{Gd}(\text{NO}_3)_3 \cdot 6\text{H}_2\text{O}$, they could control the shape of the micro/nanoparticles formed, resulting in square-, pillow-, star-, carambola-, hollow cylinder-, drum- and jujube-shaped particles. Of all the shapes synthesized, the carambola-shaped $\text{GdPO}_4:5\%\text{Eu}^{3+}$ particles showed the best luminescence and MRI tracer performance. The carambola-shaped particles had a strong emission peak at 596 nm, showed orange-red emission in the CIE chromaticity diagram, and had a lifetime of 3.713 ms (τ_{ave}) and color coordinates of (0.6138, 0.3856). The MRI monitoring of the carambola-shaped particles had a relaxation rate (r_1) of $0.7709 \text{ mM}^{-1} \text{ s}^{-1}$, which was similar to the 61.5% higher r_1 value compared to the lower preparation of square $\text{GdPO}_4:5\%\text{Eu}^{3+}$. The study also explored the mechanism of morphology formation and analyzed the factors influencing the fluorescence and MRI tracer performance. The researchers suggested that the factors influencing the properties of the micro/nanoparticles could be a combination of morphology, size, crystal structure, crystal growth orientation, crystallinity, and specific surface area, with only the main influencing factors differing. The research has potential applications in the field of MRI tracing of implantable materials [87,141].

Hollow $\text{GdPO}_4:\text{Eu}^+$ microspheres are claimed to be suitable for drug delivery. $\text{GdPO}_4:\text{Eu}^+$ hollow microspheres, which are approximately 1 to 1.5 μm in diameter, emit light in response to excitation at 245 nm, displaying emission bands from the $^5\text{D}_0 / ^7\text{F}_j$ ($J = 1, 2, 3$ and 4) transitions of Eu^{3+} . These microspheres were tested for drug release properties using doxorubicin hydrochloride (DOX) release test, and for biocompatibility using the standard 3-(4,5-dimethylthiazol-2-yl)-2,5-diphenyltetrazolium bromide (MTT) assay. The results of both tests suggest that hexagonal $\text{GdPO}_4:\text{Eu}^{3+}$ hollow microspheres have a sustained drug release property, indicating their strong potential for use in the biomedical field [142]. Later studies explored the drug loading and release properties of GdPO_4 nanoparticles with and without Eu^{3+} doping, using a simple electrochemical protocol in an in-vitro environment. The electrochemical method for drug loading and releasing was validated and compared with UV-vis

spectroscopy. The nanoparticles were found to have good luminescent and magnetic properties, with spherical mesoporous structures. The high loading capacity and encapsulation efficiency were observed when the anti-fever drug, acetaminophen, was loaded onto the nanoparticles. A smooth and spontaneous release was observed at a moderate high temperature and low pH, without any sign of burst release. These nanoparticles may be suitable for targeting and specific drug release in response to pH and temperature, making them a potential drug carrier for in-vivo applications[143].

The unique properties of lanthanide orthophosphates make them promising materials for a wide range of applications in various fields. Further research and development in this area are likely to uncover new and exciting applications for these materials in the future.

2. EXPERIMENTAL PART

2.1. Chemicals and Reagents

2.1.1. Materials used for the synthesis

The following materials were used for the synthesis of phosphates $\text{Gd}(\text{NO}_3)_3 \cdot 6\text{H}_2\text{O}$ (99.9%, Glentham), $\text{Eu}(\text{NO}_3)_3 \cdot 6\text{H}_2\text{O}$ (99.9%, Alfa Aesar), $\text{La}(\text{NO}_3)_3 \cdot 6\text{H}_2\text{O}$ (99.9%, Alfa Aesar), tartaric acid $\text{C}_4\text{H}_6\text{O}_6$ (99.5%, Eurochemicals), ammonium dihydrogen phosphate $\text{NH}_4\text{H}_2\text{PO}_4$ (99 %, Eurochemicals), diammonium hydrogen phosphate $(\text{NH}_4)_2\text{HPO}_4$ (99 %, Eurochemicals) citric acid $\text{C}_6\text{H}_8\text{O}_7$ (99,5% Eurochemicals).and concentrated HNO_3 (65.0%, Sigma-Aldrich).

2.1.2. Control material of the cytotoxicity study

The negative control was high-density polyethylene film (NC). Positive control was 0.1% zinc containing polyurethane film (RM-A) and 0.25% zinc dibutyldithiocarbamate containing polyurethane film (RM-B). Three types of films for control were purchased at the Food and Drug Safety Center (Hatano Research Institute, Ochiai 729-5, Hadanoshi, Kanagawa 257, Japan).

The mouse fibroblast-like cell line L929 (RCB2619) was obtained from RIKEN Cell Bank. The culture medium was MEM (Minimum Essential Medium Eagle, SIGMA-ALDRICH) medium with 10% FBS (Fetal Bovine Serum Qualified One Shot, gibco) and 1% Penicillin-Streptomycin Solution (Wako).

2.2. Synthesis and Processing

2.2.1. Synthesis and Processing of $\text{GdPO}_4:15\%\text{Eu}$ samples

15% of Gd was replaced by Eu, resulting $\text{Gd}_{0.85}\text{Eu}_{0.15}\text{PO}_4 \cdot \text{H}_2\text{O}$ formula of the desired compound. In each synthesis, the number of precursors was calculated in order to obtain 0.1 g of product, meaning $\text{Gd}(\text{NO}_3)_3 \cdot 6\text{H}_2\text{O}$ – 0.1526 g, $\text{Eu}(\text{NO}_3)_3 \cdot 6\text{H}_2\text{O}$ – 0.0266 g, $\text{C}_4\text{H}_6\text{O}_6$ – 0.4575 g, $\text{NH}_4\text{H}_2\text{PO}_4$ – 0.1785 g were weighed accordingly. The tartaric acid was added 3 : 1 ratio to all cations on purpose to get Gd-tartaric acid and Eu-tartaric acid complex, meanwhile cations and phosphate ratio 1 : 10 was kept. All materials were

dissolved separately in distilled water and left under stirring for 30 min. at 50 °C. The amount of distillate water was selected according to the desired total amount of solution (10 mL, 20 mL, 30 mL, 40 mL, 50 mL, 60 mL). $\text{Gd}(\text{NO}_3)_3 \cdot 6\text{H}_2\text{O}$, $\text{Eu}(\text{NO}_3)_3 \cdot 6\text{H}_2\text{O}$ and $\text{C}_4\text{H}_6\text{O}_6$ solutions were mixed and left under stirring for 30 min. at 50 °C in order for Gd-tartaric acid complex to form. Afterwards, $\text{NH}_4\text{H}_2\text{PO}_4$ solution was added drop by drop to the freshly prepared solution of cations and left under stirring for 30 minutes at 50 °C. Finally, the pH value was adjusted to 1 by adding HNO_3 solution.

The hydrothermal syntheses were performed in Berghof High-pressure reactor BR with 100 mL Teflon vessel, using BTC-3000 temperature controller, BMH Heating jacket and IKA RH Digital mixer. The reaction mixture was poured into a Teflon vessel autoclave, which was then sealed and placed into a hydrothermal reactor. The pressure in the reactor was increased to 4 bars with compressed air. The temperature was slowly increased to 180 °C and maintained throughout the syntheses for 18 h.

The obtained mixture was centrifuged at 7000 rpm and washed with distilled water. This procedure was repeated four times, and two times this procedure was repeated using $\text{C}_2\text{H}_5\text{OH}$ for washing. The precipitate was left to dry in the air at 70 °C.

2.2.2. Synthesis and Processing of $\text{Gd}_{1-x}\text{Eu}_x\text{PO}_4$ and $\text{Gd}_{1-x}\text{La}_x\text{PO}_4$:15%Eu samples

Firstly, required amounts of gadolinium, lanthanum, and europium nitrates are dissolved in 5 mL of distilled water for about 0.5 mmol of the final product (around 0.1 grams). Then a 10 mL solution of citric acid, containing double the moles of citric acid as compared to the metals, is added to the europium and gadolinium solution, and stirred for 10 minutes. Then a 5 mL water solution of ammonium dihydrogen phosphate or diammonium hydrogen phosphate is added slowly. Then the solution is diluted to the desired volume (25 mL). And the final mixture is stirred for 30 minutes. Then the solution is transferred to the Teflon lined autoclave and left inside a furnace at 180 °C temperature for 18 hours. The obtained powders are centrifuged (7000 rpm 10 minutes) and washed with deionized water and ethanol 3 times. Then dried at 70 °C for 24 h and characterized.

2.2.3. Preparation of the extract and cytotoxicity test

Samples were sterilized with ethylene oxide gas (EOG). 1 mL of medium was added to 0.2 g of samples and extracted for 24 hours at 37 °C in a 5% CO₂ incubator. The extract was diluted with medium to obtain 75%, 50%, 25%, 12.5% and 6.25 % diluted extract medium.

The negative and positive control materials were sterilized by high-pressure steam at 121 °C for 15 minutes, respectively. 1 mL of the medium was added to 0.1 g of control material, and extraction was performed in the same way as the samples described above. Each extract of the positive control was diluted with medium to obtain 75%, 50%, 25%, 12.5%, and 6.25% diluted extract medium. The extract of the negative control was not diluted meaning used as it was.

2.2.4. Cytotoxicity test

Monolayer-grown L929 cells were detached by trypsinization, and a cell suspension of 1×10^5 cells/ mL was prepared using the medium. This cell suspension was seeded into each well of 96-well cell culture plates at 0.1 mL /well and incubated for 24 h at 37 °C in a 5% CO₂ incubator.

MTT solution (Nacalai Tesque) was added to 0.01 mL /well and incubated for 2 h at 37 °C in a 5% CO₂ incubator, allowing MTT to be reduced to formazan. Then, 0.1 mL /well of the solubilized solution (Nacalai Tesque) was added and the formazan was dissolved by incubation at 37 °C for 24 hours in a sealed plate seal. No remaining MTT crystals were confirmed by optical microscope and the absorbance at 570 nm was measured by a microplate reader (ChroMate, Awareness Technology, Inc(USA)). The reference wavelength was set at 650 nm.

2.3. Characterization Techniques

X-ray diffraction (XRD) analysis was performed using a Rigaku MiniFlex II. The source of the diffractometer radiation was Ni-filtered Cu K α 1. Measurements were performed in the 10–80° 2 θ range at room temperature. A glass sample holder was used on which the sample was placed.

The Hitachi SU-70 scanning electron microscope (SEM) was used for particles morphology and size analyses. The sample was diluted with ethanol, and one drop of the prepared mixture was applied to a carbon film. Then the SEM sample holder with the sample was dried by blowing with a

stream of dry air. The microscope was adjusted, and the appropriate magnification was selected. After that, the image was recorded. An open-access program, Fiji, was used for image analysis.

The Edinburgh Instruments FLS980 spectrometer was used to investigate the luminescent properties. The spectrometer is equipped with double excitation and emission monochromators, 450 W Xe arc lamp, a cooled (-20°C) single-photon counting photomultiplier (Hamamatsu R928) and lens optics for powder samples. For excitation and emission measurements, the step size was 0.5 nm, and the dwell time was 0.2 s. Excitation spectra were measured in the range from 250 to 585 nm. Emission spectra were measured in the range from 450 to 800 nm. The photoluminescence emission spectra were corrected by the correction file obtained from a tungsten incandescent lamp, certified by NPL (National Physics Laboratory, UK). Excitation wavelengths of 393.0 nm were selected, while the emission was monitored at 591 nm.

BET Surface area analyser TriStar II 3020, Micromeritics was used for surface area and porosity analysis. The surface areas were determined by the Brunauer, Emmet, and Teller (BET) method. The pore sizes were determined by Barrett, Joyner, and Halenda (BJH) method.

The cytotoxicity test was conducted three times, and the cell viability (%) was calculated by the following equation.

Viability (%) = $100 \times [\text{Absorbance of the extract}] / [\text{Absorbance of the blank}]$

The magnetization of samples was recorded using vibrating sample magnetometer consisting of the lock-in amplifier SR510 (Stanford Research Systems), the gauss/teslameter FH-54 (Magnet Physics) and the laboratory magnet supplied by the power source SM 330-AR-22 (Delta Elektronika).

3. RESULTS AND DISCUSSIONS

3.1. Investigation of the optimal europium concentration in $Gd_{1-x}Eu_xPO_4 \cdot H_2O$

In this work, the hydrothermal synthesis method was chosen because it ensures high purity and crystallinity, precise control of particle characteristics, and the possibility of creating nanoparticles with a narrow size distribution. The hydrothermal method is particularly useful in biomedicine because it can create nanoparticles of specific sizes, shapes, and surface properties. The principle scheme of the synthesis is presented in Fig. 7.

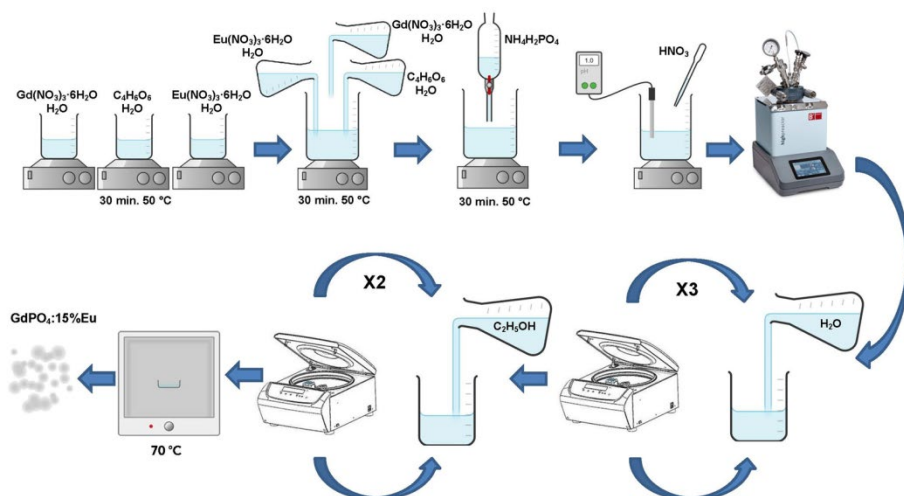


Fig. 7. Schematic diagram of hydrothermal synthesis

In order to determine the optimal amount of doped Eu^{3+} for the highest luminescence emission of nanoparticles of gadolinium phosphate, a series of syntheses varying the amount of Eu^{3+} from 1% to 20% was performed. To investigate the phase composition as well as the crystal structure of the synthesized compounds, X-ray diffraction (XRD) analysis was used. XRD patterns are represented in Figure 8. All the peaks present in the given diffraction patterns correspond well and are attributed to the hexagonal crystal structure of the $GdPO_4 \cdot H_2O$ (space group $P3_121$ (#152), PDF ICDD 00-039-0232). There is no indication of any secondary phases as no non ascribed reflections appear in the diffraction patterns even 20% of europium doping. This indicates that all europium has been successfully introduced

into the hexagonal gadolinium phosphate structure. It is worthy to note that even when 20% of gadolinium is replaced by europium there is no clear evidence of peak shift, this may be due to the similarity of gadolinium and europium ionic radii. According to the literature data, gadolinium and europium ionic radii are 1.06 Å and 1.07 Å respectively [38]. Note, the sample containing 5% of Eu^{3+} demonstrates offset resulting probably by the sample preparation. However, there is a clear difference observed between the different patterns presented in Figure 8. First of all, for the samples containing from 5 to 15 percent of europium the background in the range of 5-35° 2θ degree exhibit a quite high intensity. It indicates quite poor crystallinity resulting in the formation of the amorphous phase. An increase in the background noise is also possible due to the small amount of sample placed on an amorphous glass sample holder.

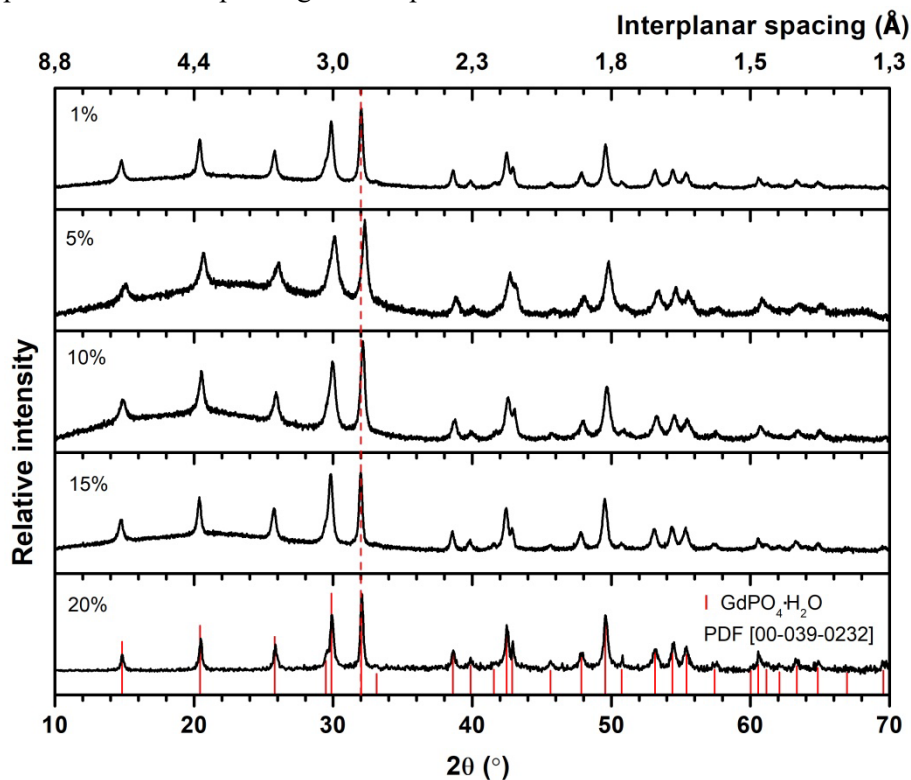


Fig. 8. XRD of $\text{Gd}_{1-x}\text{PO}_4:\text{Eu}_x \cdot \text{H}_2\text{O}$ containing different content of europium.

Additionally, to support the XRD data and characterize the morphology of particles SEM technique has been used. The obtained results are displayed in Figure 9. From the given images it can be clearly seen that independently of europium content the particles form in the shape of an elongated rod, that

then aggregate into larger clusters. The concentration of Eu^{3+} in the sample does not affect the particle shape. Using Fiji software, particle lengths and widths were measured from SEM images. The particle length and width distribution results are shown in Table 1. The measured average particle sizes are similar in all samples. The size of the particles slightly varies therefore it can be said that the Eu^{3+} concentration does not dramatically affect the particle size formed.

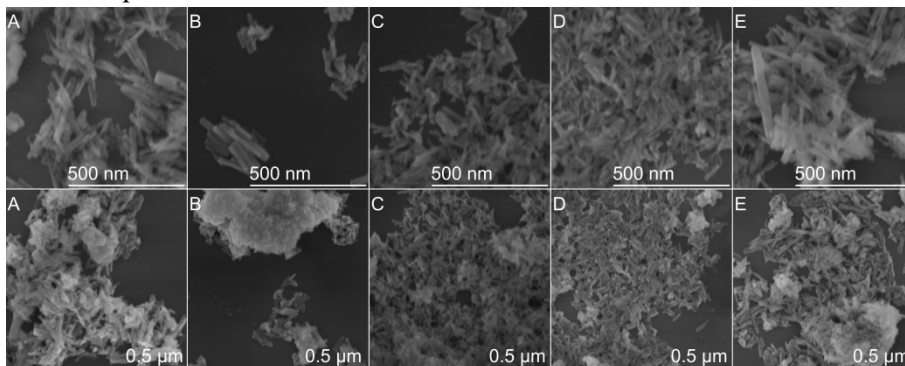


Fig. 9. SEM images of $\text{Gd}_{1-x}\text{PO}_4:\text{Eu}_x \cdot \text{H}_2\text{O}$ synthesized by hydrothermal method: A) $x = 0.01$, B) $x = 0.05$, C) $x = 0.1$, D) $x = 0.15$ and E) $x = 0.2$.

Table 1. The average particle length and width of $\text{Gd}_{1-x}\text{PO}_4:\text{Eu}_x \cdot \text{H}_2\text{O}$.

Sample	Length, nm	Standart deviation, nm	Width, nm	Standart deviation, nm	Length to width ratio
1% of Eu^{3+}	118	37	19	7	6.3
5% of Eu^{3+}	108	48	21	7	5.3
10% of Eu^{3+}	94	20	17	7	5.4
15% of Eu^{3+}	88	22	18	5	5.0
20% of Eu^{3+}	123	66	22	7	5.5

The emission spectra of the synthesized powders are given in Figure 10. The emission spectra were recorded under 392.5 nm excitation. Red colour phosphors contain all $^5\text{D}_0 \rightarrow ^7\text{F}_j$ transitions that are characteristic for the Eu^{3+} ion: $^5\text{D}_0 \rightarrow ^7\text{F}_0$, $^5\text{D}_0 \rightarrow ^7\text{F}_1$, $^5\text{D}_0 \rightarrow ^7\text{F}_2$, $^5\text{D}_0 \rightarrow ^7\text{F}_3$, and $^5\text{D}_0 \rightarrow ^7\text{F}_4$. The most intensive characteristic peaks are observed at ~ 577 nm, ~ 590 nm, ~ 615 nm, ~ 650 nm, and ~ 690 nm, and are ascribed to the aforementioned transitions. The $^5\text{D}_0 \rightarrow ^7\text{F}_4$ transitions are the most dominant. Note, that the intensity of emission gradually increases with increasing the content of europium from 1 to 15 mol%. However, upon reaching 20% the emission

intensity decreases. The maximum point of europium concentration is reached, and the concentration quenching is observed, causing the lower intensity of $\text{Gd}_{0.80}\text{Eu}_{0.20}\text{PO}_4\cdot\text{H}_2\text{O}$ sample emission as compared to the $\text{Gd}_{0.85}\text{Eu}_{0.15}\text{PO}_4\cdot\text{H}_2\text{O}$ sample. All the mentioned results allow us to determine that from the presented compounds, a sample doped with 15% of europium shows the most promise and will for further measurements and analysis samples doped with such Eu^{3+} content I be used.

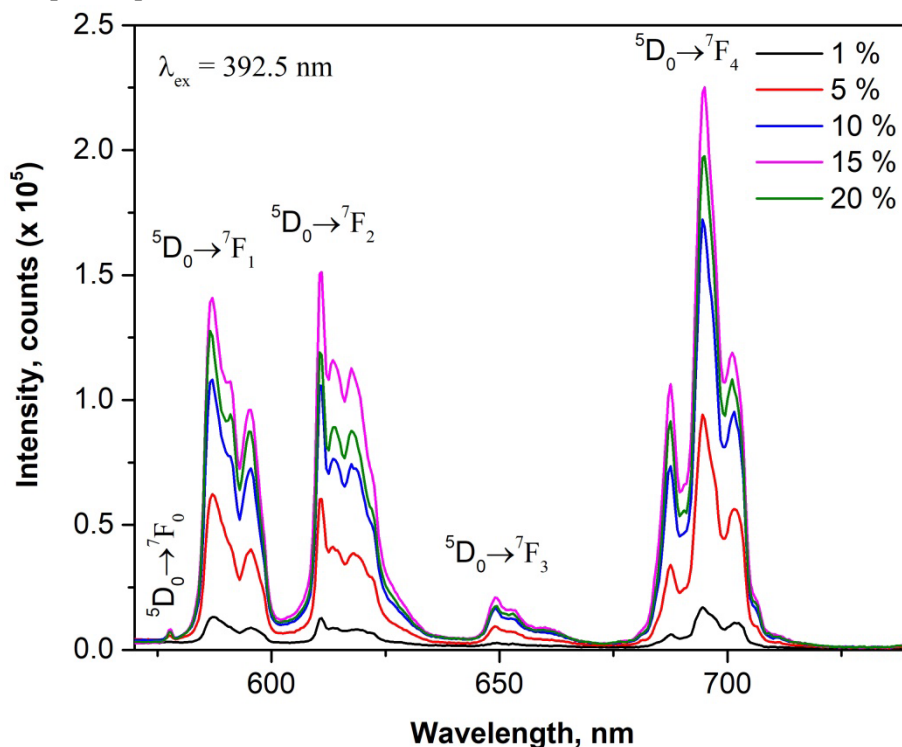


Fig. 10. Emission spectra of $\text{Gd}_{1-x}\text{PO}_4:\text{Eu}_x\cdot\text{H}_2\text{O}$ containing different content of europium.

In order to investigate the behaviour of the samples in a more realistic setting luminescence properties of sample demonstrating the most intensive emission have been tested in different solutions. The samples were prepared by mixing $\text{Gd}_{0.85}\text{Eu}_{0.15}\text{PO}_4\cdot\text{H}_2\text{O}$ with water in proportions of 1 mg-10 mL or with Dulbecco's Modified Eagle Medium (DMEM) in proportions of 0.5 mg-3 mL. The resulting emission spectra are given in Figure 11. The clear signal of europium emission is observed in water meanwhile, the emission of europium is overshadowed by the autofluorescence of the DMEM solution clearly indicating that in order to use synthesized particles for bioimaging luminescence should be further improved.

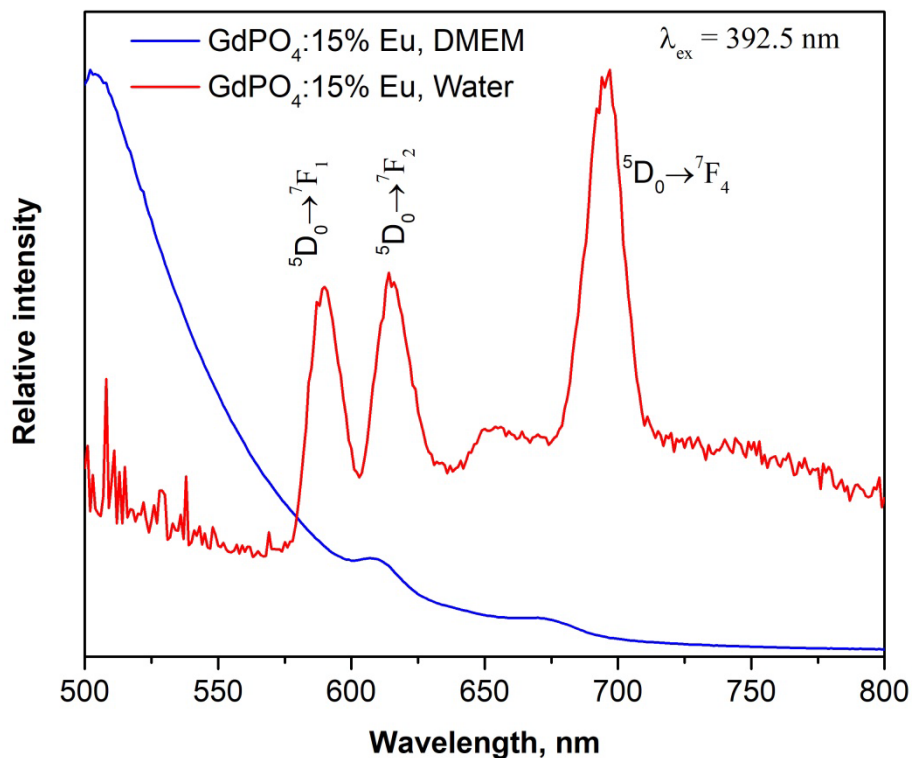


Fig. 11. Emission spectra of GdPO₄:15%Eu samples in DMEM and water solution.

3.2. Investigation of the dependence of the Gd_{0.85}Eu_{0.15}PO₄·H₂O nanoparticle size on the reactor volume

Since it is very important to be able to obtain nanoparticles of the desired size, sintezys were performed by changing the by changing the volume of filling the hydrothermal reactor with water. X-ray diffraction studies were performed to investigate all synthesized samples phase composition and purity. Regardless of the synthesis conditions, XRD analysis of all samples showed that a uniform phase composition was obtained. The XRD patterns of Gd_{0.85}Eu_{0.15}PO₄·H₂O samples corresponds to reference data of hexagonal Gadolinium Phosphate Hydrate (space group P3121 (152), cell parameters of reference compound a=6.9055 Å c=6.3257 Å, cell volume 261.2300 Å³; PDF ICDD 00-039-0232). Based on this database, it has obtained a pure rhabdophane-type phase. A small shift of all peaks toward smaller 2θ values is observed in all samples. This is due to the fact that Gd³⁺ ions (1.06 Å) have been replaced by slightly larger Eu³⁺ ions (1.07 Å) [38], resulting in a shift that follows the Bragg's Law . In some cases, it is seen an increase in

the background. The increase in background in samples that have been synthesized under pH = 1 and V = 10 mL, V = 20 mL, V = 30 mL conditions is due to the formation of smaller particle sizes under different synthesis conditions. The particle size will be discussed in detail in the section of SEM data. With the formation of larger particles, the intensity of the peaks increases and the noise of the background decreases (Figure 12).

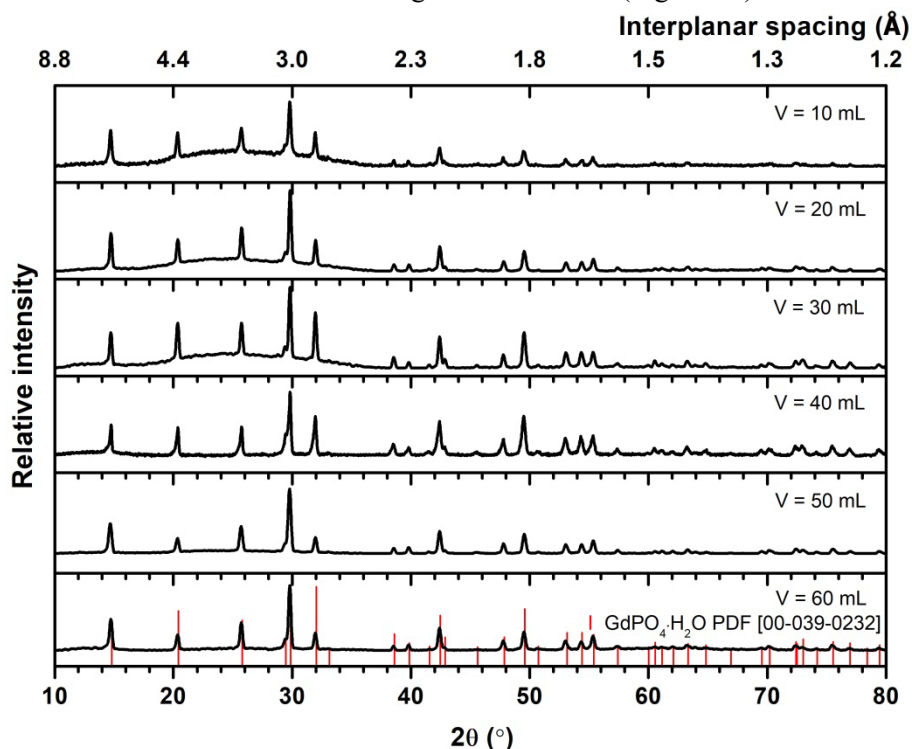


Fig. 12. XRD patterns of $\text{Gd}_{0.85}\text{Eu}_{0.15}\text{PO}_4 \cdot \text{H}_2\text{O}$ samples were synthesized using different amounts of solvent (H_2O) in the hydrothermal autoclave reactor.

SEM study was performed to investigate the morphology of the synthesized particles. The synthesized particles are in the form of a rod, but under a different selected total volume of solvent, the size and length of particles are controlled (Figure 13). Using Fiji software, particle lengths and widths were measured from SEM images by choosing random 100 particles. The particle length and width distribution results are shown in histograms Figure 14. In the histograms, it is observed that if the smallest volume $V = 10$ mL is used for the synthesis, the smallest particles are obtained: the length varies from 50 nm to 450 nm and the width from 30 nm to 110 nm. Doubling the volume $V = 20$ mL increases the particle length dramatically

from 500 nm to 1800 nm and the width from 20 nm to 180 nm. This can be explained by the fact that increasing the volume decreases the solution concentration, and it is known that the higher the concentration of the solution, the lower the energy barrier for nucleation [144]. This means that crystals nucleate faster, and more particles are obtained but smaller. Further increase in volume $V = 30$ mL and the corresponding decrease in solution concentration results in slightly shorter 200 nm–1100 nm but larger diameter 10 nm–400 nm particles. The particles synthesized at higher volumes $V = 40$ mL, $V = 50$ mL, and $V = 60$ mL of solution are obtained in not regular sizes resulting in both fine particles and large ones.

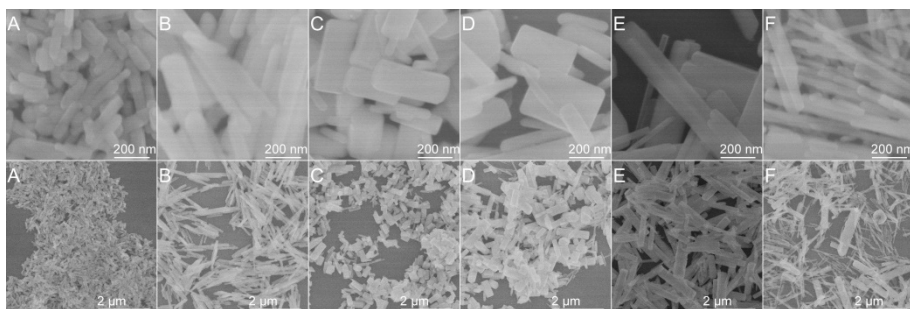


Fig. 13. SEM images of $\text{Gd}_{0.85}\text{Eu}_{0.15}\text{PO}_4 \cdot \text{H}_2\text{O}$ synthesized using different amount of solvent (H_2O) in reactor of hydrothermal autoclave: (A) $V = 10$ mL, (B) $V = 20$ mL, (C) $V = 30$ mL, (D) $V = 40$ mL, (E) $V = 50$ mL, (F) $V = 60$ mL.

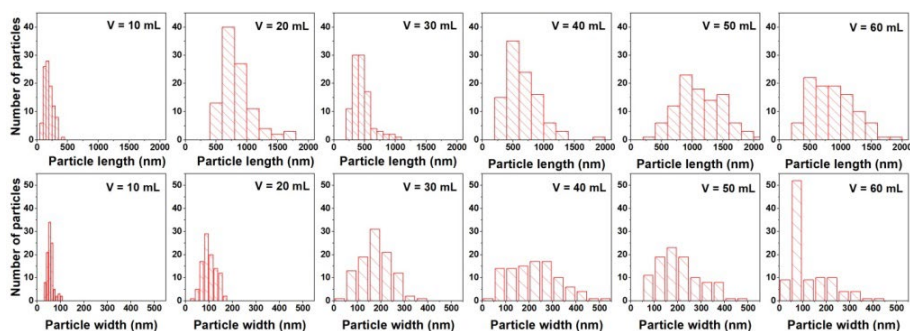


Fig. 14. Histograms of nanorods length and width of $\text{GdPO}_4 \cdot \text{H}_2\text{O}$ were synthesized using different amounts of solvent (H_2O) in the hydrothermal autoclave reactor.

The luminescent properties of all samples synthesized under different conditions were studied (Figure 15 and 16). All $\text{Gd}_{0.85}\text{Eu}_{0.15}\text{PO}_4 \cdot \text{H}_2\text{O}$ samples were pure white, so the samples should have low or no absorption in

the visible spectrum range. The Excitation spectra were recorded in the range from 250 nm to 585 nm upon emission wavelength $\lambda_{em} = 591$ nm. The excitation spectra consist of the part of broadband at higher energy (from 250 nm to 270 nm) range. This is due to charge transfer and results from the electron transfer from O^{2-} to Eu^{3+} . Narrow peaks at the 275 nm and 310 nm range are assigned to ${}^8S \rightarrow {}^6I_J$ and ${}^8S \rightarrow {}^6P_J$ transitions of Gd^{3+} ions. The presence of Gd^{3+} excitation lines in excitation spectra monitored for Eu^{3+} ion proves the occurring $Gd^{3+} \rightarrow Eu^{3+}$ energy transfer. The remaining excitation peaks are assigned to the Eu^{3+} ion. The peaks at 362 nm are assigned to the transitions of ${}^7F_0 \rightarrow {}^5D_4$. In the range from 370 nm to 390 nm, a group of several peaks is visible, which is assigned to the ${}^7F_0 \rightarrow {}^5L_{7,8}$ and ${}^7F_0 \rightarrow {}^5G_{2,4,5,6}$ transitions. The most intense peak at 394 nm is attributed to transition ${}^7F_0 \rightarrow {}^5L_6$. The small peaks at 465 nm and 527 nm are assigned to the transitions of ${}^7F_0 \rightarrow {}^5D_2$ and ${}^7F_0 \rightarrow {}^5D_1$, respectively.

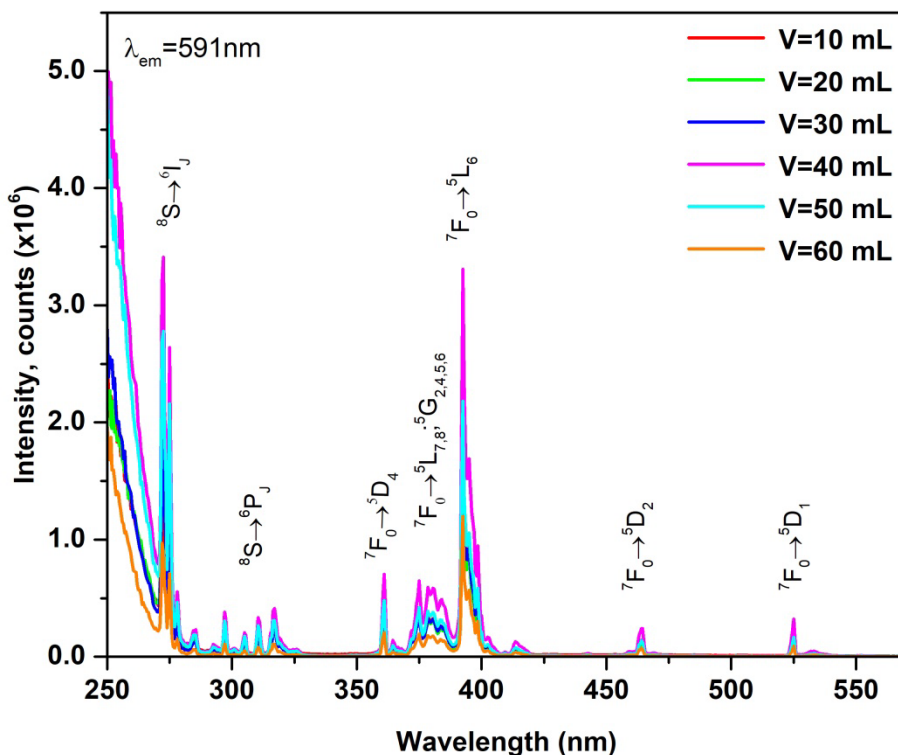


Fig. 15. Excitation spectra of $Gd_{0.85}Eu_{0.15}PO_4 \cdot H_2O$ samples synthesized under different amounts of solvent (H_2O).

Performing emission spectrum measurements, all samples of $Gd_{0.85}Eu_{0.15}PO_4 \cdot H_2O$ were excited under wavelength $\lambda_{ex} = 393$ nm. The

emission spectrum shows that the radiation received is in the red colour range. The emission spectral peaks at ~ 577 nm, ~ 590 nm, ~ 615 nm, ~ 650 nm and ~ 690 nm attributed to ${}^5D_0 \rightarrow {}^7F_0$, ${}^5D_0 \rightarrow {}^7F_1$, ${}^5D_0 \rightarrow {}^7F_2$, ${}^5D_0 \rightarrow {}^7F_3$, and ${}^5D_0 \rightarrow {}^7F_4$ respectively. It should be noted that the peak at 577 nm is minimal. Nevertheless, it indicates the emission is permitted as a dipolar electric transition for local C_s , C_n or C_{nv} sites. The peak of maximum intensity is observed at 690 nm. This is typical for Eu^{3+} doped orthophosphates [145]. Moreover, it is described in the literature that if the europium emission ratio of ${}^5D_0 \rightarrow {}^7F_2 / {}^5D_0 \rightarrow {}^7F_1$ is less than or equal to one when there is a high symmetry environment, and conversely, the lower the symmetry, the higher the ratio is [25]. Calculations of the relative intensities of emission ratio were performed, and the result is presented in Table 2. The symmetry of the investigated all synthesized samples is high. Calculations of relative integral intensities ${}^5D_0 \rightarrow {}^7F_4$ emissions (680-709 nm) compared to emission intensity in the range of 520 nm–750 nm was also performed. The result is presented in Table 2. The transition ${}^5D_0 \rightarrow {}^7F_4$ is dominant, and around 40% of the emissions fall in the 680–709 nm band that falls within the bandwidth of the human body transmits light.

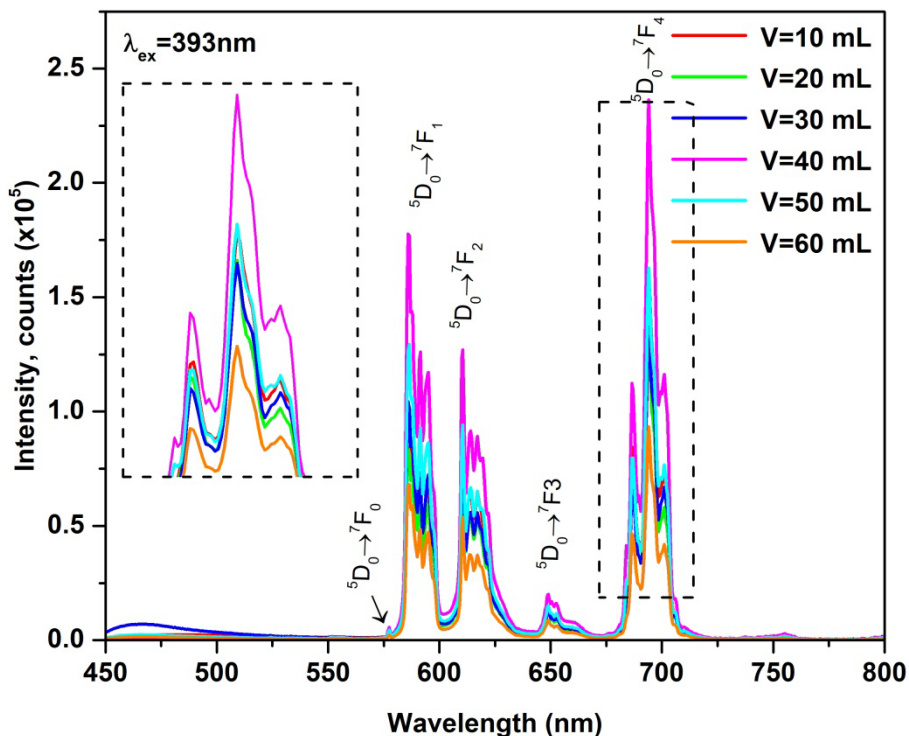


Fig. 16. Emission spectra of $\text{Gd}_{0.85}\text{Eu}_{0.15}\text{PO}_4 \cdot \text{H}_2\text{O}$ samples synthesized under different amounts of solvent (H_2O).

Table 2 Relative integral intensities of ${}^5D_0 \rightarrow {}^7F_2 / {}^5D_0 \rightarrow {}^7F_1$ emission line and ${}^5D_0 \rightarrow {}^7F_4$ emission line expressed in percent of total emission.

Sample	${}^5D_0 \rightarrow {}^7F_2 / {}^5D_0 \rightarrow {}^7F_1$	${}^5D_0 \rightarrow {}^7F_4 / \text{total emission}$
V = 10 mL	1.0	40.6
V = 20 mL	1.0	40.6
V = 30 mL	0.9	38.3
V = 40 mL	0.8	40.3
V = 50 mL	0.8	38.4
V = 60 mL	0.9	38.3

Table 3 Measured length, width, standart deviation and length to width ratio of nanoparticles prepared at different filling volumes.

Sample	Length, nm	Standart deviation, nm	Width, nm	Standart deviation, nm	Length to width ratio
V = 10 mL	194	71	58	14	3.3
V = 20 mL	835	268	103	28	8.1
V = 30 mL	455	157	178	64	2.6
V = 40 mL	658	276	224	104	2.9
V = 50 mL	1121	381	207	89	5.4
V = 60 mL	865	349	124	85	7.0

Note, the sample synthesized at volume V = 40 mL demonstrates the highest emission. After calculating the average particle length and width values for all samples, it was obtained that the width of the particles synthesized at volume V = 40 mL is the largest 223 nm. Moreover, the mean particle length and width ratios for all samples synthesized under different conditions were also calculated. The lowest values of the ratio (Table 3) (2.6 and 2.9, respectively) were obtained for samples synthesized at volume V = 30 mL and volume V = 40 mL, indicating the luminescent centers of the particles in these samples are more in bulk than on the surface. As it is known, typically, the largest bulk crystals have the highest intensity of emission.

For these reasons, even the ratio of the sample synthesized at volume V = 30 mL is smaller (2.6) indicating more luminescent centers in the bulk compared to the sample synthesized at volume V = 50 mL (5.4) though the size of the particles themselves are noticeably larger (Figure 13 C and E and Figure 14) of the sample synthesized at volume V = 50 mL causing almost the same intensity of the emission of both samples. Concluding, there is a

competition between the particle size (length) and the length on width ratio but probably the width is the most important factor. The particles of the sample synthesized at $V = 40$ demonstrate the optimal size and the best ratio value of investigated samples resulting in the most intensive emission.

3.3. Effect of doping by lanthanum on structure and luminescence properties of $\text{Gd}_{0.85-y}\text{La}_y\text{PO}_4:15\%\text{Eu}$

To further improve the luminescence properties, samples were additionally doped with lanthanum in hopes of stabilizing the monoclinic structure. Three different La doped samples were prepared to contain 25%, 50%, and 75% of lanthanum. The diffraction patterns for the obtained samples are displayed in Figure 17.

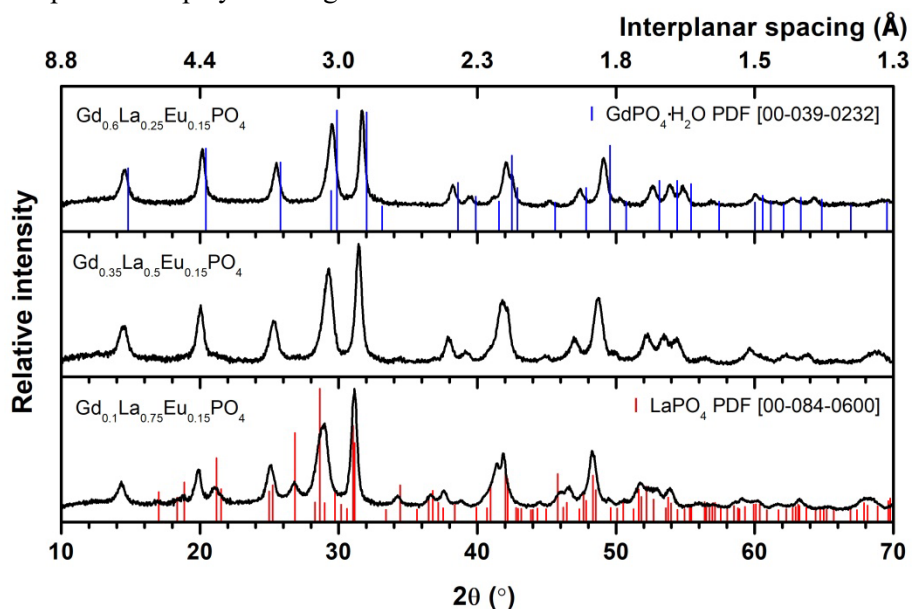


Fig. 17. XRD of $\text{Gd}_{0.85-y}\text{La}_y\text{PO}_4:15\%\text{Eu}$ containing different content of lanthanum

From the given XRD results some of the synthesized compounds are not a single phase and contain a mixture of two different crystal structures (Figure 17). The $\text{Gd}_{0.1}\text{La}_{0.75}\text{Eu}_{0.15}\text{PO}_4$ sample contains two-phase composition with monoclinic (PDF ICDD 00-084-0600) and hexagonal (PDF ICDD 00-039-0232) crystal structures. By decreasing La and increasing the amount of Gd in the sample accordingly, we still have a two-phase system. In the $\text{Gd}_{0.35}\text{La}_{0.5}\text{Eu}_{0.15}\text{PO}_4$ sample, at 21° , 27° , and 34° 2θ values, additional, small peaks are visible that correspond to the monoclinic

crystalline system. With a decrease in the amount of La to 25% for the $\text{Gd}_{0.6}\text{La}_{0.25}\text{Eu}_{0.15}\text{PO}_4$ sample, no additional peaks of the hexagonal crystal system were found, as such indicating a formation of a single-phase material. The width of the peaks does not change. This suggests that the size of crystallite size is not affected by lanthanum doping.

The SEM images are given in Figure 18 show particles adhering to larger derivatives. Individual particles can also be found in certain places. The size of adhering and detached particles was measured using Fiji software. Particle's average size of $\text{Gd}_{0.6}\text{La}_{0.25}\text{PO}_4:15\%\text{Eu}$, $\text{Gd}_{0.35}\text{La}_{0.5}\text{PO}_4:15\%\text{Eu}$, and $\text{Gd}_{0.35}\text{La}_{0.5}\text{PO}_4:15\%\text{Eu}$ is 115 nm, 92 nm, and 122 nm, respectively. Individual particles all show a nanorod shape.

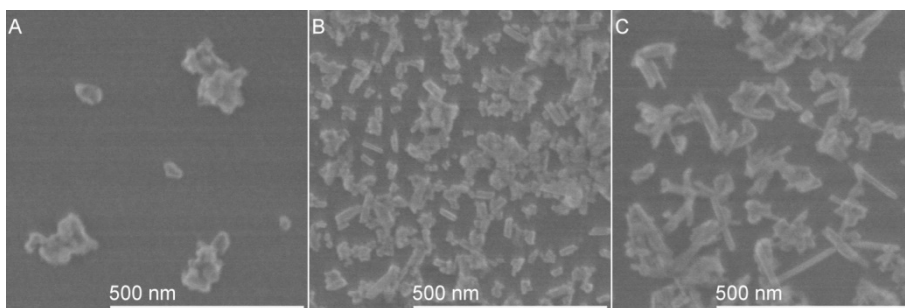


Fig. 18 SEM images of $\text{Gd}_{0.85-y}\text{La}_y\text{PO}_4:15\%\text{Eu}$: A) $\text{Gd}_{0.6}\text{La}_{0.25}\text{PO}_4:15\%\text{Eu}$, B) $\text{Gd}_{0.35}\text{La}_{0.5}\text{PO}_4:15\%\text{Eu}$, C) $\text{Gd}_{0.1}\text{La}_{0.75}\text{PO}_4:15\%\text{Eu}$.

The luminescent properties of $\text{Gd}_{0.85-y}\text{La}_y\text{PO}_4:15\%\text{Eu}$ samples were also studied. The Excitation spectra were recorded in the range from 250 nm to 500 nm at emission wavelength $\lambda_{\text{em}} = 587$ nm (Figure 19). The excitation spectra consist of a broad band at higher energy up to 270 nm. This is due to charge transfer from between O^{2-} to Eu^{3+} ions. Peaks observed at ~ 275 nm and ~ 298 nm are assigned to ${}^8\text{S}_{7/2} \rightarrow {}^6\text{I}_{11/2}$, and ${}^8\text{S}_{7/2} \rightarrow {}^6\text{P}_J$ transitions of the Gd^{3+} ion. For the sample with the lowest Gd content ($\text{Gd}_{0.1}\text{La}_{0.75}\text{PO}_4:15\%\text{Eu}$), the peak at ~ 275 nm is not observed due to the high intensity of the peak of electron transfer from O^{2-} to Eu^{3+} . The presence of Gd^{3+} excitation lines in excitation spectra monitored for Eu^{3+} ion proves the occurring $\text{Gd}^{3+} \rightarrow \text{Eu}^{3+}$ energy transfer. The remaining excitation peaks are assigned to the Eu^{3+} ion. The peaks at ~ 318 nm, are assigned to the ${}^7\text{F}_0 \rightarrow {}^5\text{H}_J$ transitions. In the range from ~ 360 nm to ~ 400 nm, a group of several peaks is visible which are assigned to the ${}^7\text{F}_0 \rightarrow {}^5\text{D}_4$ and ${}^7\text{F}_0 \rightarrow {}^5\text{G}_J$, ${}^7\text{F}_0 \rightarrow {}^5\text{G}_J$; ${}^5\text{L}_7$ transitions, respectively. The most intense peak at ~ 393 nm is attributed ${}^7\text{F}_0 \rightarrow {}^5\text{L}_6$ transition. The small peaks at ~ 415 nm and ~ 463 nm is assigned to the ${}^7\text{F}_0 \rightarrow {}^5\text{D}_3$, ${}^7\text{F}_0 \rightarrow {}^5\text{D}_2$ transitions.

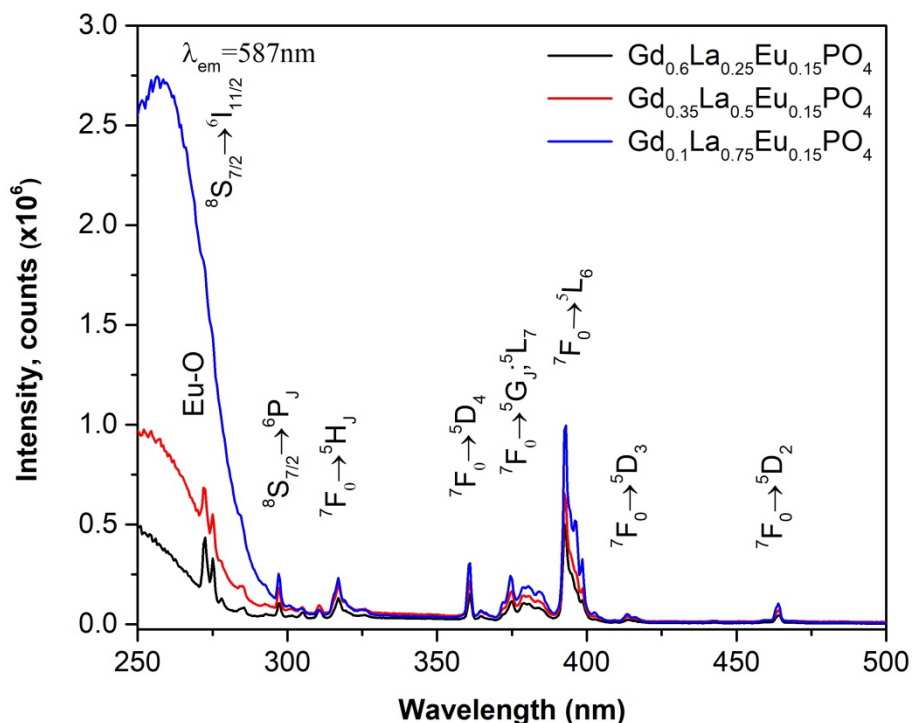


Fig. 19. Excitation spectra of $\text{Gd}_{0.85-y}\text{La}_y\text{PO}_4:15\%\text{Eu}$.

The emission spectra were also recorded for all samples $\text{Gd}_{1-y}\text{La}_y\text{PO}_4:15\%\text{Eu}$ in the range from 450 nm to 800 nm. The compounds were excited with 393 nm wavelength light and the results are shown in Figure 20. Based on the emission spectra data, the resulting emitted light is in the orange to red range. The emission spectral peaks at ~ 577 nm, ~ 590 nm, ~ 615 nm, ~ 650 nm and ~ 690 nm attributed to ${}^5\text{D}_0 \rightarrow {}^7\text{F}_0$, ${}^5\text{D}_0 \rightarrow {}^7\text{F}_1$, ${}^5\text{D}_0 \rightarrow {}^7\text{F}_2$, ${}^5\text{D}_0 \rightarrow {}^7\text{F}_3$, and ${}^5\text{D}_0 \rightarrow {}^7\text{F}_4$ transitions respectively. At 577 nm we see a very intensity peak. At 690 nm we observed the peak of maximum intensity. This is typical for Eu^{3+} doped orthophosphates [145].

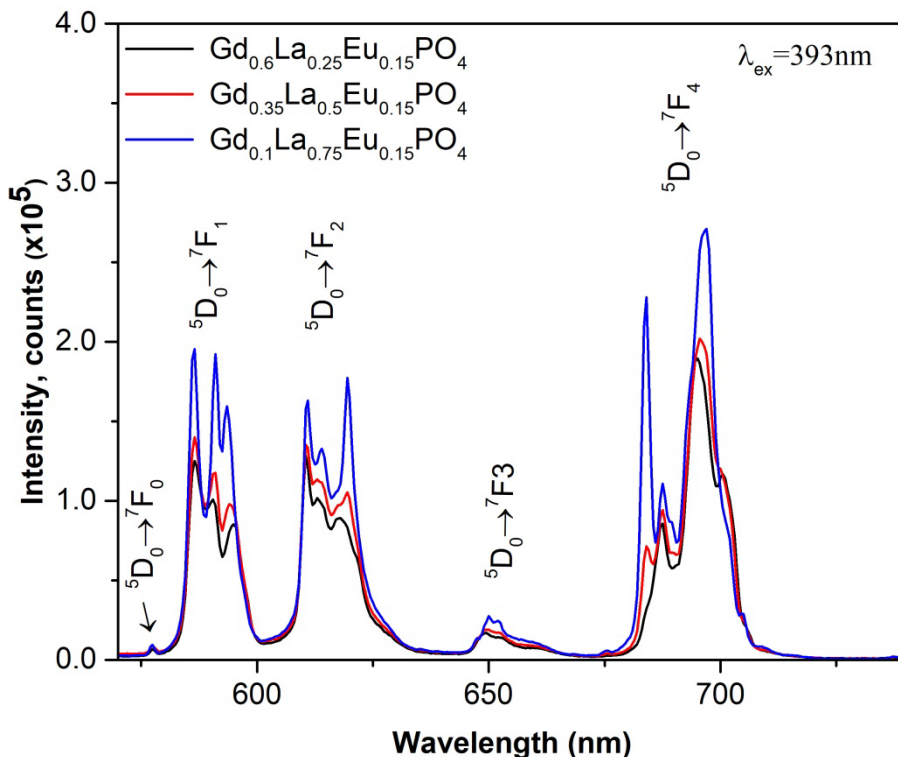


Fig. 20. Emission spectra of Gd_{0.85-y}La_yPO₄:15%Eu.

To determine the surface area of the compounds Nitrogen adsorption measurements by the Brunauer, Emmet, and Teller (BET) method were performed. The resulting N₂ adsorption-desorption isotherms for all Gd_{0.85-y}La_yPO₄:15%Eu samples have the same shape and can be assigned to one group (Figure 21). According to the IUPAC classification Isotherms of all samples are classified as type IV (a). At higher pressure values H1-type of hysteresis loops are observed [147]. Based on the descriptions of this type of isotherms, it can be stated that the sample contains mesoporous.

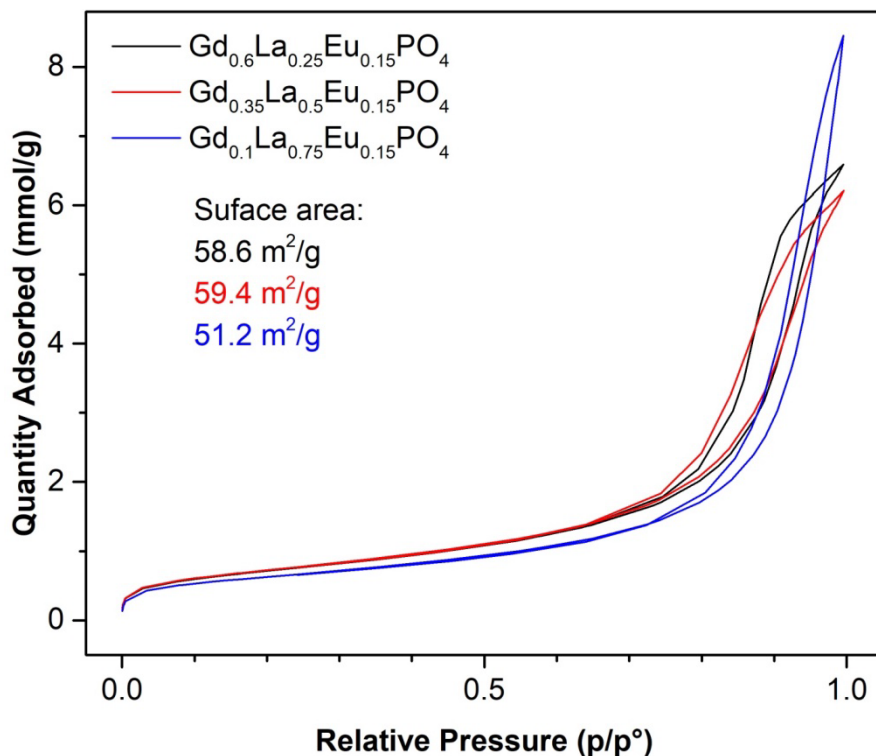


Fig. 21. Nitrogen adsorption-desorption isotherms of $\text{Gd}_{0.85-y}\text{La}_y\text{PO}_4:15\%\text{Eu}$ samples.

The pore size distribution of all $\text{Gd}_{0.85-y}\text{La}_y\text{PO}_4:15\%\text{Eu}$ samples is shown in Figure 22. The measurements were performed by the BJH method. All samples show a wide mesopore size distribution. $\text{Gd}_{0.6}\text{La}_{0.25}\text{PO}_4:15\%\text{Eu}$ and $\text{Gd}_{0.35}\text{La}_{0.5}\text{PO}_4:15\%\text{Eu}$ samples exhibit a size distribution ranging from 2 nm to 50 nm, meanwhile, the mesopores with sizes 12 nm and 15 nm, respectively, are dominant. $\text{Gd}_{0.1}\text{La}_{0.75}\text{PO}_4:15\%\text{Eu}$ sample demonstrates an even wider size distribution of the mesopores (from 2 nm to 80 nm), and the dominant contribution of mesopores with a size of 19 nm. Note, that pores above 50 nm are classified as macropores [148], but the amount of such pores is not significant. Probably these pores are not formed on the particle itself, but in the gaps between their aggregates.

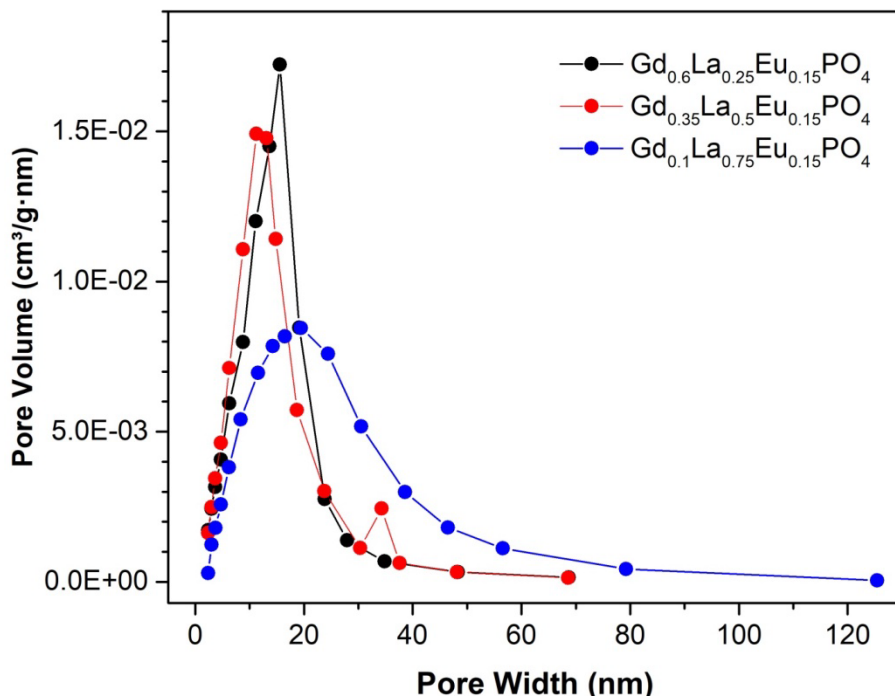


Fig. 22. The Pore width of Gd_{0.85-y}La_yPO₄:15%Eu samples.

3.4. Biological evaluation of Gd_{0.85-y}La_yPO₄:15%Eu samples

Cytotoxicity testing is required for the use of nanomaterials for bio-imaging and cell labelling, as only non-toxic substances may be used. Analysis was performed on Gd_{0.85-y}La_yPO₄:15%Eu samples to assess cell viability depending on extract concentration.

Figure 23 shows that cell viability decreased with increasing extract concentration in all samples. In particular, the degree of decrease in Gd_{0.6}La_{0.25}PO₄:15%Eu was more remarkable than in the other two samples. The cell viability of the three control samples was RM-A < RM-B < NC, which was consistent with the trend of cytotoxicity of the control samples, and this evaluation was judged to be appropriate. For further evaluation, an approximate curve was drawn by logistic regression [149], and the extract concentration at which the cell viability was 50% (IC₅₀) was converted and compared. The IC₅₀ of Gd_{0.1}La_{0.75}PO₄:15%Eu, Gd_{0.35}La_{0.5}PO₄:15%Eu, and NC exceeded 100% of the extract dilution. On the other hand, the IC₅₀ of Gd_{0.6}La_{0.25}PO₄:15%Eu, RM-A and RM-B were 97.4%, 27.3%, and 51.1%, respectively. This means that the cytotoxicity of the three samples was lower than that of RM-B, which exhibited weak cytotoxicity. In particular,

$Gd_{0.1}La_{0.75}PO_4:15\%Eu$, and $Gd_{0.35}La_{0.5}PO_4:15\%Eu$ showed similar cytocompatibility to NC when evaluated using IC50.

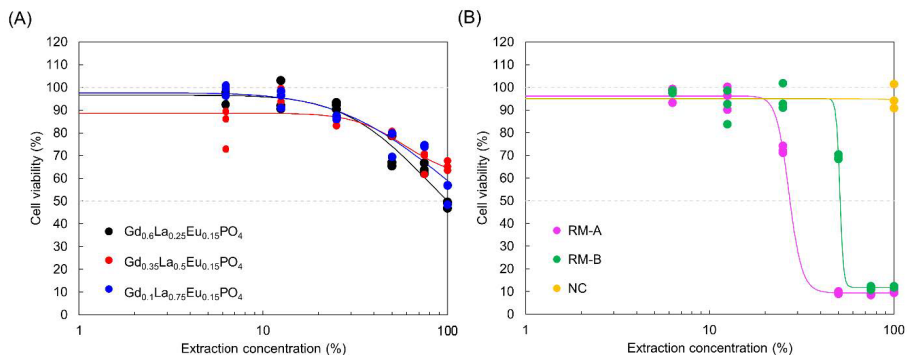


Fig. 23. Cell viability against extract: (A) samples, (B) controls

Figure 24 shows the optical microscopic images of all samples in 100% extract. In RM-A and RM-B, spherical cells were observed, and cells were not adherent to the wells. While, in the three samples and NC, L929 cells were observed to be elongated into a spindle shape with a size of about 100 μm , and the cells were adherent to the wells. These images are consistent with typical L929 responses to cytotoxicity [150]. This suggests that the three samples were less cytotoxic.

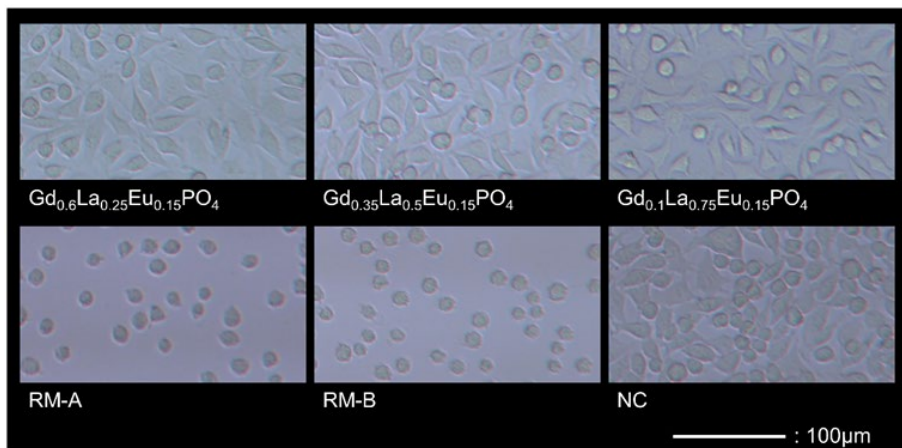


Fig. 24. Optical microscopy images of L929 cells with 100% extract of each sample

These cytotoxicity studies indicate that the synthesized and tested the $\text{Gd}_{0.1}\text{La}_{0.75}\text{PO}_4:15\%\text{Eu}$ and, $\text{Gd}_{0.35}\text{La}_{0.5}\text{PO}_4:15\%\text{Eu}$, samples are non-toxic and the $\text{Gd}_{0.6}\text{La}_{0.25}\text{PO}_4:15\%\text{Eu}$ sample is slightly toxic.

3.5. Investigation of synthesis conditions of monoclinic structure $\text{Gd}_{0.85-y}\text{La}_y\text{PO}_4:15\%\text{Eu}$ and study of luminescent properties

In order to synthesize the monoclinic structure of $\text{Gd}_{0.85-y}\text{La}_y\text{PO}_4:15\%\text{Eu}$, it was decided to find out the conditions for the synthesis of $\text{LaPO}_4:1\%\text{Eu}$. For economic reasons, it was decided to dope LaPO_4 with 1 percent of Eu^{3+} . First of all, it was aimed to clarify the influence of PO_4^{3-} ion precursor and synthesis temperature on $\text{LaPO}_4:1\%\text{Eu}$ structure. XRD was performed in order to determine the crystal structure of the $\text{LaPO}_4:\text{Eu}$ synthesized in the hydrothermal reactor, and to assess the purity of the phase. If diammonium hydrogen phosphate $(\text{NH}_4)_2\text{HPO}_4$ is used as a precursor of PO_4^{3-} ions, in Figure 25 we see that at different synthesis temperatures two different crystal structures of $\text{LaPO}_4:1\%\text{Eu}$ are formed.

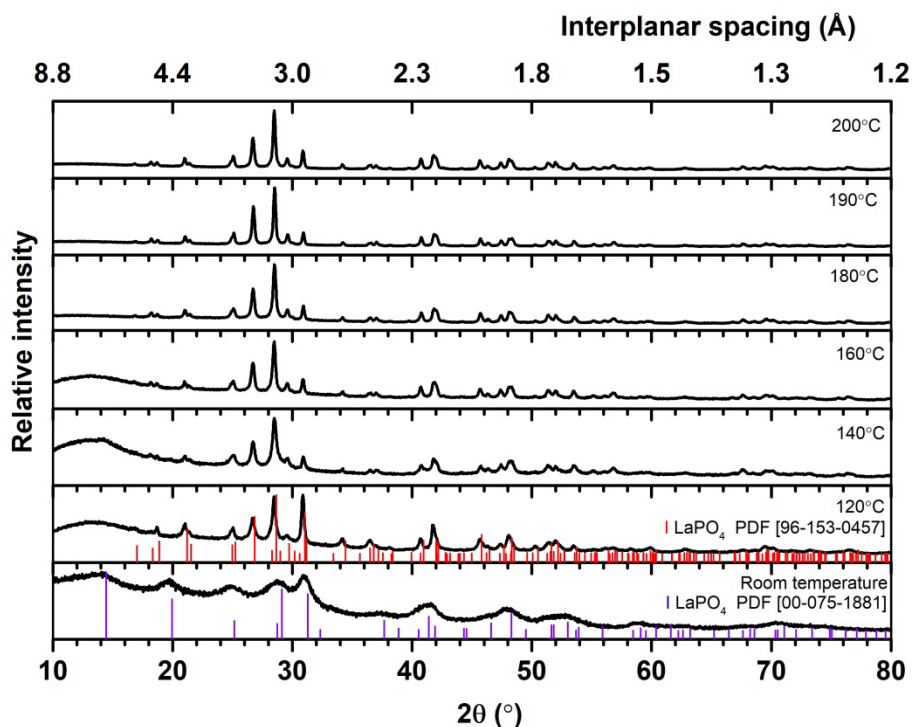


Fig. 25. XRD patterns of $\text{LaPO}_4:1\%\text{Eu}$ samples synthesized using $(\text{NH}_4)_2\text{HPO}_4$ at different temperatures.

Analyzing the diffractograms and comparing the obtained data with the reference in database, we can see that, at a synthesis temperature higher than or equal to 160 °C, peaks and their relative intensities of experimental XRD data agree with the standard data of the monoclinic LaPO₄ structure (PDF ICCD 96-153-0457). The single-phase LaPO₄:1%Eu with a monoclinic crystal structure is formed. At a lower synthesis temperature, 140 °C and lower, the peaks attributed to monoclinic phase is still dominant, nevertheless a observable peak at 14.4° characteristic of the hexagonal crystal structure of LaPO₄ (PDF ICCD 00-075-1881) and the peak at 28.6° degrees is asymmetric and is broadened towards higher 2θ values, this can be explained by the same hexagonal structure of the peak at 29.1°. Therefore, it can be said that a two-phase crystal structure is formed, the hexagonal and monoclinic crystal structure of LaPO₄. Meanwhile, at room temperature a low crystallinity pure hexagonal phase is obtained. It should also be noted that the synthesis performed at room temperature can not be called the synthesis performed in a hydrothermal reactor, it should be called the LaPO₄:1%Eu obtained by the precipitation method.

A wide band at a range from 10° to 20° is also observed. The origin of it could be attributed to the amorphousness of the synthesized material itself or the influence of the amorphous glass tray on which the research material was placed. Since all materials were prepared in the same way during the XRD analysis, we can see in the diffractograms that the band from 10° to 20° disappears when the synthesis temperature is higher than 180 °C. Thus, it is the influence of the amorphousness of the material itself. To conclude, even 120 °C temperature is high enough to obtain the dominant monoclinic LaPO₄:1%Eu phase dominant, but the pure monoclinic crystal structure phase is obtained only at 180 °C and higher temperatures if diammonium hydrogen phosphate ((NH₄)₂HPO₄) is used as a precursor of PO₄³⁻ ions.

A series of syntheses was also performed in a hydrothermal reactor using ammonium dihydrogen phosphate (NH₄H₂PO₄) as a precursor of PO₄³⁻ ions.

The diffractograms of the XRD analysis are presented in the Figure 26. In the diffractograms, we can see that only at the synthesis temperature of 200 °C, single-phase of LaPO₄:1%Eu with a monoclinic crystal structure is obtained. There are no additional peaks in this diffractogram. At a synthesis temperature lower than 200 °C a low intensity peak corresponding to of the hexagonal crystal structure of LaPO₄ (PDF ICCD 00-075-1881) is visible at 14.4° and we also see the asymmetry of the peak at 29.1°. At the synthesis temperature of 140 °C, peak at 14.4° becomes more prominent and peak at 29.1° starts to separate. Therefore, it can be stated that two-phase LaPO₄:1%Eu is obtained at a lower synthesis temperature than 200 °C. As

well as in the previous synthesized $\text{LaPO}_4:1\%\text{Eu}$ series, a wide peak at 10° to 20° is present at 180°C and lower temperatures, which could be the amorphousness of the synthesized material itself.

Thus, comparing the diffractograms of the first series synthesis when diammonium hydrogen phosphate was used as the PO_4^{3-} ion precursor and the second one when ammonium dihydrogen phosphate was used as the PO_4^{3-} -ion precursor, it is concluded that the ion precursor affects the temperature under the pure monoclinic crystal structure final product of the synthesized $\text{LaPO}_4:1\%\text{Eu}$ is formed. Using $(\text{NH}_4)_2\text{HPO}_4$, the pure monoclinic phase is formed at a lower temperature of 180°C , while using $\text{NH}_4\text{H}_2\text{PO}_4$, the pure monoclinic phase is formed only at the synthesis temperature of 200°C , the hexagonal phase impurity is clearly visible at lower temperatures.

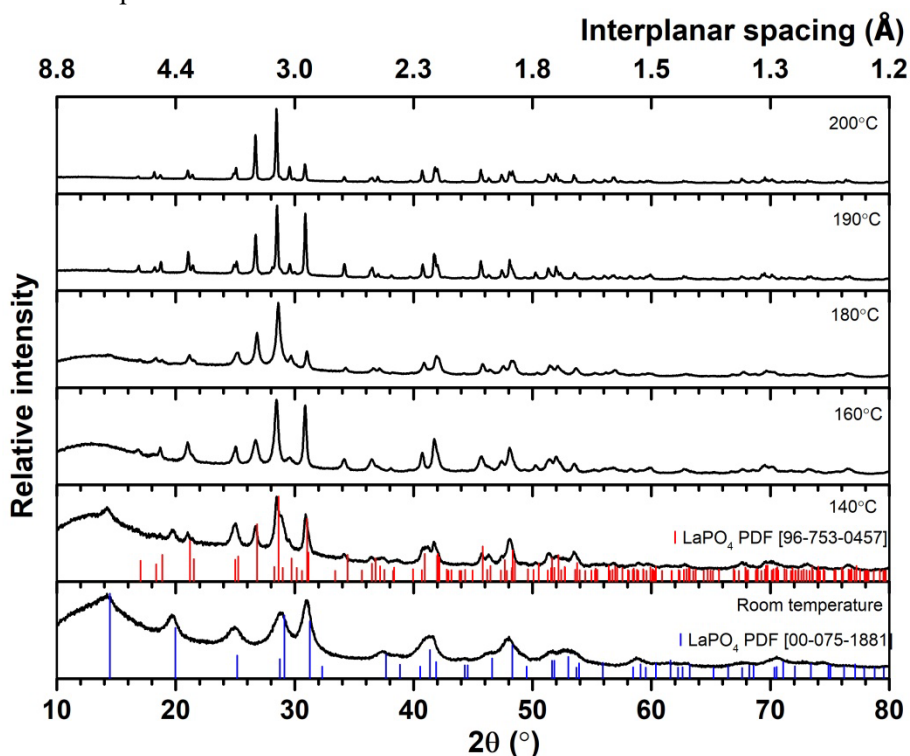


Fig. 26. XRD patterns of $\text{LaPO}_4:1\%\text{Eu}$ samples were synthesized using $\text{NH}_4\text{H}_2\text{PO}_4$ at different temperature.

SEM analysis of all synthesized $\text{LaPO}_4:1\%\text{Eu}$ samples was also performed to evaluate the morphology of the formed particles shown in Figure 27 A and 27 B. In both cases, the particles obtained by $\text{LaPO}_4:1\%\text{Eu}$ synthesized at room temperature are of irregular indefinite shape and

unequal size, similar to spherical particles. By increasing the synthesis temperature, the shape of the particle becomes similar to nanorods. For synthesis using $(\text{NH}_4)_2\text{HPO}_4$ as a precursor for PO_4^{3-} , the shape and size of the particles are more uniform compared to the particles synthesized at the same temperature when $\text{NH}_4\text{H}_2\text{PO}_4$ is used. The particle size measurements of the synthesized samples are presented in Tables 4 and 5. At synthesis temperatures above $160\text{ }^\circ\text{C}$, when the particles become similar to nanorods, the particle is longer when ammonium dihydrogen phosphate is used for synthesis. At the synthesis temperature of $200\text{ }^\circ\text{C}$, the average of the particle's length is 2652 nm and width is 609 nm , which is more than twice as large as using diammonium phosphate.

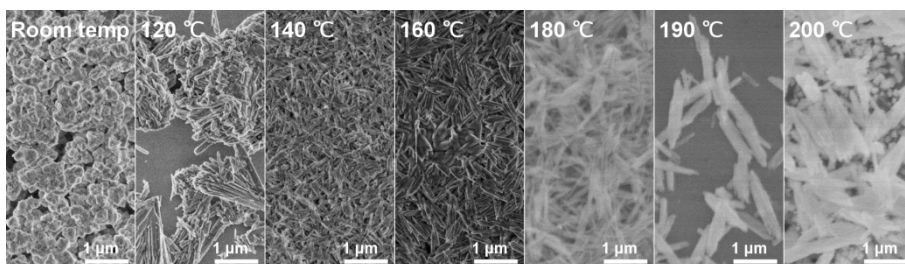


Fig. 27 A. SEM images of $\text{LaPO}_4:1\%\text{Eu}$ samples were synthesized using $(\text{NH}_4)_2\text{HPO}_4$ at different temperature.

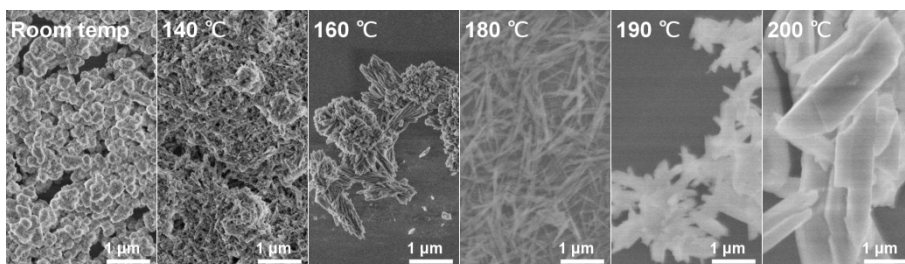


Fig. 27 B. SEM images of $\text{LaPO}_4:1\%\text{Eu}$ samples were synthesized using $\text{NH}_4\text{H}_2\text{PO}_4$ at different temperature.

Table 4 Measured particle size of LaPO₄:1%Eu samples were synthesized using (NH₄)₂HPO₄ at different temperature.

Sample	Length, nm	Standart deviation, nm	Width, nm	Standart deviation, nm	Length to width ratio
t = room temp.	740	202	385	62	1.9
t = 120 °C	1508	1005	88	33	17.1
t = 140 °C	286	83	36	7	7.9
t = 160 °C	486	89	77	20	6.3
t = 180 °C	737	921	76	20	9.7
t = 190 °C	1162	223	179	48	6.5
t = 200 °C	1227	143	224	92	5.5

Table 5 Measured particle size of LaPO₄:1%Eu samples were synthesized using NH₄H₂PO₄ at different temperature.

Sample	Length, nm	Standart deviation, nm	Width, nm	Standart deviation, nm	Length to width ratio
t = room temp.	525	99	319	27	1.6
t = 140 °C	271	57	65	15	4.2
t = 160 °C	826	253	205	86	4.0
t = 180 °C	800	379	59	29	13.6
t = 190 °C	1324	235	210	59	6.3
t = 200 °C	2652	728	609	218	4.4

Based on these synthesis and analysis results, it was decided to choose diammonium hydrogen phosphate (NH₄)₂HPO₄ as a precursor of PO₄³⁻ ions for further synthesis and to perform hydrothermal synthesis at 180 °C in order to synthesize the monoclinic crystal structure particals. A series of La_xGd_{1-x}PO₄:1%Eu synthesis was performed where x = 1; 0,75; 0,5; 0,25, 0. The results of XRD analysis are presented in Figure 28. From the diffractogram we can see that the crystal structure of the material obtained at x=0,5; 0,25, 0 is hexagonal because it corresponds to reference data of hexagonal Gadolinium Phosphate Hydrate (PDF ICDD 00-039-0232). However, the diffractograms of La_{0.75}Gd_{0.24}PO₄:1%Eu and LaPO₄:1%Eu

correspond to reference data of monoclinic Lanthanum Phosphate (PDF ICDD 96-153-0457).

A faint increase of the intensity of the the background line at a range from 10° to 20° is present if $x = 0.50$ and 0.25 indicating the amorphousness of the synthesized material itself or the influence of the amorphous glass tray on which the research material was place. Since the annealing temperature of all samples is constant, it is difficult to conclude the phase elementary composition or samplpe preparation gives this affect.

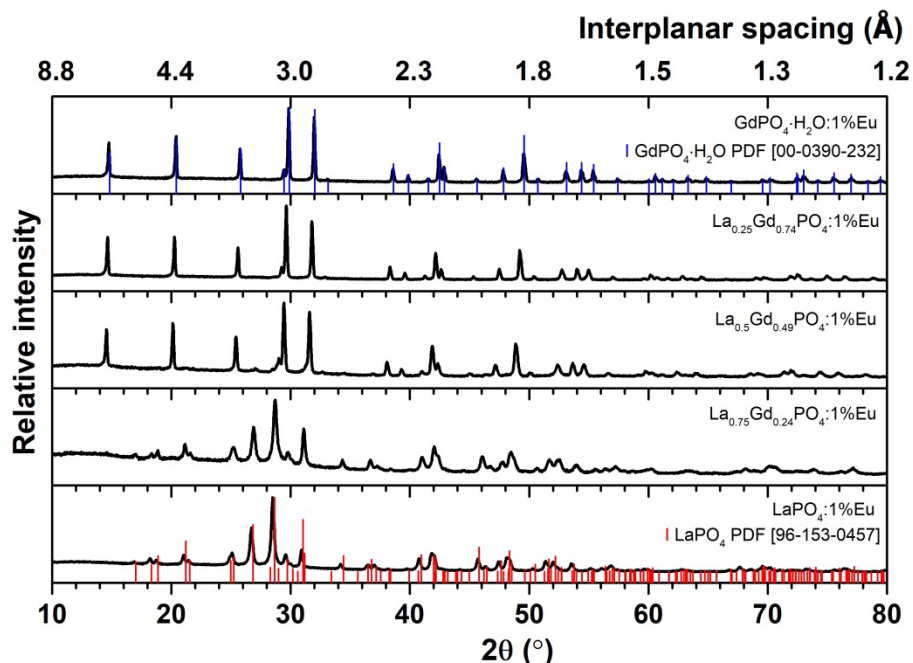


Fig. 28. XRD of $\text{La}_x\text{Gd}_{1-x}\text{PO}_4:1\% \text{Eu}$ containing different content of lanthanum

The materials obtained during these syntheses were also examined by SEM. The obtained SEM images of $\text{La}_x\text{Gd}_{1-x}\text{PO}_4:1\% \text{Eu}$ reflect the morphology of the particles when the synthesis temperature is 180°C . As can be seen, the shape and size of the synthesized particles change depending on the composition of the products. The structure of sintered $\text{LaPO}_4:1\% \text{Eu}$ (Figure 29 A) particles have similar shape, which could be called nanorods, the average particle length is 727 nm and the average width is 80 nm . The shape of the particles of $\text{La}_{0.75}\text{Gd}_{0.24}\text{PO}_4:1\% \text{Eu}$ (Figure 29 B) can be called a precursor of nanorods, but these particles are much shorter than the previously mentioned pure lanthanum phosphate particles, and the

average particle length is 216 nm and the average width is 58 nm. When gadolinium is present in the synthesized phosphate as much or more than lanthanum, it can be seen that the particles lose their nanorods shape and become irregular, unevenly sized, cohesive polygons, which can no longer be called nanoparticles, but microstructures with a size of up to 5 μm are obtained, as can be seen in Figure 29 D where the average particle length is 2.7 μm and 28E – 1.6 μm .

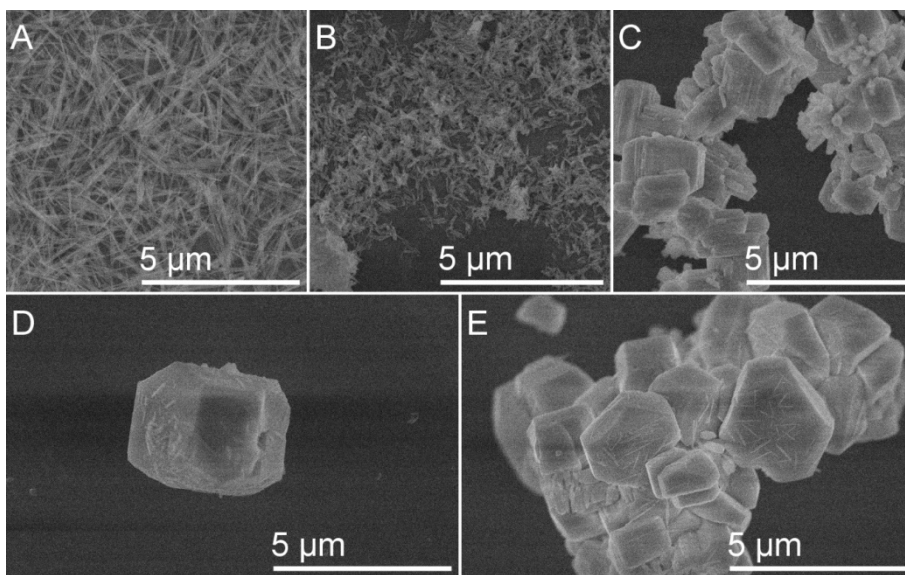


Fig. 29. SEM images of $\text{La}_x\text{Gd}_{1-x}\text{PO}_4:1\%$ $x = 1$ (A); 0.75 (B); 0.5 (C); 0.25 (D); 0 (E).

The investigation in chapter 3.1. has shown that GdPO_4 exhibits the best luminescence properties if the sample is doped by 15% of Eu^{3+} . Therefore, after evaluating the previously described synthesis and analysis results, when $\text{La}_{0.75}\text{Gd}_{0.24}\text{PO}_4:1\%\text{Eu}$ single phase with a monoclinic crystal structure is obtained, it was decided to increase from 1% of Eu^{3+} to 15% percent by replacing La or Gd. An XRD study was performed to evaluate the sample's crystal structure phase composition and purity. XRD analysis of both samples have shown that a uniform phase composition was obtained and is shown on Figure 30. The XRD patterns of samples correspond to reference data of monoclinic Lanthanum Phosphate (PDF ICDD 96-153-0457). Based on this database, it has been obtained a pure monoclinic phase.

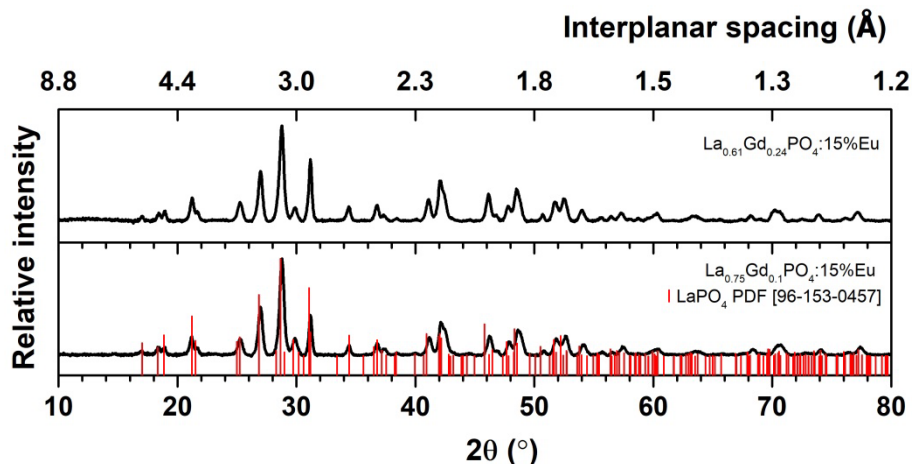


Fig. 30. XRD of $\text{La}_{0.61}\text{Gd}_{0.24}\text{PO}_4:15\%\text{Eu}$ and $\text{La}_{0.75}\text{Gd}_{0.1}\text{PO}_4:15\%\text{Eu}$

SEM analysis was conducted to investigate morphology and particle size of the materials obtained by hydrothermal syntheses. Nanoparticles in the shape of nanorods were synthesized in both samples. However, the particles' lengths and thicknesses were not uniform in either sample, with some particles adhering to one another (Figure 31). In the $\text{La}_{0.75}\text{Gd}_{0.1}\text{PO}_4:15\%\text{Eu}$ sample (A), the particles formed were slightly shorter and thicker compared to the $\text{La}_{0.61}\text{Gd}_{0.24}\text{PO}_4:15\%\text{Eu}$ sample (B). $\text{La}_{0.75}\text{Gd}_{0.1}\text{PO}_4:15\%\text{Eu}$ particles range in length varies from 45 nm to 150 nm. There are a very few smaller size particles. The particle thickness ranges from 13 nm to 35 nm without measuring agglomerated particles. The synthesized particles of sample B have a measured length in the range of 120 nm to 250 nm and a thickness from 10 nm to 40 nm. From these measurements, we can see that the particles formed in sample A are slightly shorter compared to the particles in sample B, but slightly thicker.

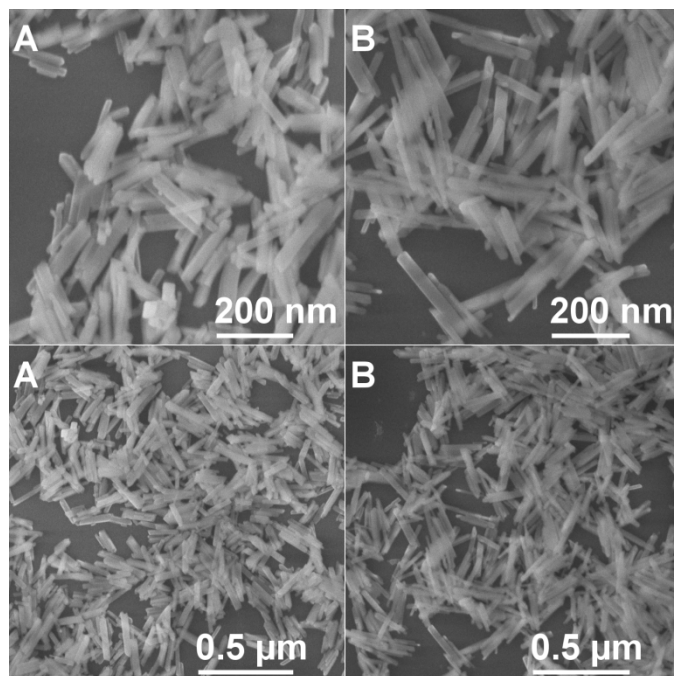


Fig. 31. SEM images of $\text{La}_{0.61}\text{Gd}_{0.24}\text{PO}_4:15\%\text{Eu}$ and $\text{La}_{0.75}\text{Gd}_{0.1}\text{PO}_4:15\%\text{Eu}$.

The luminescent characteristics of $\text{La}_{0.61}\text{Gd}_{0.24}\text{PO}_4:15\%\text{Eu}$ and $\text{La}_{0.75}\text{Gd}_{0.1}\text{PO}_4:15\%\text{Eu}$ samples were examined and shown in Figure. 32 and 33. As the samples appeared pure white, they were expected to exhibit minimal or no absorption within the visible spectrum. The excitation spectra were recorded from 250 nm to 585 nm, with an emission wavelength of $\lambda_{\text{em}} = 591$ nm. The excitation spectra demonstrated a broadband at higher energy (ranging from 250 nm to 270 nm) attributable to charge transfer, resulting from electron transfer from O^{2-} to Eu^{3+} . The ${}^8\text{S}_{7/2} \rightarrow {}^6\text{P}_J$ transitions of the Gd^{3+} ion was assigned to the narrow peaks at ~ 298 nm. The presence of these Gd^{3+} excitation lines in the excitation spectra monitored for Eu^{3+} ion indicated $\text{Gd}^{3+} \rightarrow \text{Eu}^{3+}$ energy transfer. The remaining excitation peaks were attributed to the Eu^{3+} ion. The peaks at ~ 318 nm was associated with the ${}^7\text{F}_0 \rightarrow {}^5\text{H}_J$ transitions, while a cluster of several peaks was visible in the range of 370 nm to 390 nm, ascribed to the ${}^7\text{F}_0 \rightarrow {}^5\text{D}_4$ and ${}^7\text{F}_0 \rightarrow {}^5\text{G}_J$, ${}^7\text{F}_0 \rightarrow {}^5\text{G}_J$; ${}^5\text{L}_7$ transitions. The most intense peak at 393 nm was related to the transition ${}^7\text{F}_0 \rightarrow {}^5\text{L}_6$. The small peaks at ~ 415 nm, ~ 463 nm, and ~ 527 nm was assigned to the transitions of ${}^7\text{F}_0 \rightarrow {}^5\text{D}_3$, ${}^7\text{F}_0 \rightarrow {}^5\text{D}_2$, and ${}^7\text{F}_0 \rightarrow {}^5\text{D}_1$, respectively.

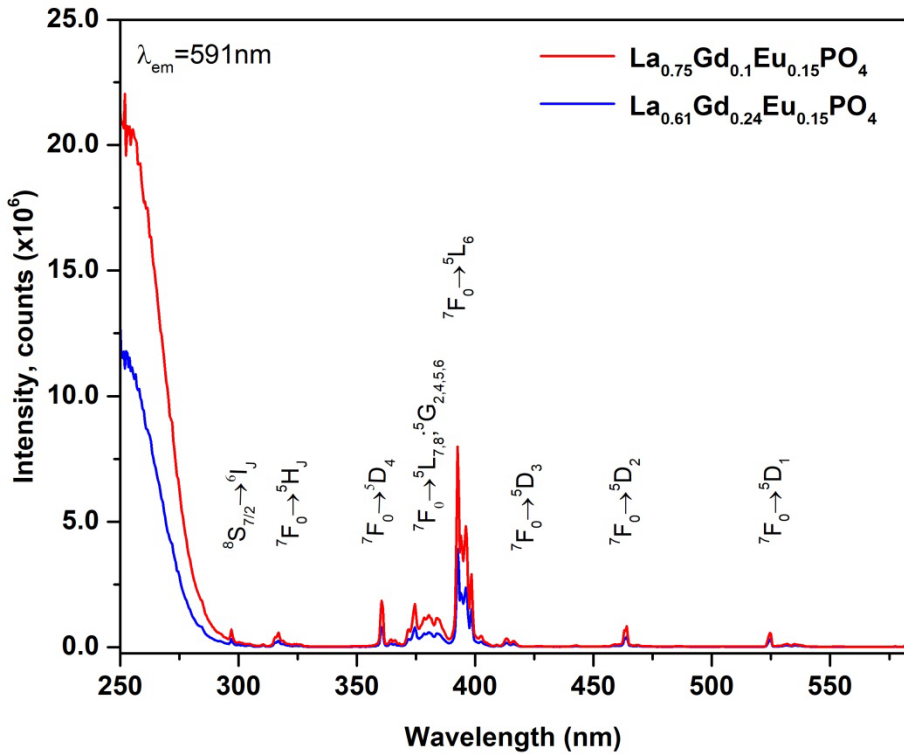


Fig. 32. Excitation spectra of $\text{La}_{0.61}\text{Gd}_{0.24}\text{PO}_4:15\%\text{Eu}$ and $\text{La}_{0.75}\text{Gd}_{0.1}\text{PO}_4:15\%\text{Eu}$.

The luminescence properties of $\text{La}_{0.61}\text{Gd}_{0.24}\text{PO}_4:15\%\text{Eu}$ and $\text{La}_{0.75}\text{Gd}_{0.1}\text{PO}_4:15\%\text{Eu}$ samples were investigated by exciting them with a wavelength of 393 nm and measuring their emission spectra (Figure 33). The emitted radiation was found to be in the orange-red colour range, and the emission peaks were attributed to various transitions between different energy levels of the Eu^{3+} ion. The emission spectral peaks at ~577 nm, ~590 nm, ~615 nm, ~650 nm and ~690 nm attributed to ${}^5\text{D}_0 \rightarrow {}^7\text{F}_0$, ${}^5\text{D}_0 \rightarrow {}^7\text{F}_1$, ${}^5\text{D}_0 \rightarrow {}^7\text{F}_2$, ${}^5\text{D}_0 \rightarrow {}^7\text{F}_3$, and ${}^5\text{D}_0 \rightarrow {}^7\text{F}_4$ transitions, respectively. The peak at 577 nm was the smallest, it indicated the emission as a dipolar electric transition for local C_s , C_n or C_{nv} sites. The peak with the highest intensity was observed at 690 nm, which is typical for Eu^{3+} doped orthophosphates [145]. As expected, and aimed for, the emission intensity of $\text{La}_{0.75}\text{Gd}_{0.1}\text{PO}_4:15\%\text{Eu}$ is significantly higher and reaches 5.5×10^5 counts compared to the previously synthesized and discussed samples with a hexagonal crystal system, where the maximum of emission intensity is 2.5×10^5 counts.

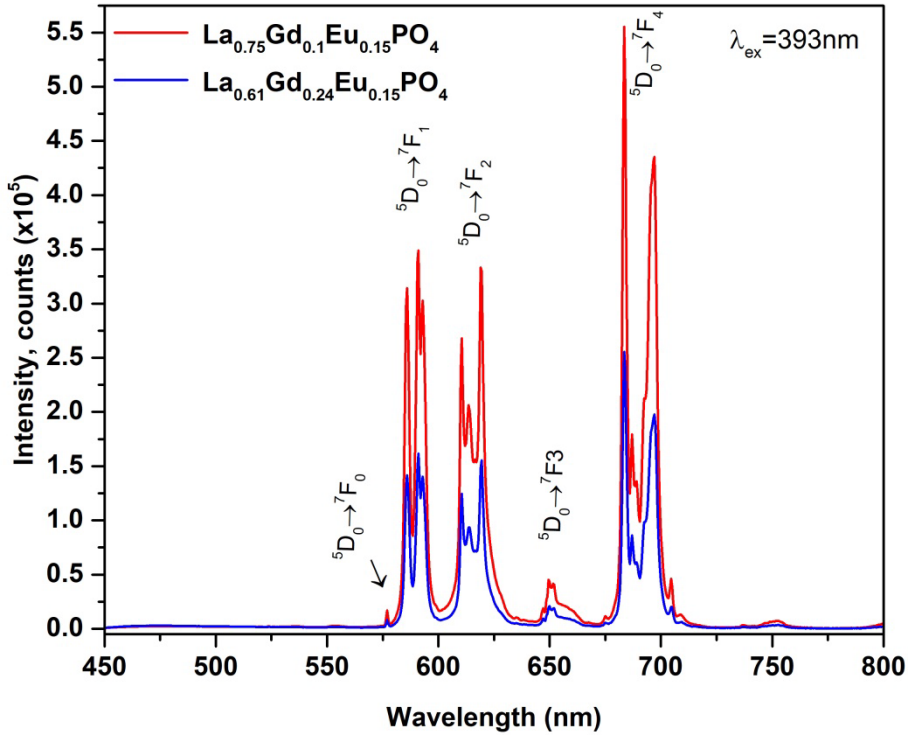


Fig. 33. Emission spectra of $\text{La}_{0.61}\text{Gd}_{0.24}\text{PO}_4:15\%\text{Eu}$ and $\text{La}_{0.75}\text{Gd}_{0.1}\text{PO}_4:15\%\text{Eu}$.

Magnetization dependence on applied magnetic field strength is shown in Figure 34. For paramagnets the magnetization is proportional to applied magnetic field strength $M = \chi H$ where volume magnetic susceptibility χ according to Curie-Weiss law is

$$\chi = \frac{N}{3k_B} \cdot \frac{\mu_{eff}^2}{T + \Theta} \quad (\text{Eq.1.})$$

N is number of paramagnetic atoms per volume, k_B is the Boltzmann constant, and Θ is Weiss constant. The effective magnetic moment of paramagnetic atom where J is the angular momentum quantum number and μ_B is the Bohr magneton. Though for the main state of Eu^{3+} $J = 0$, the first excited state is close to it at room temperature, so Eu^{3+} also contributes to the paramagnetism of the samples. However, the effective magnetic moment is larger for Gd^{3+} ion with $J = 7/2$ and g -factor $g = 2$. Although magnetic susceptibility also depends on the Weiss constant and some deviations from Curie-Weiss law are possible, since the GdPO_4 magnetic ordering temperature $T_N = 225$ K [2] is quite close to room temperature, the

susceptibility differences for samples can mainly be explained by different amounts of Gd^{3+} .

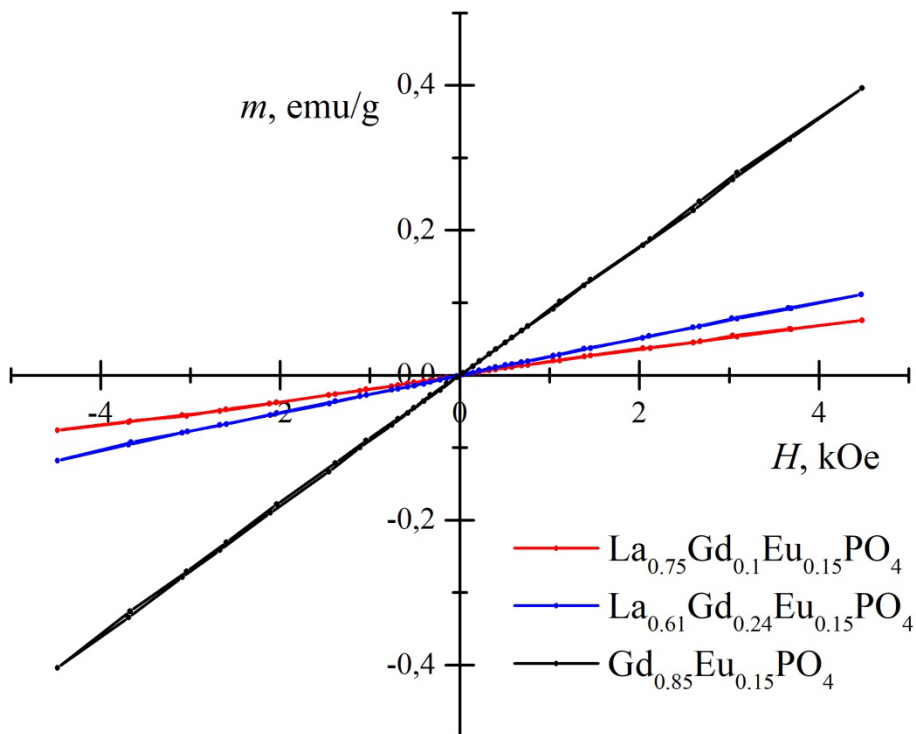


Fig. 34. Dependence of magnetization on magnetic field strength at room temperature.

All three investigated samples exhibited paramagnetic properties and can potentially be used as contrast in magnetic resonance imaging (MRI). However, based on the luminescence measurements of the samples, $La_{0.61}Gd_{0.24}PO_4:15\%Eu$ monoclinic nanorods have the highest emission intensity and can potentially be used for multimodal imaging combining magnetic resonance imaging (MRI) and luminescence measurements.

CONCLUSIONS

1. Due to a similar ionic radius, gadolinium is replaced by europium even up to 20% without significant effect on the hexagonal crystal structure. Furthermore, the Eu^{3+} concentration does not dramatically affect the particle size formed, but, contrary to what has been reported so far, the emission is most intense if the amount of Eu^{3+} is 15%. If the amount of europium is exceeded the concentration quenching begins.
2. The size of $\text{Gd}_{0.85}\text{Eu}_{0.15}\text{PO}_4 \cdot \text{H}_2\text{O}$ nanoparticles can be adjusted by changing the filling of the hydrothermal reactor with different amounts of solvent (water). The obtained particles were characterized by a rod-like morphology, and their size was effectively controlled.
3. The size and the ratio of length and width affect the luminescence properties of nanorods. In this way, the desired luminescent properties can be adjusted by selecting the filling of the reactor volume. The intensity of $\text{Gd}_{0.85}\text{Eu}_{0.15}\text{PO}_4 \cdot \text{H}_2\text{O}$ samples emission increases if more Eu is in the bulk of nanorods. Under our investigation, the optimal size and ratio of width and length particles were obtained for the sample synthesized at volume $V = 40$ mL.
4. The choice of the precursor of PO_4^{3-} ions significantly influenced $\text{LaPO}_4:1\%\text{Eu}$ crystal structure. $(\text{NH}_4)_2\text{HPO}_4$ precursor led to distinct crystal structures at lower temperatures compared to $\text{NH}_4\text{H}_2\text{PO}_4$.
5. A higher amount of lanthanum in the $\text{La}_x\text{Gd}_{1-x}\text{PO}_4:1\%\text{Eu}$ compound leads to the formation of a monoclinic phase.
6. Increasing Eu^{3+} content to 15% in $\text{La}_{0.61}\text{Gd}_{0.24}\text{PO}_4:15\%\text{Eu}$ and $\text{La}_{0.75}\text{Gd}_{0.1}\text{PO}_4:15\%\text{Eu}$ samples exhibited enhanced luminescence emission. Emission spectra demonstrated distinct peaks corresponding to Eu^{3+} transitions, with superior emission intensity observed in $\text{La}_{0.75}\text{Gd}_{0.1}\text{PO}_4:15\%\text{Eu}$ samples compared to hexagonal counterparts.
7. Magnetization studies indicated paramagnetic behavior in synthesized samples, influenced by both Eu^{3+} and Gd^{3+} ions.
8. $\text{La}_{0.61}\text{Gd}_{0.24}\text{PO}_4:15\%\text{Eu}$ monoclinic nanorods are paramagnetic and have the highest luminescence emission intensity and can potentially be used for multimodal imaging by combining magnetic resonance imaging (MRI) and luminescence measurements.

REFERENCES

- [1] Y. Huang, P.O. Boamah, J. Gong, Q. Zhang, M. Hua, Y. Ye, Gd (III) complex conjugate of low-molecular-weight chitosan as a contrast agent for magnetic resonance/fluorescence dual-modal imaging, *Carbohydr. Polym.* 143 (2016) 288–295. <https://doi.org/10.1016/j.carbpol.2016.02.032>.
- [2] T. Jahanbin, H. Sauriat-Dorizon, P. Spearman, S. Benderbous, H. Korri-Youssoufi, Development of Gd(III) porphyrin-conjugated chitosan nanoparticles as contrast agents for magnetic resonance imaging, *Mater. Sci. Eng. C.* 52 (2015) 325–332. <https://doi.org/10.1016/j.msec.2015.03.007>.
- [3] T.S. Atabaev, Y.C. Shin, S.J. Song, D.W. Han, N.H. Hong, Toxicity and t2-weighted magnetic resonance imaging potentials of holmium oxide nanoparticles, *Nanomaterials.* 7 (2017). <https://doi.org/10.3390/nano7080216>.
- [4] R.B. Northrop, Noninvasive instrumentation and measurement in medical diagnosis, *Noninvasive Instrum. Meas. Med. Diagnosis.* 2565 (2001) 1–546. <https://doi.org/10.1118/1.1600741>.
- [5] H. Hifumi, S. Yamaoka, A. Tanimoto, D. Citterio, K. Suzuki, Gadolinium-based hybrid nanoparticles as a positive MR contrast agent, *J. Am. Chem. Soc.* 128 (2006) 15090–15091. <https://doi.org/10.1021/ja066442d>.
- [6] S. Golovynskyi, I. Golovynska, L.I. Stepanova, O.I. Datsenko, L. Liu, J. Qu, T.Y. Ohulchanskyi, Optical windows for head tissues in near-infrared and short-wave infrared regions: Approaching transcranial light applications, *J. Biophotonics.* 11 (2018). <https://doi.org/10.1002/jbio.201800141>.
- [7] W. Ren, G. Tian, L. Zhou, W. Yin, L. Yan, S. Jin, Y. Zu, S. Li, Z. Gu, Y. Zhao, Lanthanide ion-doped GdPO₄ nanorods with dual-modal bio-optical and magnetic resonance imaging properties, *Nanoscale.* 4 (2012) 3754–3760. <https://doi.org/10.1039/c2nr30683b>.
- [8] Z. Xu, Y. Cao, C. Li, P. Ma, X. Zhai, S. Huang, X. Kang, M. Shang, D. Yang, Y. Dai, J. Lin, Urchin-like GdPO₄ and GdPO₄:Eu³⁺ hollow spheres – hydrothermal synthesis, luminescence and drug-delivery properties, *J. Mater. Chem.* 21 (2011) 3686. <https://doi.org/10.1039/c0jm03333b>.
- [9] K. Igashira, D. Nakauchi, T. Ogawa, T. Kato, N. Kawaguchi, T. Yanagida, Effects of dopant concentration in Eu-doped Ca₂MgSi₂O₇ single crystalline scintillators, *Mater. Res. Bull.* 135 (2021) 111155. <https://doi.org/10.1016/j.materresbull.2020.111155>.
- [10] M. Yang, Y. Wu, J. Shi, H. Li, X. Zhao, G. Ren, Effects of different Eu concentrations and Cu, Mg or Ba ions co-doping on optical and scintillation properties of LiCaAlF₆:Eu single crystals, *Radiat. Meas.* 147 (2021) 1350–4487.

- <https://doi.org/10.1016/J.RADMEAS.2021.106638>.
- [11] N. Yaiphaba, R.S. Ningthoujam, N. Shanta Singh, R.K. Vatsa, N. Rajmuhon Singh, Probing of inversion symmetry site in Eu^{3+} -doped GdPO_4 by luminescence study: Concentration and annealing effect, *J. Lumin.* 130 (2010) 174–180. <https://doi.org/10.1016/j.jlumin.2009.08.008>.
- [12] M.E. Alvarez-Ramos, J. Alvarado-Rivera, F. Félix-Domínguez, R.C. Carrillo-Torres, R. Sánchez-Zeferino, G. Saavedra-Rodríguez, Multicolor green to orange-red emission of Tb^{3+} and Eu^{3+} -codoped tellurite glasses: Eu^{3+} concentration and $\text{Tb}^{3+} \rightarrow \text{Eu}^{3+}$ energy transfer, *Appl. Phys. A* 129 (2023) 75. <https://doi.org/10.1007/s00339-022-06347-6>.
- [13] D. Chen, Y. Yu, P. Huang, H. Lin, Z. Shan, Y. Wang, Color-tunable luminescence of Eu^{3+} in LaF_3 embedded nanocomposite for light emitting diode, *Acta Mater.* 58 (2010) 3035–3041. <https://doi.org/10.1016/j.actamat.2010.01.035>.
- [14] H. Lin, S. Tanabe, L. Lin, D.L. Yang, K. Liu, W.H. Wong, J.Y. Yu, E.Y.B. Pun, Infrequent blue and green emission transitions from Eu^{3+} in heavy metal tellurite glasses with low phonon energy, *Phys. Lett. Sect. A Gen. At. Solid State Phys.* 358 (2006) 474–477. <https://doi.org/10.1016/j.physleta.2006.05.066>.
- [15] M. Dejneka, E. Snitzer, R.E. Riman, Blue, green and red fluorescence and energy transfer of Eu^{3+} in fluoride glasses, *J. Lumin.* 65 (1995) 227–245. [https://doi.org/10.1016/0022-2313\(95\)00073-9](https://doi.org/10.1016/0022-2313(95)00073-9).
- [16] J. Adam, W. Metzger, M. Koch, P. Rogin, T. Coenen, J. Atchison, P. König, Light Emission Intensities of Luminescent $\text{Y}_2\text{O}_3:\text{Eu}$ and $\text{Gd}_2\text{O}_3:\text{Eu}$ Particles of Various Sizes, *Nanomaterials*. 7 (2017) 26. <https://doi.org/10.3390/nano7020026>.
- [17] V.M. Lisitsyn, D.T. Valiev, I.A. Tupitsyna, E.F. Polisadova, V.I. Oleshko, L.A. Lisitsyna, L.A. Andryuschenko, A.G. Yakubovskaya, O.M. Vovk, Effect of particle size and morphology on the properties of luminescence in ZnWO_4 , *J. Lumin.* 153 (2014) 130–135. <https://doi.org/10.1016/j.jlumin.2014.03.024>.
- [18] G.L. Varaprasad, H. Lee, S. Kim, E. Kim, E. Pavitra, N. Valluru, Y.-K. Han, G.S.R. Raju, Y.S. Huh, Phosphate source induced rapid synthesis of urchin-like hydrated $\text{GdPO}_4:\text{Eu}^{3+}$ nanoparticles: Imaging and drug delivery in A549 cell line, *Ceram. Int.* (2022). <https://doi.org/10.1016/j.ceramint.2022.05.086>.
- [19] M.A. Hassairi, A. Garrido Hernández, T. Kallel, M. Dammak, D. Zambon, G. Chadeyron, A. Potdevin, D. Boyer, R. Mahiou, Spectroscopic properties and Judd-Ofelt analysis of Eu^{3+} doped GdPO_4 nanoparticles and nanowires, *J. Lumin.* 170 (2016) 200–206. <https://doi.org/10.1016/j.jlumin.2015.10.054>.
- [20] N.K. Sahu, R.S. Ningthoujam, D. Bahadur, Disappearance and recovery of luminescence in $\text{GdPO}_4:\text{Eu}^{3+}$ nanorods: Propose to

- water/OH⁻ release under near infrared and gamma irradiations, *J. Appl. Phys.* 112 (2012) 836. <https://doi.org/10.1063/1.4731644>.
- [21] R. Priya, R. Mariappan, A. Karthikeyan, E. Palani, E. Krishnamoorthy, G. Gowrisankar, Review on rare earth metals doped LaPO₄ for optoelectronic applications, *Solid State Commun.* 339 (2021) 114457. <https://doi.org/10.1016/j.ssc.2021.114457>.
- [22] M.T. Colomer, L. Zur, M. Ferrari, A.L. Ortiz, Structural-microstructural characterization and optical properties of Eu³⁺, Tb³⁺-codoped LaPO₄·nH₂O and LaPO₄ nanorods hydrothermally synthesized with microwaves, *Ceram. Int.* 44 (2018) 11993–12001. <https://doi.org/10.1016/j.ceramint.2018.03.142>.
- [23] N. Clavier, R. Podor, N. Dacheux, Crystal chemistry of the monazite structure, *J. Eur. Ceram. Soc.* 31 (2011) 941–976. <https://doi.org/10.1016/j.jeurceramsoc.2010.12.019>.
- [24] Huheey J.E., Keiter E.A., Keiter R.L., *Inorganic Chemistry Principles of Structure and Reactivity*, ed. 4, USA, Harper Collins College Publishers, 1993.
- [25] Ladd M., *Symmetry and Group Theory in Chemistry*, England, Horwood Publishing, 1998.
- [26] S.N. Achary, S. Bevara, A.K. Tyagi, Recent progress on synthesis and structural aspects of rare-earth phosphates, *Coord. Chem. Rev.* 340 (2017) 266–297. <https://doi.org/10.1016/j.ccr.2017.03.006>.
- [27] D. Qin, A. Mesbah, C. Gausse, S. Szenknect, N. Dacheux, N. Clavier, Incorporation of thorium in the rhabdophane structure: Synthesis and characterization of Pr_{1-2x}Ca_xTh_xPO₄·nH₂O solid solutions, *J. Nucl. Mater.* 492 (2017) 88–96. <https://doi.org/10.1016/j.jnucmat.2017.05.019>.
- [28] Y. Ni, J.M. Hughes, A.N. Mariano, Crystal chemistry of the monazite and xenotime structures, *Am. Mineral.* 80 (1995) 21–26. <https://doi.org/10.2138/am-1995-1-203>.
- [29] H.J. Förster, The chemical composition of REE-Y-Th-U-rich accessory minerals in peraluminous granites of the Erzgebirge-Fichtelgebirge region, Germany. Part II: Xenotime, *Am. Mineral.* 83 (1998) 1302–1315. <https://doi.org/10.2138/AM-1998-11-1219>.
- [30] A. Mesbah, N. Clavier, E. Elkaim, C. Gausse, I. Ben Kacem, S. Szenknect, N. Dacheux, Monoclinic Form of the Rhabdophane Compounds: REEPO₄·0.667H₂O, *Cryst. Growth Des.* 14 (2014) 5090–5098. <https://doi.org/10.1021/cg500707b>.
- [31] A. Berger, E. Gnos, E. Janots, A. Fernandez, J. Giese, Formation and composition of rhabdophane, bastnäsite and hydrated thorium minerals during alteration: Implications for geochronology and low-temperature processes, *Chem. Geol.* 254 (2008) 238–248. <https://doi.org/10.1016/J.CHEMGEO.2008.03.006>.
- [32] B.P. Onac, K. Ettinger, J. Kearns, I.I. Balasz, A modern, guano-related occurrence of foggite, CaAl(PO₄)(OH)₂·H₂O and churchite-

- (Y), $\text{YPO}_4 \cdot 2\text{H}_2\text{O}$ in Cioclovina Cave, Romania, *Mineral. Petrol.* 85 (2005) 291–302. <https://doi.org/10.1007/s00710-005-0106-4>.
- [33] G. Jia, K. Liu, Y. Zheng, Y. Song, M. Yang, H. You, Highly uniform $\text{Gd}(\text{OH})_3$ and $\text{Gd}_2\text{O}_3:\text{Eu}^{3+}$ nanotubes: Facile synthesis and luminescence properties, *J. Phys. Chem. C.* 113 (2009) 6050–6055. <https://doi.org/10.1021/jp9002164>.
- [34] S. Ullah, Y. Feng, M. Zhu, H. Kong, S. Sun, C. Dou, F. Zheng, J. Tang, D. Zhong, B. Teng, Co-precipitation synthesis and photoluminescence properties of $(\text{Gd}_x\text{La}_{1-x})\text{PO}_4:5\text{at.}\% \text{Eu}^{3+}$ orange-red emitting phosphors, *J. Mater. Sci. Mater. Electron.* 30 (2019) 14703–14713. <https://doi.org/10.1007/s10854-019-01842-8>.
- [35] M.R. Neupane, G.A. Garrett, S. Rudin, J.W. Andzelm, Phase dependent structural and electronic properties of lanthanum orthophosphate (LaPO_4), *J. Phys. Condens. Matter.* 28 (2016). <https://doi.org/10.1088/0953-8984/28/20/205501>.
- [36] H. Lai, A. Bao, Y. Yang, Y. Tao, H. Yang, Selective synthesis and luminescence property of monazite-and hexagonal-type $\text{LaPO}_4:\text{Eu}$ nanocrystals, (2009). <https://doi.org/10.1039/b818877g>.
- [37] Y.P. Fang, A.W. Xu, R.Q. Song, H.X. Zhang, L.P. You, J.C. Yu, H.Q. Liu, Systematic Synthesis and Characterization of Single-Crystal Lanthanide Orthophosphate Nanowires, *J. Am. Chem. Soc.* 125 (2003) 16025–16034. <https://doi.org/10.1021/ja037280d>.
- [38] R.D. Shannon, C.T. Prewitt, Effective ionic radii in oxides and fluorides, *Acta Crystallogr. Sect. B Struct. Crystallogr. Cryst. Chem.* 25 (1969) 925–946. <https://doi.org/10.1107/s0567740869003220>.
- [39] R. Kijkowska, E. Cholewka, B. Duszak, X-ray diffraction and Ir-absorption characteristics of lanthanide orthophosphates obtained by crystallisation from phosphoric acid solution, *J. Mater. Sci.* 38 (2003) 223–228. <https://doi.org/10.1023/A:1021188810349>.
- [40] S. Gallini, J.R. Jurado, M.T. Colomer, Combustion synthesis of nanometric powders of LaPO_4 and Sr-substituted LaPO_4 , *Chem. Mater.* 17 (2005) 4154–4161. <https://doi.org/10.1021/cm047945q>.
- [41] S. Rodriguez-Liviano, A.I. Becerro, D. Alcántara, V. Grazú, J.M. De La Fuente, M. Ocaña, Synthesis and properties of multifunctional tetragonal $\text{Eu}:\text{GdPO}_4$ nanocubes for optical and magnetic resonance imaging applications, *Inorg. Chem.* 52 (2013) 647–654. <https://doi.org/10.1021/ic3016996>.
- [42] T. Subramani, M.R. Rafiuddin, A. Shelyug, S. Ushakov, A. Mesbah, N. Clavier, D. Qin, S. Szenknect, E. Elkaim, N. Dacheux, A. Navrotsky, Synthesis, Crystal Structure, and Enthalpies of Formation of Churchite-type $\text{REPO}_4 \cdot 2\text{H}_2\text{O}$ (RE = Gd to Lu) Materials, *Cryst. Growth Des.* 19 (2019) 4641–4649. <https://doi.org/10.1021/acs.cgd.9b00524>.
- [43] K.M. Heffernan, N.L. Ross, E.C. Spencer, L.A. Boatner, The structural response of gadolinium phosphate to pressure, *J. Solid*

- State Chem. 241 (2016) 180–186.
<https://doi.org/10.1016/j.jssc.2016.06.009>.
- [44] J. Cho, C.H. Kim, Solid-state phase transformation mechanism from hexagonal $\text{GdPO}_4 : \text{Eu}^{3+}$ nanorods to monoclinic nanoparticles, *RSC Adv.* 4 (2014) 31385–31392. <https://doi.org/10.1039/c4ra03229b>.
- [45] X. Wang, J. Wu, H. Jia, Z. Liu, C. Liu, Y. Qi, Z. Wang, PEG coated nano-phosphor $\text{GdPO}_4 \cdot \text{H}_2\text{O} : 12\% \text{Eu}^{3+}$ and its performance analysis, *J. Alloys Compd.* 905 (2022) 164223. <https://doi.org/10.1016/j.jallcom.2022.164223>.
- [46] J. Yang, X. Wang, L. Song, N. Luo, J. Dong, S. Gan, L. Zou, Tunable luminescence and energy transfer properties of $\text{GdPO}_4 : \text{Tb}^{3+}, \text{Eu}^{3+}$ nanocrystals for warm-white LEDs, *Opt. Mater. (Amst.)* 85 (2018) 71–78. <https://doi.org/10.1016/j.optmat.2018.08.043>.
- [47] N. Ben Amar, T. Kallel, T. Koubaa, M.A. Hassairi, M. Dammak, E. Cavalli, Synthesis, characterization and optical spectroscopy of $\text{GdPO}_4 : \text{Er}^{3+}$, *Luminescence.* 35 (2020) 1056–1067. <https://doi.org/10.1002/bio.3817>.
- [48] M.T. Abbas, S.A. Khan, J. Mao, N.Z. Khan, L. Qiu, J. Ahmed, X. Wei, Y. Chen, S.M. Alshehri, S. Agathopoulos, Optical thermometry based on the luminescence intensity ratio of Dy^{3+} -doped GdPO_4 phosphors, *J. Therm. Anal. Calorim.* 147 (2022) 11769–11775. <https://doi.org/10.1007/s10973-022-11415-3>.
- [49] Z. Fu, T. Sheng, Z. Wu, Y. Yu, T. Cui, A novel and tunable upconversion luminescent material $\text{GdPO}_4 : \text{Yb}^{3+}, \text{Ln}^{3+}$ ($\text{Ln} = \text{Er}, \text{Tm}, \text{Ho}$), *Mater. Res. Bull.* 56 (2014) 138–142. <https://doi.org/10.1016/j.materresbull.2014.04.067>.
- [50] Pushpendra, I. Suryawanshi, S. Srinidhi, S. Singh, R. Kalia, R.K. Kunchala, S.L. Mudavath, B.S. Naidu, Downshifting and upconversion dual mode emission from lanthanide doped GdPO_4 nanorods for unclonable anti-counterfeiting, *Mater. Today Commun.* 26 (2021) 102144. <https://doi.org/10.1016/j.mtcomm.2021.102144>.
- [51] J. Xue, L. Yang, Y. Jia, H. Wang, N. Zhang, X. Ren, H. Ma, Q. Wei, H. Ju, Electrochemiluminescence Double Quenching System Based on Novel Emitter $\text{GdPO}_4 : \text{Eu}$ with Low-Excited Positive Potential for Ultrasensitive Procalcitonin Detection, *ACS Sensors.* 4 (2019) 2825–2831. <https://doi.org/10.1021/acssensors.9b01552>.
- [52] H. Lai, X. Yang, H. Yang, Luminescent properties of $\text{GdPO}_4 : \text{Eu}$ nanorods, *J. Mater. Sci. Mater. Electron.* 23 (2012) 285–289. <https://doi.org/10.1007/s10854-011-0405-y>.
- [53] H. Lai, H. Yang, Synthesis and luminescence properties of GdPO_4 doped with europium ion nanocrystals, *Solid State Sci.* 13 (2011) 1654–1657. <https://doi.org/10.1016/j.solidstatesciences.2011.06.018>.
- [54] J. Cho, C.H. Kim, Solid-state phase transformation mechanism from hexagonal $\text{GdPO}_4 : \text{Eu}^{3+}$ nanorods to monoclinic nanoparticles, *RSC Adv.* 4 (2014) 31385. <https://doi.org/10.1039/C4RA03229B>.

- [55] D. Bokov, A. Turki Jalil, S. Chupradit, W. Suksatan, M. Javed Ansari, I.H. Shewael, G.H. Valiev, E. Kianfar, Nanomaterial by Sol-Gel Method: Synthesis and Application, *Adv. Mater. Sci. Eng.* 2021 (2021). <https://doi.org/10.1155/2021/5102014>.
- [56] G.J. Owens, R.K. Singh, F. Foroutan, M. Alqaysi, C.M. Han, C. Mahapatra, H.W. Kim, J.C. Knowles, Sol-gel based materials for biomedical applications, *Prog. Mater. Sci.* 77 (2016) 1–79. <https://doi.org/10.1016/j.pmatsci.2015.12.001>.
- [57] Y. Yang, J. Bi, X. Gao, K. Sun, L. Qiao, G. Liang, H. Wang, Facile synthesis of nanocrystalline high-entropy diboride powders by a simple sol-gel method and their performance in supercapacitor, *Ceram. Int.* 49 (2023) 19523–19527. <https://doi.org/10.1016/j.ceramint.2023.02.170>.
- [58] M.A. Ahmadzadeh, S.F. Chini, A. Sadeghi, Size and shape tailored sol-gel synthesis and characterization of lanthanum phosphate (LaPO₄) nanoparticles, *Mater. Des.* 181 (2019) 108058. <https://doi.org/10.1016/j.matdes.2019.108058>.
- [59] R. Gao, D. Qian, W. Li, Sol-gel synthesis and photoluminescence of LaPO₄:Eu³⁺ nanorods, *Trans. Nonferrous Met. Soc. China (English Ed.)* 20 (2010) 432–436. [https://doi.org/10.1016/S1003-6326\(09\)60158-8](https://doi.org/10.1016/S1003-6326(09)60158-8).
- [60] M. Skruodiene, R. Juodvalkyte, G. Inkrataite, A. Pakalniskis, R. Ramanauskas, A. Sarakovskis, R. Skaudzius, Sol-gel assisted molten-salt synthesis of novel single phase Y_{3–2x}Ca_{2x}Ta_xAl_{5–x}O₁₂:1%Eu garnet structure phosphors, *J. Alloys Compd.* 890 (2022) 161889. <https://doi.org/10.1016/J.JALLCOM.2021.161889>.
- [61] M.J. Fisher, W. Wang, P.K. Dorhout, E.R. Fisher, Synthesis of LaPO₄:Eu nanostructures using the sol - gel template method, *J. Phys. Chem. C* 112 (2008) 1901–1907. <https://doi.org/10.1021/jp0763782>.
- [62] A.V. Rane, K. Kanny, V.K. Abitha, S. Thomas, Methods for Synthesis of Nanoparticles and Fabrication of Nanocomposites, in: *Synth. Inorg. Nanomater.*, Elsevier, 2018: pp. 121–139. <https://doi.org/10.1016/B978-0-08-101975-7.00005-1>.
- [63] M.Z. Iqbal, J. Khan, H.T.A. Awan, M. Alzaid, A.M. Afzal, S. Aftab, Cobalt–manganese-zinc ternary phosphate for high performance supercapattery devices, *Dalt. Trans.* 49 (2020) 16715–16727. <https://doi.org/10.1039/D0DT03313H>.
- [64] C. Yu, M. Yu, C. Li, X. Liu, J. Yang, P. Yang, J. Lin, Facile sonochemical synthesis and photoluminescent properties of lanthanide orthophosphate nanoparticles, *J. Solid State Chem.* 182 (2009) 339–347. <https://doi.org/10.1016/j.jssc.2008.10.023>.
- [65] Y. Wenyuan, L. Guanlai, Z. Li, Sonochemical synthesis and photoluminescence properties of rare-earth phosphate core/shell nanorods, *J. Rare Earths.* 28 (2010) 171–175. [https://doi.org/10.1016/S1002-0721\(09\)60074-0](https://doi.org/10.1016/S1002-0721(09)60074-0).

- [66] A. Phuruangrat, T. Thongtem, S. Thongtem, Sonochemical synthesis and characterization of uniform lanthanide orthophosphate (LnPO₄, Ln = La and Ce) nanorods, *Rare Met.* 34 (2015) 301–307. <https://doi.org/10.1007/s12598-014-0297-0>.
- [67] H. Dong, S.R. Du, X.Y. Zheng, G.M. Lyu, L.D. Sun, L.D. Li, P.Z. Zhang, C. Zhang, C.H. Yan, Lanthanide Nanoparticles: From Design toward Bioimaging and Therapy, *Chem. Rev.* 115 (2015) 10725–10815. <https://doi.org/10.1021/acs.chemrev.5b00091>.
- [68] L.A. Kolahalam, I. V. Kasi Viswanath, B.S. Diwakar, B. Govindh, V. Reddy, Y.L.N. Murthy, Review on nanomaterials: Synthesis and applications, *Mater. Today Proc.* 18 (2019) 2182–2190. <https://doi.org/10.1016/j.matpr.2019.07.371>.
- [69] R.A. Goncalves, R.P. Toledo, N. Joshi, O.M. Berengue, Green synthesis and applications of ZnO and TiO₂ nanostructures, *Molecules.* 26 (2021). <https://doi.org/10.3390/molecules26082236>.
- [70] S. Verma, K.K. Bamzai, Preparation by chemical co-precipitation, spectral and electrical characteristics of neodymium orthophosphate nanoparticles, *J. Rare Earths.* 33 (2015) 535–544. [https://doi.org/10.1016/S1002-0721\(14\)60453-1](https://doi.org/10.1016/S1002-0721(14)60453-1).
- [71] T.H. Lee, *Planar Microwave Engineering*, 2004. <https://doi.org/10.1017/cbo9780511812941>.
- [72] D. Stuerger, *Microwave-Materials Interactions and Dielectric Properties: From Molecules and Macromolecules to Solids and Colloidal Suspensions*, in: *Microwaves Org. Synth.* Third Ed., Wiley, 2013: pp. 1–56. <https://doi.org/10.1002/9783527651313.ch1>.
- [73] G. Cravotto, P. Cintas, *Microwave chemistry: History, development and legacy*, in: *Microw. Chem.*, 2017: pp. 1–17. <https://doi.org/10.1515/9783110479935-001>.
- [74] A. Abu-Samra, J.S. Morris, S.R. Koirtiyohann, Wet ashing of some biological samples in a microwave oven, *Anal. Chem.* 47 (1975) 1475–1477. <https://doi.org/10.1021/ac60358a013>.
- [75] J.A. Heseck, R.C. Wilson, Use of a Microwave Oven in In-Process Control, *Anal. Chem.* 46 (1974) 1160. <https://doi.org/10.1021/ac60344a017>.
- [76] C. Leonelli, S. Komarneni, Inorganic syntheses assisted by microwave heating, *Inorganics.* 3 (2015) 388–391. <https://doi.org/10.3390/inorganics3040388>.
- [77] C.N.R. Rao, H.S.S. Ramakrishna Matte, R. Voggu, A. Govindaraj, Recent progress in the synthesis of inorganic nanoparticles, *Dalt. Trans.* 41 (2012) 5089–5120. <https://doi.org/10.1039/c2dt12266a>.
- [78] L.-Y. Meng, B. Wang, M.-G. Ma, K.-L. Lin, The progress of microwave-assisted hydrothermal method in the synthesis of functional nanomaterials, *Mater. Today Chem.* 1–2 (2016) 63–83. <https://doi.org/10.1016/j.mtchem.2016.11.003>.
- [79] S. Promnopas, W. Promnopas, W. Maisang, S. Wannapop, T.

- Thongtem, S. Thongtem, O. Wiranwetchayan, One-step microwave-hydrothermal synthesis of visible-light-driven $\text{Ag}_3\text{PO}_4/\text{LaPO}_4$ photocatalyst induced by visible light irradiation, *Chem. Phys. Lett.* 779 (2021) 138883. <https://doi.org/10.1016/j.cplett.2021.138883>.
- [80] Z. Wang, Y. Tang, D. Fan, X. Liu, Y. Wang, J.G. Li, One-step microwave synthesis of $(\text{Gd}, \text{Eu})\text{PO}_4$ urchin-like hollow spheres: Enhanced luminescence and pH-sensitive drug delivery properties, *J. Alloys Compd.* 824 (2020) 153809. <https://doi.org/10.1016/j.jallcom.2020.153809>.
- [81] M.T. Colomer, J. Bartolomé, A.L. Ortiz, A. de Andrés, Raman characterization and photoluminescence properties of $\text{La}_{1-x}\text{Tb}_x\text{PO}_4 \cdot n\text{H}_2\text{O}$ and $\text{La}_{1-x}\text{Tb}_x\text{PO}_4$ phosphor nanorods prepared by microwave-assisted hydrothermal synthesis, *Ceram. Int.* 43 (2017) 10840–10847. <https://doi.org/10.1016/j.ceramint.2017.05.110>.
- [82] L. Ma, L.M. Xu, W.X. Chen, Z. De Xu, Microwave-assisted synthesis and characterization of $\text{LaPO}_4:\text{Re}$ ($\text{Re} = \text{Ce}^{3+}, \text{Eu}^{3+}, \text{Tb}^{3+}$) nanorods, *Mater. Lett.* 63 (2009) 1635–1637. <https://doi.org/10.1016/j.matlet.2009.04.038>.
- [83] G. Yang, S.J. Park, Conventional and microwave hydrothermal synthesis and application of functional materials: A review, *Materials (Basel)*. 12 (2019). <https://doi.org/10.3390/ma12071177>.
- [84] M. Janulevicius, V. Klimkevicius, A. Vanetsev, V. Plausinaitiene, S. Sakirzanovas, A. Katelnikovas, Controlled hydrothermal synthesis, morphological design and colloidal stability of $\text{GdPO}_4 \cdot n\text{H}_2\text{O}$ particles, *Mater. Today Commun.* 23 (2020) 100934. <https://doi.org/10.1016/J.MTCOMM.2020.100934>.
- [85] Z.G. Yan, Y.W. Zhang, L.P. You, R. Si, C.H. Yan, General synthesis and characterization of monocrystalline 1D-nanomaterials of hexagonal and orthorhombic lanthanide orthophosphate hydrate, *J. Cryst. Growth.* 262 (2004) 408–414. <https://doi.org/10.1016/J.JCRYSGRO.2003.10.058>.
- [86] E. Ezerskyte, A. Zarkov, V. Klimkevicius, A. Katelnikovas, Hydrothermal Synthesis of Well-Defined Red-Emitting Eu-Doped GdPO_4 Nanophosphors and Investigation of Their Morphology and Optical Properties, *Crystals*. 13 (2023). <https://doi.org/10.3390/cryst13020174>.
- [87] F. Wang, L. Li, C. Yang, Z. Cai, Z. Guo, S. Hou, X. Xie, Y. Chen, J. Huang, L. Zhang, Boosting luminescence and MRI evolution via regulation of $\text{GdPO}_4:5\%\text{Eu}^{3+}$ morphologies by H_3PO_4 , *Ceram. Int.* 49 (2023) 12725–12735. <https://doi.org/10.1016/j.ceramint.2022.12.137>.
- [88] G. Blasse, B.C. Grabmaier, *Luminescent Materials*, Springer Berlin Heidelberg, Berlin, Heidelberg, 1994. <https://doi.org/10.1007/978-3-642-79017-1>.
- [89] Lakowicz J.R., *Principles of Fluorescence Spectroscopy*, Springer US, Boston, MA, 1999. <https://doi.org/10.1007/978-1-4757-3061-6>.

- [90] G. Baryshnikov, B. Minaev, H. Ågren, Theory and Calculation of the Phosphorescence Phenomenon, *Chem. Rev.* 117 (2017) 6500–6537. <https://doi.org/10.1021/acs.chemrev.7b00060>.
- [91] M.A. Tzani, D.K. Giftofidou, M.G. Kallitsakis, N. V Pliatsios, N.P. Kalogiouri, P.A. Angaridis, I.N. Lykakis, M.A. Terzidis, Direct and Indirect Chemiluminescence: Reactions, Mechanisms and Challenges, *Molecules*. 26 (2021) 7664. <https://doi.org/10.3390/molecules26247664>.
- [92] Ronda C.R., ed., *Luminescence: From Theory to Applications*, Weinheim, WILEY-VCH Verlag GmbH & Co. KGaA, 2008.
- [93] C. Wei, D. Xu, J. Li, A. Geng, X. Li, J. Sun, Synthesis and luminescence properties of Eu³⁺-doped a novel double perovskite Sr₂YTaO₆ phosphor, *J. Mater. Sci. Mater. Electron.* 30 (2019) 2864–2871. <https://doi.org/10.1007/s10854-018-0563-2>.
- [94] T. Gavrilović, J. Periša, J. Papan, K. Vuković, K. Smits, D.J. Jovanović, M.D. Dramićanin, Particle size effects on the structure and emission of Eu³⁺:LaPO₄ and EuPO₄ phosphors, *J. Lumin.* 195 (2018) 420–429. <https://doi.org/10.1016/J.JLUMIN.2017.12.002>.
- [95] J. Zhou, L. Xie, J. Zhong, H. Liang, J. Zhang, M. Wu, Site occupancy and luminescence properties of Eu³⁺ in double salt silicate Na₃LuSi₃O₉, *Opt. Mater. Express.* 8 (2018) 736. <https://doi.org/10.1364/OME.8.000736>.
- [96] X. Liu, C. Lin, J. Lin, White light emission from Eu³⁺ in CaIn₂O₄ host lattices, *Appl. Phys. Lett.* 90 (2007) 3–6. <https://doi.org/10.1063/1.2539632>.
- [97] H. Zhang, Y. Wang, L. Han, Photoluminescence properties and energy transfer between Eu³⁺ and Nd³⁺ in polyborate BaGdB₉O₁₆:Eu³⁺, Nd³⁺, *J. Appl. Phys.* 109 (2011) 053109. <https://doi.org/10.1063/1.3553844>.
- [98] C. Li, C. Zhang, Z. Hou, L. Wang, Z. Quan, H. Lian, J. Lin, β-NaYF₄ and β-NaYF₄:Eu³⁺ Microstructures: Morphology Control and Tunable Luminescence Properties, *J. Phys. Chem. C*. 113 (2009) 2332–2339. <https://doi.org/10.1021/jp8101628>.
- [99] X. Duan, F. Yu, Y. Wu, Synthesis and luminescence properties of ZnGa₂O₄ spinel doped with Co²⁺ and Eu³⁺ ions, *Appl. Surf. Sci.* 261 (2012) 830–834. <https://doi.org/10.1016/j.apsusc.2012.08.112>.
- [100] S. V. Eliseeva, J.C.G. Bünzli, Lanthanide luminescence for functional materials and bio-sciences, *Chem. Soc. Rev.* 39 (2010) 189–227. <https://doi.org/10.1039/b905604c>.
- [101] L. Xie, X. Qu, B. Peng, Tb³⁺ ion luminescence monitors β-dicalcium silicate mineralization conversion, *Phys. B Condens. Matter.* 665 (2023) 415019. <https://doi.org/10.1016/j.physb.2023.415019>.
- [102] A. Bouddouch, E. Amaterz, A. Taoufyq, B. Bakiz, F. Guinneton, S. Villain, J.C. Valmalette, J.R. Gavarri, A. Benlhachemi, Photocatalytic and photoluminescent properties of a system based on

- SmPO₄ nanostructure phase, *Mater. Today Proc.* 27 (2020) 3139–3144. <https://doi.org/10.1016/j.matpr.2020.03.803>.
- [103] V. Singh, S. Kaur, A. Yadav, A.S. Rao, Blue emitting CaAl₄O₇:Tm³⁺ phosphor, *Optik (Stuttg)*. 265 (2022) 169509. <https://doi.org/10.1016/j.ijleo.2022.169509>.
- [104] R. Martín-Rodríguez, R. Geitenbeek, A. Meijerink, Incorporation and Luminescence of Yb³⁺ in CdSe Nanocrystals, *J. Am. Chem. Soc.* 135 (2013) 13668–13671. <https://doi.org/10.1021/ja4077414>.
- [105] V.R. Kumar, N. Purnachand, B.N. Kumar Reddy, V.R. Kumar, Y. Gandhi, B.V. Ragavaiah, NIR luminescence features of Nd³⁺ ion in lithium antimonite glass system, *Phys. B Condens. Matter.* 600 (2021) 412519. <https://doi.org/10.1016/j.physb.2020.412519>.
- [106] Z. Pan, A. Ueda, S.H. Morgan, R. Mu, Luminescence of Er³⁺ in Oxyfluoride Transparent Glass-Ceramics, *J. Rare Earths.* 24 (2006) 699–705. [https://doi.org/10.1016/S1002-0721\(07\)60012-X](https://doi.org/10.1016/S1002-0721(07)60012-X).
- [107] S.G. Revankar, K.A. Gedekar, P.D. Belsare, S.V. Moharil, Study of luminescence of Gd³⁺ in some aluminoborates and energy transfer from Gd³⁺ to Ln³⁺ (Ln = Eu, Tb or Dy), *Optik (Stuttg)*. 266 (2022) 169610. <https://doi.org/10.1016/j.ijleo.2022.169610>.
- [108] K. Binnemans, Lanthanide-based luminescent hybrid materials, *Chem. Rev.* 109 (2009) 4283–4374. <https://doi.org/10.1021/cr8003983>.
- [109] P. Dorenbos, 5d-level energies of Ce³⁺ and the crystalline environment. III. Oxides containing ionic complexes, *Phys. Rev. B - Condens. Matter Mater. Phys.* 64 (2001) 125117. <https://doi.org/10.1103/PhysRevB.64.125117>.
- [110] S. Han, R. Deng, X. Xie, X. Liu, Enhancing Luminescence in Lanthanide-Doped Upconversion Nanoparticles, *Angew. Chemie Int. Ed.* 53 (2014) 11702–11715. <https://doi.org/10.1002/anie.201403408>.
- [111] X.-Z. Wang, Synthesis and luminescence of LaPO₄:Eu nanoparticles from different phosphate sources, *J. Mater. Sci. Mater. Electron.* 25 (2014) 1264–1268. <https://doi.org/10.1007/s10854-014-1719-3>.
- [112] C. Sun, M. Gradzielski, Advances in fluorescence sensing enabled by lanthanide-doped upconversion nanophosphors, *Adv. Colloid Interface Sci.* 300 (2022) 102579. <https://doi.org/10.1016/j.cis.2021.102579>.
- [113] P. Zhang, L. Liang, X. Liu, Lanthanide-doped nanoparticles in photovoltaics – more than just upconversion, *J. Mater. Chem. C.* 9 (2021) 16110–16131. <https://doi.org/10.1039/D1TC02441H>.
- [114] P. Jethva, M. Momin, T. Khan, A. Omri, Lanthanide-Doped Upconversion Luminescent Nanoparticles—Evolving Role in Bioimaging, Biosensing, and Drug Delivery, *Materials (Basel)*. 15 (2022) 2374. <https://doi.org/10.3390/ma15072374>.
- [115] U. Cho, J.K. Chen, Lanthanide-Based Optical Probes of Biological Systems, *Cell Chem. Biol.* 27 (2020) 921–936.

- <https://doi.org/10.1016/j.chembiol.2020.07.009>.
- [116] J.G. Bünzli, Rising Stars in Science and Technology: Luminescent Lanthanide Materials, *Eur. J. Inorg. Chem.* 2017 (2017) 5058–5063. <https://doi.org/10.1002/ejic.201701201>.
- [117] Q.M. Le, T.H. Tran, T.H. Nguyen, T.K. Hoang, T.B. Nguyen, K.T. Do, K.A. Tran, D.H. Nguyen, T.L. Le, T.Q. Nguyen, M.D. Dang, N.A.T. Nguyen, M. Van Nguyen, Development of a fluorescent label tool based on lanthanide nanophosphors for viral biomedical application, *Adv. Nat. Sci. Nanosci. Nanotechnol.* 3 (2012). <https://doi.org/10.1088/2043-6262/3/3/035003>.
- [118] M. Toro-González, D.M. Clifford, R. Copping, S. Mirzadeh, J. V Rojas, Synthesis and characterization of intrinsically radiolabeled lanthanide phosphate nanoparticles toward biomedical and environmental applications, *J. Nanoparticle Res.* 20 (2018). <https://doi.org/10.1007/s11051-018-4338-8>.
- [119] V. Tucureanu, A. Matei, A.M. Avram, Synthesis and characterization of YAG:Ce phosphors for white LEDs, *Opto-Electronics Rev.* 23 (2015) 239–251. <https://doi.org/10.1515/oere-2015-0038>.
- [120] L. Mariscal-Becerra, S. Carmona-Téllez, R. Vázquez-Arreguín, C.M. García-Rosas, C. Falcony, H.M. S., M.A. Sánchez-Alejo, Green Light Emission in Aluminum Oxide Powders Doped with Different Terbium Concentrations, *Univers. J. Mater. Sci.* 4 (2016) 47–53. <https://doi.org/10.13189/ujms.2016.040301>.
- [121] Y.C. Kang, E.J. Kim, D.Y. Lee, H.D. Park, High brightness LaPO₄:Ce,Tb phosphor particles with spherical shape, *J. Alloys Compd.* 347 (2002) 266–270. [https://doi.org/10.1016/S0925-8388\(02\)00747-8](https://doi.org/10.1016/S0925-8388(02)00747-8).
- [122] S.K. Gupta, J.P. Zuniga, M. Abdou, M.P. Thomas, M. De Alwis Goonatilleke, B.S. Guiton, Y. Mao, Lanthanide-doped lanthanum hafnate nanoparticles as multicolor phosphors for warm white lighting and scintillators, *Chem. Eng. J.* 379 (2020) 122314. <https://doi.org/10.1016/j.cej.2019.122314>.
- [123] C. Kinowski, H. El Hamzaoui, B. Capoen, G. Bouwmans, A.-M. Blanchenet, K. Delplace, B. Prochet, M. Bouzaoui, YbPO₄ nanocylinders formation and alignment within optical fiber preforms using fiber-drawing process, *Mater. Res. Bull.* 97 (2018) 293–299. <https://doi.org/10.1016/j.materresbull.2017.09.014>.
- [124] D. Boivin, A. Pastouret, E. Burov, C. Gonnet, O. Cavani, S. Lempereur, P. Sillard, Performance characterization of new erbium-doped fibers using MCVD nanoparticle doping process, in: J.W. Dawson (Ed.), *Fiber Lasers VIII Technol. Syst. Appl.*, 2011: p. 791423. <https://doi.org/10.1117/12.873714>.
- [125] C.C. Baker, E.J. Friebele, C.G. Askins, M.P. Hunt, B.A. Marcheschi, J. Fontana, J.R. Peele, W. Kim, J. Sanghera, J. Zhang, R.K. Pattnaik, L.D. Merkle, M. Dubinskii, Y. Chen, I.A. Dajani, C. Mart,

- Nanoparticle doping for improved Er-doped fiber lasers, in: J. Ballato (Ed.), *Fiber Lasers XIII Technol. Syst. Appl.*, 2016: p. 97280T. <https://doi.org/10.1117/12.2217905>.
- [126] D.E. Boivin, A. Pastouret, E. Burov, C. Gonnet, O. Cavani, S. Lempereur, P. Sillard, C. Goldmann, E. Saudry, C. Chanéac, A. Shlifer, U. Ghera, Core-shell nanoparticle erbium-doped fibers for next generation amplifiers, in: *Fiber Lasers IX Technol. Syst. Appl.*, 2012: p. 82372T. <https://doi.org/10.1117/12.907909>.
- [127] I. Savelii, L. Bigot, B. Capoen, C. Gonnet, C. Chanéac, E. Burova, A. Pastouret, H. El-Hamzaoui, M. Bouazaoui, Benefit of Rare-Earth “Smart Doping” and Material Nanostructuring for the Next Generation of Er-Doped Fibers, *Nanoscale Res. Lett.* 12 (2017). <https://doi.org/10.1186/s11671-017-1947-6>.
- [128] J. Thomas, M. Myara, L. Troussellier, E. Burov, A. Pastouret, D. Boivin, G. Mélin, O. Gilard, M. Sotom, P. Signoret, Radiation-resistant erbium-doped-nanoparticles optical fiber for space applications, *Opt. Express.* 20 (2012) 2435. <https://doi.org/10.1364/oe.20.002435>.
- [129] X. Chen, T. Sun, F. Wang, Lanthanide-Based Luminescent Materials for Waveguide and Lasing, *Chem. – An Asian J.* 15 (2020) 21–33. <https://doi.org/10.1002/asia.201901447>.
- [130] S. Moynihan, R. Van Deun, K. Binnemans, G. Redmond, Optical properties of planar polymer waveguides doped with organolanthanide complexes, *Opt. Mater. (Amst.)* 29 (2007) 1821–1830. <https://doi.org/10.1016/j.optmat.2006.10.005>.
- [131] V. Kumar, S. Singh, S. Chawla, Fabrication of dual excitation, dual emission nanophosphor with broad UV and IR excitation through simultaneous doping of triple rare earth ions Er^{3+} , Yb^{3+} , Eu^{3+} in GdPO_4 , *Superlattices Microstruct.* 79 (2015) 86–95. <https://doi.org/10.1016/j.spmi.2014.12.003>.
- [132] H. Thakur, A.K. Gathania, I. Kumar, R.K. Singh, Tunable white light photoluminescence of a single phase $\text{Tm}^{3+}/\text{Tb}^{3+}/\text{Eu}^{3+}$ codoped GdPO_4 phosphor, *Mater. Today Commun.* 36 (2023) 106458. <https://doi.org/10.1016/j.mtcomm.2023.106458>.
- [133] B. Wang, S. Jiang, X. Wang, S. Gao, Magnetic molecular materials with paramagnetic lanthanide ions, *Sci. China, Ser. B Chem.* 52 (2009) 1739–1758. <https://doi.org/10.1007/S11426-009-0275-9/METRICS>.
- [134] S. Viswanathan, Z. Kovacs, K.N. Green, S.J. Ratnakar, A.D. Sherry, Alternatives to gadolinium-based metal chelates for magnetic resonance imaging, *Chem. Rev.* 110 (2010) 2960–3018. https://doi.org/10.1021/CR900284A/ASSET/IMAGES/CR-2009-00284A_M034.GIF.
- [135] J.C.G. Bünzli, C. Piguet, Taking advantage of luminescent lanthanide ions, *Chem. Soc. Rev.* 34 (2005) 1048–1077.

- <https://doi.org/10.1039/b406082m>.
- [136] M.R. Rafiuddin, A.P. Grosvenor, A Structural Investigation of Hydrous and Anhydrous Rare-Earth Phosphates, *Inorg. Chem.* 55 (2016) 9685–9695. <https://doi.org/10.1021/acs.inorgchem.6b01471>.
- [137] M.R. Rafiuddin, A.P. Grosvenor, An investigation of the chemical durability of hydrous and anhydrous rare-earth phosphates, *J. Nucl. Mater.* 509 (2018) 631–643. <https://doi.org/10.1016/j.jnucmat.2018.07.039>.
- [138] E.H. Oelkers, J.-M. Montel, Phosphates and Nuclear Waste Storage, *Elements.* 4 (2008) 113–116. <https://doi.org/10.2113/GSELEMENTS.4.2.113>.
- [139] K. Rajesh, P. Shajesh, O. Seidel, P. Mukundan, K.G.K. Warriar, A facile sol-gel strategy for the synthesis of rod-shaped, nanocrystalline, high-surface-area lanthanum phosphate powders and nanocoatings, *Adv. Funct. Mater.* 17 (2007) 1682–1690. <https://doi.org/10.1002/adfm.200600794>.
- [140] Y. Wu, X. Xu, X. You, Q. Xiao, Synthesis of mesoporous core-shell structured $\text{GdPO}_4:\text{Eu}@ \text{SiO}_2@ \text{mSiO}_2$ nanorods for drug delivery and cell imaging applications, *J. Rare Earths.* 38 (2020) 1086–1092. <https://doi.org/10.1016/j.jre.2020.01.008>.
- [141] J. Huang, Z. Lv, Y. Wang, Z. Wang, T. Gao, N. Zhang, M. Guo, H. Zou, P. Zhang, In Vivo MRI and X-Ray Bifunctional Imaging of Polymeric Composite Supplemented with $\text{GdPO}_4 \cdot \text{H}_2\text{O}$ Nanobundles for Tracing Bone Implant and Bone Regeneration, *Adv. Healthc. Mater.* 5 (2016) 2182–2190. <https://doi.org/10.1002/adhm.201600249>.
- [142] Y. Tang, R. Mei, S. Yang, H. Tang, W. Yin, Y. Xu, Y. Gao, Hollow $\text{GdPO}_4:\text{Eu}^{3+}$ microspheres: Luminescent properties and applications as drug carrier, *Superlattices Microstruct.* 92 (2016) 256–263. <https://doi.org/10.1016/J.SPMI.2016.02.038>.
- [143] M. Kumari, S. Mondal, P.K. Sharma, Synthesis, characterization and electrochemical monitoring of drug release properties of dual stimuli responsive mesoporous $\text{GdPO}_4:\text{Eu}^{3+}$ nanoparticles, *J. Alloys Compd.* 776 (2019) 654–665. <https://doi.org/10.1016/J.JALLCOM.2018.10.286>.
- [144] J. Raudoniene, R. Skaudzius, A. Zarkov, A. Selskis, O. Karlsson, A. Kareiva, E. Garskaite, Wet-chemistry synthesis of shape-controlled Ag_3PO_4 crystals and their 3D surface reconstruction from SEM imagery, *Powder Technol.* 345 (2019) 26–34. <https://doi.org/10.1016/j.powtec.2018.12.091>.
- [145] R. Skaudzius, A. Katelnikovas, D. Enseling, A. Kareiva, T. Jüstel, Dependence of the $5\text{D}_0 \rightarrow 7\text{F}_4$ transitions of Eu^{3+} on the local environment in phosphates and garnets, *J. Lumin.* 147 (2014) 290–294. <https://doi.org/10.1016/j.jlumin.2013.11.051>.
- [146] R. Reisfeld, E. Zigansky, M. Gaft, Europium probe for estimation of

- site symmetry in glass films, glasses and crystals, *Mol. Phys.* 102 (2004) 1319–1330. <https://doi.org/10.1080/00268970410001728609>.
- [147] K.S.W.S. and K.K.U. J. Rouquerol, D. Avnir, C. W. Fairbridge, D. H. Everett, J. M. Haynes, N. Pernicone, J. D. F. Ramsay, Recommendations for the characterization of porous solids (Technical Report), *Pure Appl. Chem.* 66 (1994) 1739–1758. <https://doi.org/10.1351/pac199466081739>.
- [148] J. Rouquerol, D. Avnir, D.H. Everett, C. Fairbridge, M. Haynes, N. Pernicone, J.D.F. Ramsay, K.S.W. Sing, K.K. Unger, Guidelines for the Characterization of Porous Solids, *Stud. Surf. Sci. Catal.* 87 (1994) 1–9. [https://doi.org/10.1016/S0167-2991\(08\)63059-1](https://doi.org/10.1016/S0167-2991(08)63059-1).
- [149] J.L. Sebaugh, Guidelines for accurate EC50/IC50 estimation, *Pharm. Stat.* 10 (2011) 128–134. <https://doi.org/10.1002/pst.426>.
- [150] G. Demirel, F.F. Kaya Demirsoy, Ö. Irmak, Cytotoxicity evaluation of eluates from universal adhesives by real-time cell analysis, *Dent. Mater. J.* 39 (2020) 815–824. <https://doi.org/10.4012/dmj.2019-221>.

SUMMARY IN LITHUANIAN

ĮVADAS

Dėl stiprios gadolinio paramagnetinės prigimties Gd pagrindu pagamintos medžiagos dažniausiai naudojamos medicinoje kaip magnetinio rezonanso tyrimo (MRT) kontrastinė medžiaga. Tačiau dar 2009 m. pasaulio sveikatos organizacija apribojo kai kurių komercinių chelatinių gadolinio kontrastinių medžiagų naudojimą pacientams, turintiems inkstų problemų. Taip yra, nes Gd^{3+} jonai yra labai toksiški. Net ir gadolinio junginiai chelatų pavidalu kelia Gd^{3+} išsiskyrimo į organizmą riziką. Nors MRT yra galingas medicininės diagnostikos metodas, vis dar reikia naujų būdų pagerinti vaizdavimą. Vienmodė MRT ne visada užtikrina pakankamą vaizdo kokybę, todėl siekiant pagerinti MRT kokybę, kuriamos ir naudojamos medžiagos, kurios leidžia kartu gauti T1 ir T2 MRT vaizdus. Taip pat kuriamos multimodalinės medžiagos, tinkamos biovaizdavimui ir MRT. Tai gana nelengva užduotis, nes medicinos reikmėms naudojamos medžiagos turi atitikti itin griežtus kriterijus. Labai svarbu, kad medicinoje naudojamos medžiagos būtų netoksiškos ir biologiškai suderinamos. Dažnai stebimas toksiškų Gd^{3+} jonų patekimas į organizmą, kai naudojami gadolinio pagrindu pagaminti kompleksiniai junginiai kaip MRT kontrastinės medžiagos.

$GdPO_4$ nanodalelės yra netoksiškos, nes Gd^{3+} jonai daug rečiau patenka į žmogaus organizmą. Be to, lantanoidai yra tinkami $GdPO_4$ nanodalelių legiravimui. Junginiai, legiruoti europiu, pasižymi ~ 577 nm, ~ 590 nm, ~ 615 nm, ~ 650 ir ~ 700 nm bangos ilgio emisija. Atsižvelgiant į junginių poreikį biovaizdavimui, tai yra gana patrauklu, nes dalis emisijos (700 nm ir didesnio bangos ilgio) patenka į taip vadinamą pirmąjį biologinį langą ir yra daug mažiau absorbuojama audinių. Taigi, Eu^{3+} legiruotos $GdPO_4$ nanodalelės pritraukia daug dėmesio kaip potencialus efektyvus vienfazis multimodalinis nanozondas, pasižymintis ir liuminescencinėmis, ir magnetinėmis savybėmis.

Nors europis gana dažnai naudojamas ruošiant įvairius oranžinės–raudonos spalvos liuminescencinėmis savybėmis pasižyminčius junginius, tačiau legiruojant net ir mažomis Eu^{3+} koncentracijomis, reikalingas tolesnis optimizavimas ir tyrimas, nes jei į kristalų struktūrą patenka per didelė liuminescencinių centrų koncentracija, stebimas koncentracinis gesinimas. Europio atveju ši riba gali smarkiai kisti, priklausomai nuo junginio matricos. Siekiant užtikrinti geriausias fotoluminescencijos ir scintiliacijos savybes, vienkristalinio scintiliatoriaus $Ca_2MgSi_2O_7$ atveju optimali legiruoto Eu^{3+} koncentracija yra 10%, o $LiCaAlF_6:Eu$ monokristalams

optimali Eu^{3+} jonų koncentracija yra 2–2,5%. Tuo tarpu GdPO_4 nanodalelių legiruotų Eu^{3+} , kurios buvo sintetintos etilenglikolyje ir vėliau kaitinamos, intensyviausia emisija yra kai Eu^{3+} koncentracija yra 5–7%. Reikia pažymėti, kad liuminescencijos intensyvumas priklauso ne tik nuo medžiagos kristalinės struktūros, bet ir nuo dalelių dydžio, ilgio ir pločio santykio, dalelių formos ir sintezės temperatūros. Nepriklausomai nuo kristalinės aplinkos, Eu^{3+} jonai paprastai skleidžia raudoną šviesą, kai sužadinami UV spinduliuote. Tam tikrais atvejais silpnos emisijos juostos taip pat gali būti žalios, o kartais ir mėlynos spalvos diapazone. Svarbu ne tik emisija, bet ir dalelių forma, kuri turi įtakos praktiniam pritaikymui. Pastaruoju metu buvo pademonstruota, kad į „ežius“ panašios $\text{GdPO}_4 \cdot \text{H}_2\text{O} : 5\text{Eu}^{3+}$ nanodalelės, gali prasiskverbti į plaučių vėžio A549 ląsteles ir dėl savo liuminescencinių savybių gali būti naudojamos biovaizdavimui. Nors mokslinėje literatūroje gana plačiai aptariami GdPO_4 junginiai, tačiau tai vis dar daug dėmesio ir atsakymų reikalaujantis tyrimų objektas.

Kaip minėta anksčiau, kristalinės gardelės struktūra ir dalelių morfologija yra labai svarbūs, norint gauti didelio intensyvumo liuminescenciją. Pastaruoju metu mokslinėje literatūroje galima rasti publikacijų, kuriose monoklininės kristalinės struktūros GdPO_4 nanodalelės, legiruotos 5% Eu^{3+} , pasižymi geresnėmis liuminescencinėmis savybėmis, palyginus su heksagoninės kristalinės struktūros nanodalelėmis. Vandens terpėje susintetinti GdPO_4 mėginiai, legiruoti Eu^{3+} , gaunami heksagoninės kristalinės struktūros. Juos kaitinant virš 700 °C temperatūroje, vanduo pašalinamas, struktūra persitvarko iš heksagoninės į monoklininę. Tačiau šiuo atveju pasikeičia ne tik kristalinė struktūra, bet greičiausiai ir mėginių kristališkumas bei dalelių dydis, todėl vienam iš šių reiškinių sunku priskirti liuminescencinių savybių pagerėjimą, nes jie visi gali tam turėti įtakos. Mėginiai, susintetinti bevandenėje terpėje iškart gaunami monoklininės struktūros, tačiau tai reikalauja pakankamai aukštos temperatūros, o tai apsunkina gauti nanodaleles.

Ieškoma kitų būdų, kaip gauti norimos kristalinės struktūros junginius. Pavyzdžiui, lantano fosfatą galima gauti dviejų kristalinių struktūrų pavidalu: hidratuoto heksagoninio rabdofano tipo ir monoklininio monazito tipo. $\text{LaPO}_4 \cdot n\text{H}_2\text{O}$ legiruoto Eu^{3+} , Tb^{3+} monazito tipo nanostypeliai pasižymi didesniu fotoluminescenciniu efektyvumu nei $\text{LaPO}_4 \cdot n\text{H}_2\text{O}$ legiruoto tokiu pat kiekiu Eu^{3+} , Tb^{3+} rabdofano tipo nanostypeliai. Yra žinoma, kad labiausiai paplitusios GdPO_4 nanodalelės yra hidratatai, tuo tarpu LaPO_4 nanodalelės dažniau gaunamos bevandenės net ir iš vandeninės terpės be papildomo atkaitinimo. GdPO_4 monoklininio anhidrato stabilizavimas La^{3+}

jonais galėtų pagerinti fosforo liuminescencines savybes, lyginant su hidratuota junginio forma.

Atsižvelgdami į visa tai, šioje disertacijoje tiriama optimali Eu^{3+} koncentracija, lemianti intensyvesnę mėginių emisiją. Taip pat tiriamas poveikis kristalinei struktūrai, liuminescencinėms savybėms ir citotoksiškumui palaipsniui keičiant Gd^{3+} jonus La^{3+} jonais.

Tikslas – susintetinti magnetinių savybių turinčius lantanoidų fosfatų bevandenius junginius, kurie potencialiai galėtų būti naudojami multimodaliniam vaizdavimui.

Šio tyrimo uždaviniai yra šie:

- nustatyti ir ištirti optimalią Eu^{3+} koncentraciją;
- ištirti, kaip keičiant sintezės sąlygas keičiasi susintetintų nanodalelių dydis ir jų liuminescencinės savybės;
- susintetinti norimos kristalinės struktūros Eu^{3+} legiruotų GdPO_4 nanodaleles;
- ištirti sintetintų dalelių kristalinę struktūrą, liuminescencines ir magnetines savybes, toksiškumą

Tyrimo naudojami įvairūs junginių apibūdinimo metodai, tokie kaip rentgeno spindulių difrakcija, spektroskopija ir magnetiniai matavimai. Analizuojama dalelių dydžio, ilgio ir pločio santykio, formos ir kristalinės struktūros įtaka nanodalelių liuminescencinėms savybėms. Įvertinamas GdPO_4 nanodalelių, legiruotų Eu^{3+} , citotoksiškumas, siekiant užtikrinti jų biologinį suderinamumą. Ši analizė yra labai svarbi nustatant nanodalelių tinkamumą biomedicinos reikmėms. Apskritai tyrimu siekiama prisidėti prie lantanido fosfato nanodalelių, su optimizuotomis liuminescencinėmis ir magnetinėmis savybėmis, skirtų naudoti multimodaliniam biologiniam vaizdavimui, kūrimo.

Darbo naujumas ir originalumas:

Pirmą kartą GdPO_4 nanodalelėms susintetintoms hidroterminiu metodu, nustatytas optimalus Eu^{3+} kiekis maksimaliai liuminescencijai gauti. Taip pat pirmą kartą buvo įrodyta, kad $\text{Gd}_{0,85}\text{Eu}_{0,15}\text{PO}_4 \cdot \text{H}_2\text{O}$ nanodalelių dydis gali būti reguliuojamas keičiant hidroterminio reaktoriaus užpildymo tūrį. Pirmą kartą hidroterminės sintezės būdu, nenaudojant papildomo medžiagos apdorojimo po sintezės (kaitinimo), gautos $\text{La}_{0,61}\text{Gd}_{0,24}\text{PO}_4:15\%\text{Eu}$ ir $\text{La}_{0,75}\text{Gd}_{0,1}\text{PO}_4:15\%\text{Eu}$ vienfazės monoklininės kristalinės struktūros nanodalelės.

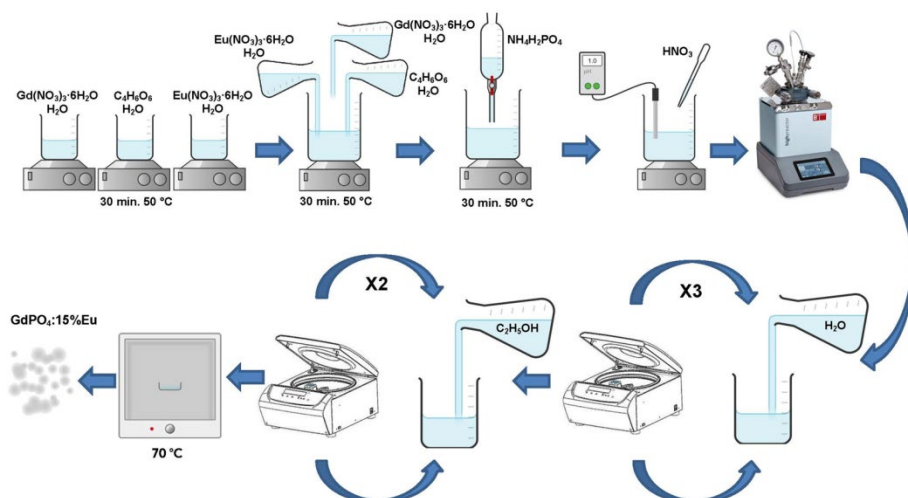
Ginamieji teiginiai:

- Gadolinio fosfato nanodalelių intensyviausia emisija pasiekama, kai legiruoto Eu^{3+} kiekis yra 15%.

- Eu^{3+} legiruočių GaPO_4 nanodalelių dydis priklauso nuo hidroterminio reaktoriaus užpildymo.
- PO_4^{3-} pirmtakas hidroterminės sintezės metu daro įtaką galutiniam produktui, jo kristalinei struktūrai ir morfologijai.
- Šiame darbe susintetintos dalelės pasižymi magnetinėmis ir liuminescencinėmis savybėmis, yra netoksiškos, todėl gali būti naudojami multimodaliniam vaizdavimui.

EKSPERIMENTO METODIKA

Visi miltelių pavidalo junginiai buvo sintetinti hidroterminiu metodu. Principinė sintezės schema pateikta 1 pav.



1 pav. Principinė sintezės schema.

Gauti mėginiai buvo tiriami skenuojančiu elektronų mikroskopu (SEM), atlikta rentgeno spindulių difrakcijos analizė (XRD), tirtos liuminescencinės savybės, atliktas $\text{Gd}_{0,85}\text{-yLa}_y\text{PO}_4:15\%\text{Eu}$ mėginių citotoksiškumo ir paviršiaus ploto ir porų dydžio tyrimas bei magnetinės savybės.

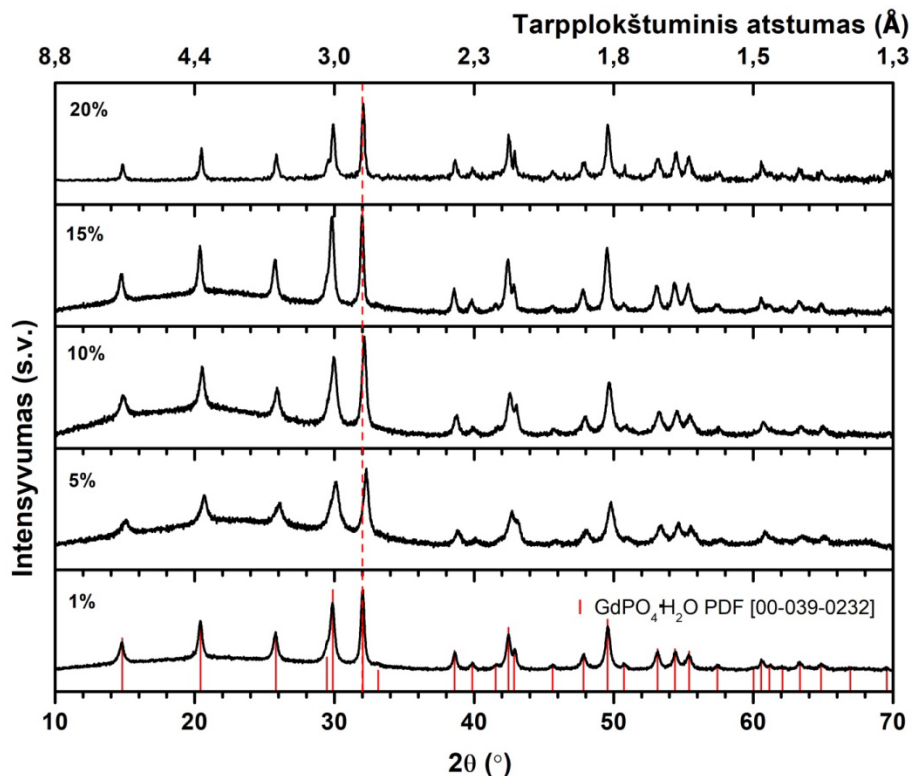
REZULTATAI IR JŲ APTARIMAS

1. Optimalios europio koncentracijos $\text{Gd}_{1-x}\text{Eu}_x\text{PO}_4 \cdot \text{H}_2\text{O}$ tyrimas

Šiame darbe pasirinktas hidroterminės sintezės metodas, nes jis užtikrina aukštą produkto grynumą ir kristališkumą, tikslią dalelių charakteristikų kontrolę ir galimybę sukurti siauro dydžio pasiskirstymo nanodaleles.

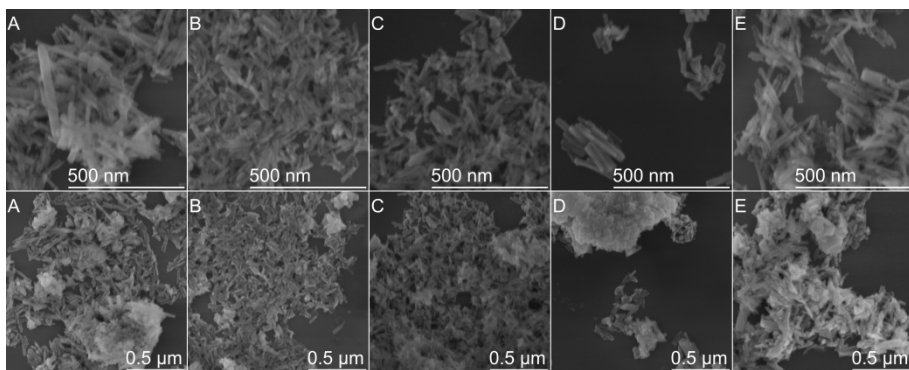
Hidroterminis metodas yra ypač naudingas biomedicinoje, nes jį panaudojant galima sukurti specifinių dydžių, formų ir paviršiaus savybių nanodaleles.

Siekiant nustatyti optimalų Eu^{3+} kiekį legiruojant gadolinio fosfatą, buvo atlikta serija sintezių, keičiant Eu^{3+} kiekį nuo 1% iki 20%. Norint iširti susintetintų junginių fazinę sudėtį ir kristalinę struktūrą, buvo naudojama rentgeno spindulių difrakcijos (XRD) analizė. Rentgeno spindulių difraktogramos pavaizduotos 2 paveiksle. Visos pateiktose difraktogramose esančios smaيليų padėty s gerai atitinka duomenų bazėje esančio standarto smaيليų padėtis, tad yra priskiriamos heksagoninei $\text{GdPO}_4 \cdot \text{H}_2\text{O}$ kristalinei struktūrai (erdvinė grupė P3121 (#152), PDF ICDD 00-039-0232). Net esant 20% europio nėra jokių antrinių fazių požymių, rentgeno spindulių difraktogramose neatsiranda nepriskirtų smaيليų. Tai rodo, kad visas europis buvo sėkmingai įterptas į heksagoninę gadolinio fosfato struktūrą. Verta pažymėti, kad net 20% gadolinio pakeitus europiu, nėra aiškių smaيليų poslinkio, tai gali būti dėl gadolinio ir europio jonų spindulių panašumo. Literatūros duomenimis, gadolinio ir europio jonų spinduliai yra atitinkamai 1,06 Å ir 1,07 Å. Mėginiui, kuriame yra 5% Eu^{3+} , matomas poslinkis, tikėtina gautas dėl mėginio paruošimo. Tačiau yra aiškus smaيليų padėčių skirtumas tarp skirtingų difraktogramų, pateiktų 2 paveiksle. Visų pirma, mėginiams, kuriuose yra nuo 5 iki 15 procentų europio, fonas ties 5-35° 2θ laipsnio diapazone pasižymi didesniu intensyvumu nei kituose mėginiuose. Fono intensyvumo skirtumus gali lemti nevienodas mėginio paruošimas matavimo metu, mėginio amorfiškumas.



2 pav. $Gd_{1-x}PO_4:Eu_x \cdot H_2O$, turinčio skirtingą europio kiekį, Rentgeno spindulių difraktogramos.

Siekiant papildyti XRD duomenis ir apibūdinti dalelių morfologiją, buvo atlikta skenuojančio elektronų mikroskopo (SEM) vaizdų analizė. Gauti rezultatai pateikti 3 paveiksle. Iš pateiktų vaizdų matyti, kad nepriklausomai nuo europio kiekio dalelės susidaro pailgos lazdelės formos, kurios vėliau agreguojasi į didesnes grupes. Eu^{3+} koncentracija mėginyje neturi įtakos dalelių formai. Iš SEM vaizdų naudojant Fiji programinę įrangą, buvo išmatuoti dalelių ilgis ir plotis. Dalelių ilgio ir pločio pasiskirstymo rezultatai pateikti 1 lentelėje. Išmatuoti vidutiniai dalelių dydžiai visuose mėginiuose yra panašūs. Galima teigti, kad Eu^{3+} koncentracija neturi didelės įtakos susidarantių dalelių dydžiui.

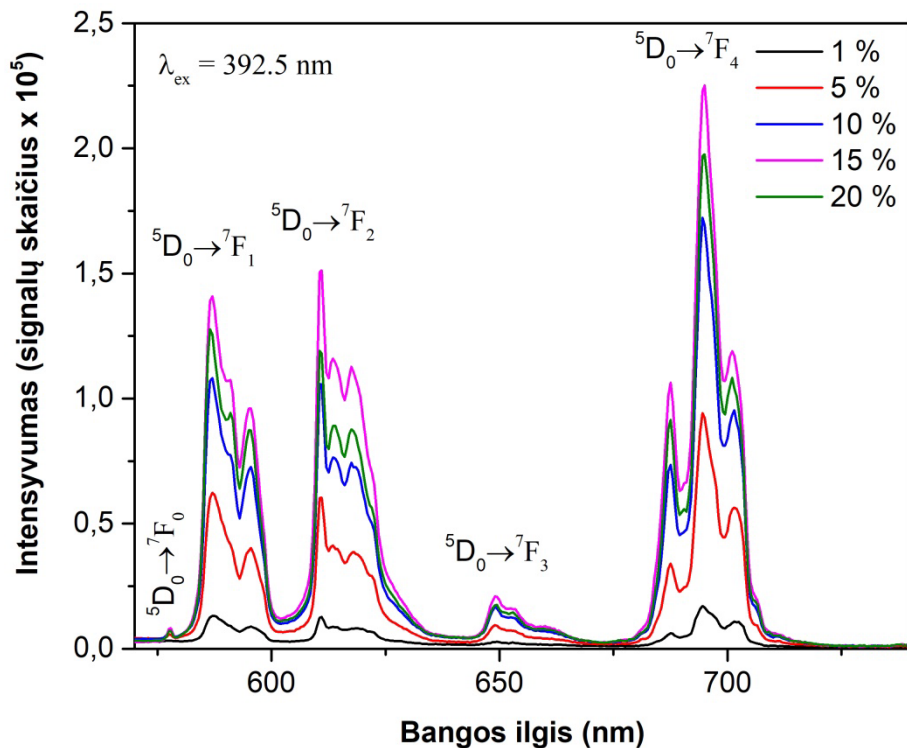


3 pav. $Gd_{1-x}PO_4:Eu_x \cdot H_2O$, susintetinto hidroterminiu metodu, SEM vaizdai: A) $x = 0,20$, B) $x = 0,15$, C) $x = 0,1$, D) $x = 0,05$ ir E) $x = 0,01$

1 lentelė Vidutinis dalelių ilgis ir plotis

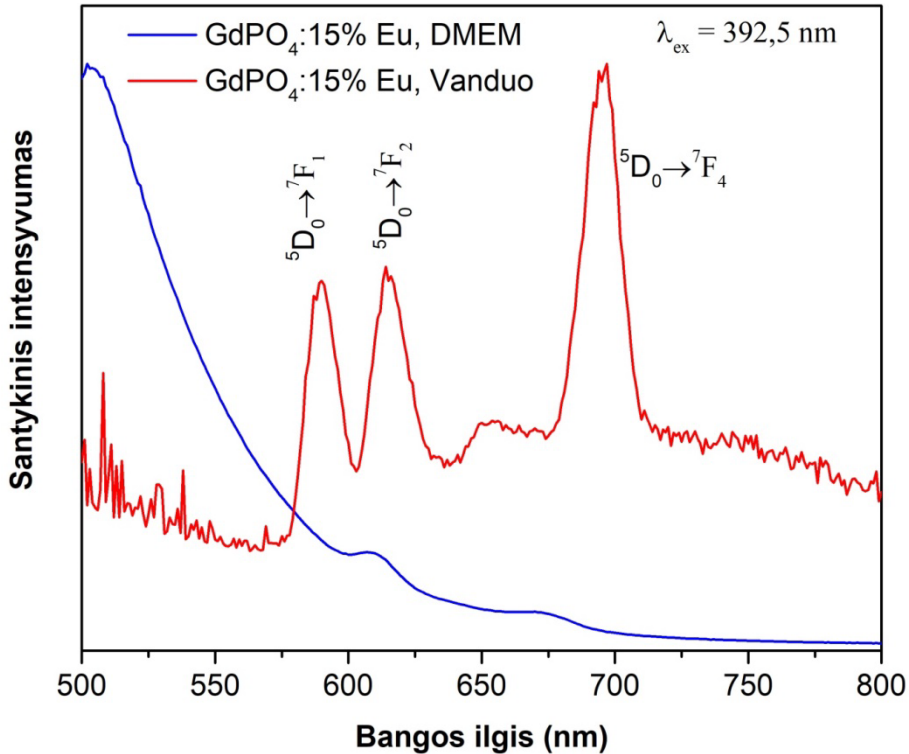
Mėginys	Ilgis, nm	Standartinis nuokrypis, nm	Plotis, nm	Standartinis nuokrypis, nm	Ilgio ir pločio santykis
20% Eu^{3+}	123	66	22	7	5,5
15% Eu^{3+}	88	22	18	5	5,0
10% Eu^{3+}	94	20	17	7	5,4
5% Eu^{3+}	108	48	21	7	5,3
1% Eu^{3+}	118	37	19	7	6,3

Sintetintų miltelių emisijos spektrai pateikti 4 paveiksle. Emisijos spektrai matuoti esant 392,5 nm sužadanimui. Raudonos spalvos luminoforuose yra visi Eu^{3+} jonui būdingi $^5D_0 \rightarrow ^7F_J$ perėjimai: $^5D_0 \rightarrow ^7F_0$, $^5D_0 \rightarrow ^7F_1$, $^5D_0 \rightarrow ^7F_2$, $^5D_0 \rightarrow ^7F_3$ ir $^5D_0 \rightarrow ^7F_4$. Intensyviausios charakteringos smailės stebimos ties ~ 577 nm, ~ 590 nm, ~ 615 nm, ~ 650 nm ir ~ 690 nm ir yra priskiriamos anksčiau minėtiems atitinkamiems perėjimams. Labiausiai dominuojantys yra $^5D_0 \rightarrow ^7F_4$ elektronų perėjimai. Emisijos intensyvumas palaipsniui didėja, kai europio kiekis didėja nuo 1 iki 15 mol%. Tačiau kai europio procentinė dalis pasiekia 20 mol%, emisijos intensyvumas sumažėja. Viršijama optimali europio koncentracija, tad stebimas koncentracinis gesimas, dėl kurio $Gd_{0,80}Eu_{0,20}PO_4 \cdot H_2O$ mėginio emisijos intensyvumas yra mažesnis nei $Gd_{0,85}Eu_{0,15}PO_4 \cdot H_2O$ mėginyje. Visi minėti rezultatai leidžia daryti išvadą, kad iš pateiktų junginių 15% europiu legiruotas mėginys yra perspektyviausias ir tokiu Eu^{3+} kiekiu legiruoti mėginiai bus naudojami tolesniems tyrimams ir analizei.



4 pav. Gd_{1-x}PO₄:Eu_x·H₂O junginių, legiruočių skirtingais europio kiekiais, emisijos spektrai.

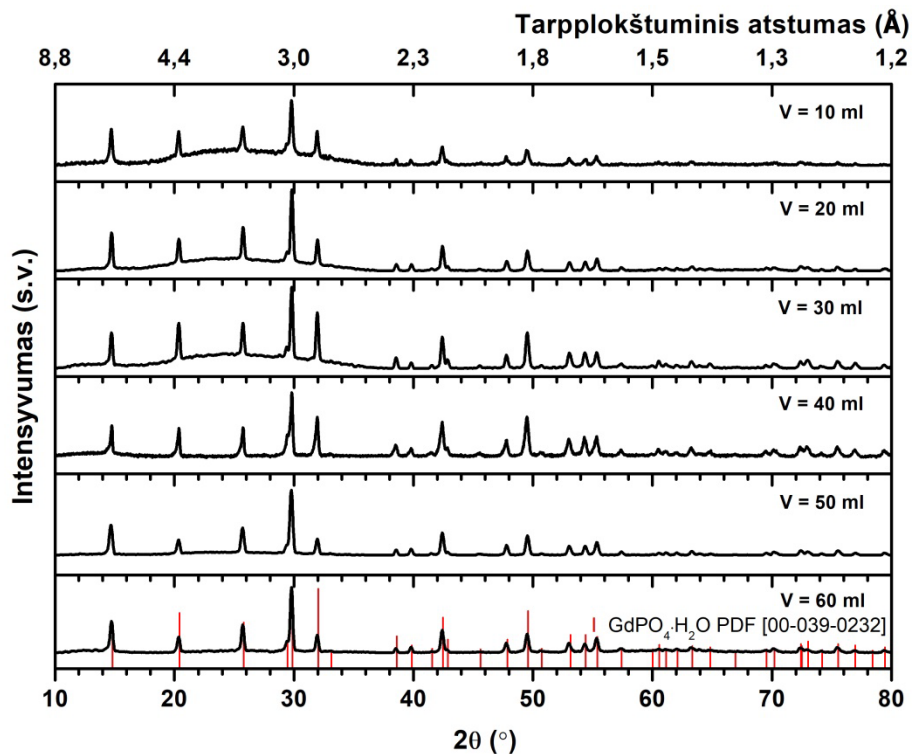
Siekiant ištirti mėginių elgseną tikroviškesnėje aplinkoje, mėginys pasižymėjęs intensyviausia emisija buvo išbandytas įvairiuose tirpaluose. Mėginiai buvo paruošti maišant Gd_{0,85}Eu_{0,15}PO₄·H₂O su vandeniu santykiu 1 mg-10 ml arba su Dulbecco modifikuota Eagle terpe (DMEM) santykiu 0,5 mg su 3 ml. Gauti emisijos spektrai pateikti 5 paveiksle. Europio emisijos signalas stebimas vandenyje, o DMEM tirpalo autofluorescencija užgožia europio emisiją. Norint naudoti susintetintas daleles biovaizdavimui, liuminescencija turėtų būti pagerinta.



5 pav. GdPO₄:15%Eu emisijos spektrai DMEM ir vandens tirpale.

2. Gd_{0,8}Eu_{0,15}PO₄·H₂O nanodalelių dydžio priklausomybės nuo reaktoriaus tūrio užpildymo tyrimas

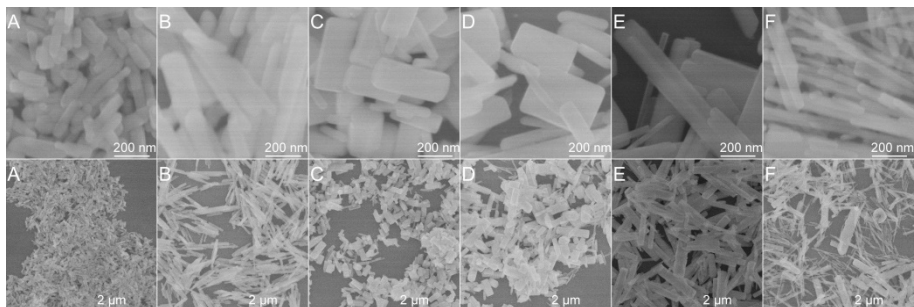
Kadangi yra labai svarbu turėti galimybę gauti norimo dydžio nanodaleles, buvo keičiamas hidroterminio reaktoriaus užpildymas. Gautiems mėginiams pirmiausiai buvo atlikti Rentgeno spindulių difrakcijos tyrimai. Visų mėginių nepriklausomai nuo sintezės sąlygų, XRD analizė pademonstravo, kad buvo gauti gryni vienfaziai mėginiai. Gd_{0,85}Eu_{0,15}PO₄·H₂O mėginių XRD difraktogramos (6 pav.) atitinka heksagoninio gadolinio fosfato hidrato standarto duomenis (erdvinė grupė P3121 (152), etaloninio junginio gardelės parametrai $a = 6,9055 \text{ \AA}$ $c = 6,3257 \text{ \AA}$; PDF $\text{\AA}DD30061.00-039-0232$). Kai kuriais atvejais pastebimas fono padidėjimas. Fono padidėjimas mėginiuose, kurie buvo susintetinti kai $V = 10 \text{ ml}$, $V = 20 \text{ ml}$, $V = 30 \text{ ml}$ sąlygomis, atsiranda dėl mažesnių dalelių susidarymo esant skirtingomis sintezės sąlygomis. Dalelių dydis bus išsamiau aptartas SEM duomenų analizės metu. Susidarius didesnėms dalelėms, didėja smailių intensyvumas, mažėja fonas.



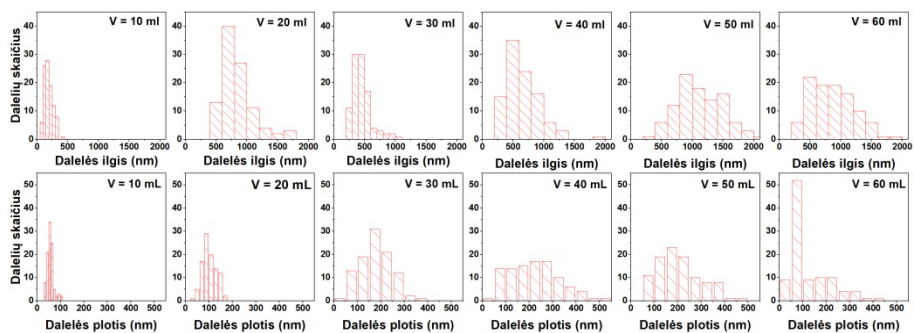
6 pav. $\text{Gd}_{0.85}\text{Eu}_{0.15}\text{PO}_4 \cdot \text{H}_2\text{O}$ mėginių, susintetintų naudojant skirtingus tirpiklio (H_2O) kiekius hidroterminio autoklavo reaktoriuje, Rentgeno spindulių difraktogramos.

Siekiant ištirti susintetintų dalelių morfologiją buvo atliktas SEM tyrimas. Visos susintetintos dalelės yra lazdelės formos, ir dalelių dydis gali būti kontroliuojamas keičiant tirpiklio kiekį (7 pav.). Dalelių ilgis ir plotis buvo išmatuoti naudojant Fiji programinę įrangą, pasirinkus atsitiktines 100 dalelių. Dalelių ilgio ir pločio pasiskirstymo rezultatai pateikti histogramose 8 paveiksle. Histogramose matome, kad sintezei panaudojus mažiausią tūrį $V = 10$ ml, gaunamos mažiausios dalelės: ilgis svyruoja nuo 50 nm iki 450 nm, plotis nuo 30 nm iki 110 nm. Dvigubai padidinus tūrį $V = 20$ ml, dalelių ilgis smarkiai padidėja nuo 500 nm iki 1800 nm, o plotis – nuo 20 nm iki 180 nm. Tai galima paaiškinti tuo, kad didinant tūrį tirpalo koncentracija mažėja. Yra žinoma, kad kuo didesnė tirpalo koncentracija, tuo mažesnis energijos barjeras branduolių susidarymui. Tai reiškia, kad kristalai greičiau formuojasi branduoliais ir gaunama daugiau dalelių, bet mažesnių. Toliau didėjant tūriui $V = 30$ ml ir atitinkamai mažėjant tirpalo koncentracijai, susidaro šiek tiek trumpesnės 200 nm–1100 nm, bet didesnio skersmens

10 nm–400 nm dalelės. Dalelės, susintetintos esant didesniai tirpalo tūriui ($V = 40$ ml, $V = 50$ ml ir $V = 60$ ml), gaunamos nevienodo dydžio, smulkios ir didelės dalelės.



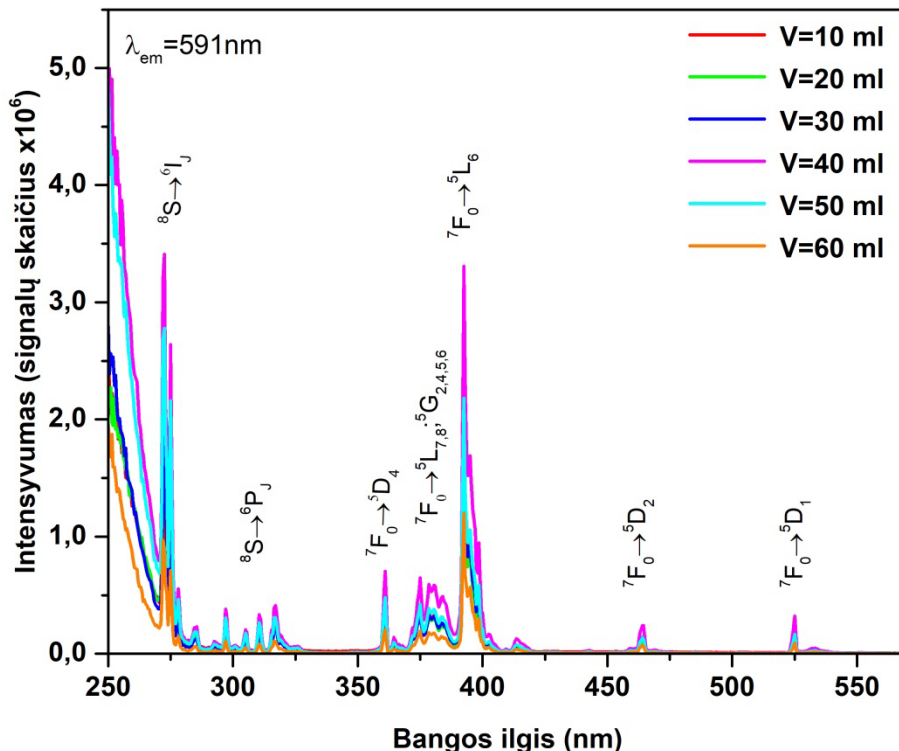
7 pav. $Gd_{0,85}Eu_{0,15}PO_4 \cdot H_2O$ mėginių, susintintų naudojant skirtingus tirpiklio (H_2O) kiekius hidroterminio autoklavo reaktoriuje, SEM vaizdai: (A) $V = 10$ ml, (B) $V = 20$ ml, (C) $V = 30$ ml, (D) $V = 40$ ml, (E) $V = 50$ ml, (F) $V = 60$ ml.



8 pav. $Gd_{0,85}Eu_{0,15}PO_4 \cdot H_2O$ nanolazdelių, susintintų naudojant skirtingus tirpiklio (H_2O) kiekius hidroterminio autoklavo reaktoriuje, ilgio ir pločio histogramos.

Ištirtos visų skirtingomis sąlygomis susintintų mėginių luminescencinės savybės (9 ir 10 pav.). Visi $Gd_{0,85}Eu_{0,15}PO_4 \cdot H_2O$ mėginiai buvo balti, todėl mėginiai turėtų turėti mažą absorbciją matomo spektro diapazone. Sužadinimo spektrai buvo matuoti nuo 250 nm iki 585 nm diapazone, kai emisijos bangos ilgis $\lambda_{em} = 591$ nm. Didesnės energijos (nuo 250 nm iki 270 nm) diapazone matoma plati juosta. Taip yra dėl krūvio pernašos – energijos perdavimo iš O^{2-} į Eu^{3+} . Siauros smailės 275 nm ir 310 nm diapazone priskiriamos Gd^{3+} jonų $^8S \rightarrow ^6I_J$ ir $^8S \rightarrow ^6P_J$ perėjimams. Sužadinant Eu^{3+} emisijai būdingą smailę, stebimos Gd^{3+} sužadinimo smailės, taigi vyksta energijos pernaša iš Gd^{3+} į Eu^{3+} jonus. Likusios sužadinimo

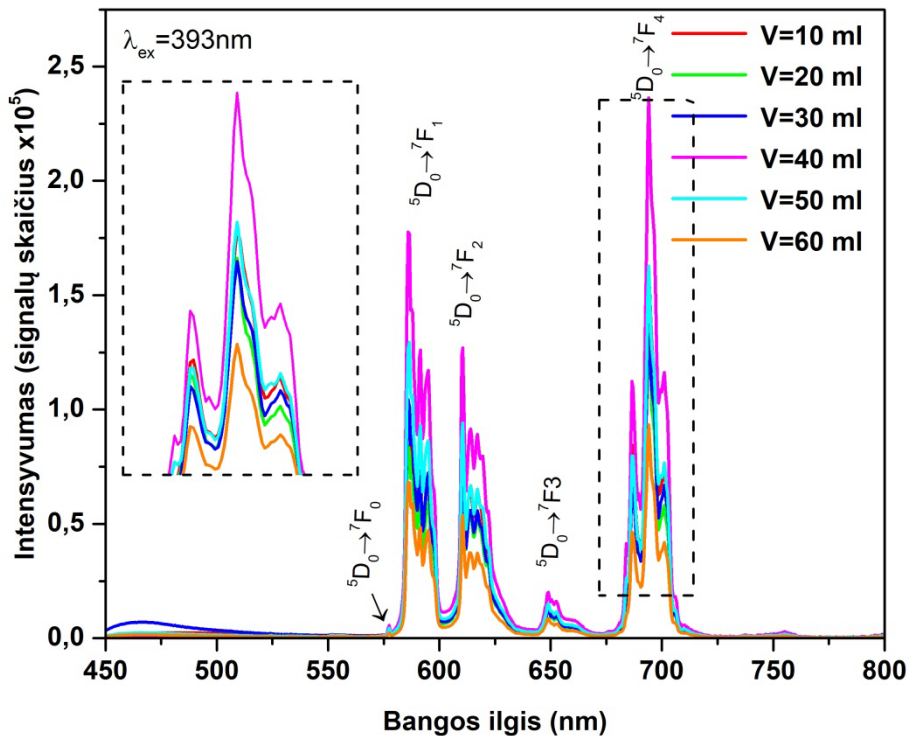
smailės priskiriamos Eu^{3+} jonui. Smailės ties 362 nm priskiriamos ${}^7\text{F}_0 \rightarrow {}^5\text{D}_4$ perėjimams. Diapazone nuo 370 nm iki 390 nm matoma kelių smailių grupė, kuri priskiriama ${}^7\text{F}_0 \rightarrow {}^5\text{L}_{7,8}$ ir ${}^7\text{F}_0 \rightarrow {}^5\text{G}_{2,4,5,6}$ perėjimams. Intensyviausia smailė ties 394 nm priskiriama perėjimui ${}^7\text{F}_0 \rightarrow {}^5\text{L}_6$. Mažos smailės ties 465 nm ir 527 nm priskiriamos atitinkamai ${}^7\text{F}_0 \rightarrow {}^5\text{D}_2$ ir ${}^7\text{F}_0 \rightarrow {}^5\text{D}_1$ perėjimams.



9 pav. $\text{Gd}_{0,85}\text{Eu}_{0,15}\text{PO}_4 \cdot \text{H}_2\text{O}$ mėginių, susintetintų naudojant skirtingus tirpiklio (H_2O) kiekius, sužadavimo spektrai.

Atliekant emisijos spektro matavimus, visi $\text{Gd}_{0,85}\text{Eu}_{0,15}\text{PO}_4 \cdot \text{H}_2\text{O}$ mėginiai buvo sužadinti $\lambda_{\text{ex}} = 393$ nm. Emisijos spektras rodo, kad gaunama spinduliuotė yra oranžinės ir raudonos spalvos diapazone. Emisijos spektro smailės yra ties ~ 577 nm, ~ 590 nm, ~ 615 nm, ~ 650 nm ir ~ 690 nm, atitinkamai priskiriamos ${}^5\text{D}_0 \rightarrow {}^7\text{F}_0$, ${}^5\text{D}_0 \rightarrow {}^7\text{F}_1$, ${}^5\text{D}_0 \rightarrow {}^7\text{F}_2$, ${}^5\text{D}_0 \rightarrow {}^7\text{F}_3$, ir ${}^5\text{D}_0 \rightarrow {}^7\text{F}_4$ perėjimams. Didžiausio intensyvumo smailė stebima ties 690 nm. Tai būdinga Eu^{3+} legiruotiems ortofosfatams. Literatūroje aprašyta, kad jei europio emisijos santykis ${}^5\text{D}_0 \rightarrow {}^7\text{F}_2 / {}^5\text{D}_0 \rightarrow {}^7\text{F}_1$ yra mažesnis arba lygus vienetui, tuomet yra aukštos simetrijos aplinka, ir atvirkščiai, kuo mažesnė simetrija, tuo didesnis santykis. Atlikti emisijų intensyvumo santykio skaičiavimai, kurių rezultatai pateikti 2 lentelėje. Duomenys patvirtina, kad

susintetinti mėginiai pasižymi aukšta simetrija. Taip pat apskaičiuota, kokią dalį emisijos sudaro ${}^5D_0 \rightarrow {}^7F_4$ (680-709 nm) elektronų šuoliai lyginant su visu emisijos ruožu (520-750 nm). Rezultatai taip pat pateikiami 2 lentelėje. Perėjimas ${}^5D_0 \rightarrow {}^7F_4$ yra dominuojantis, o apie 40% emisijos patenka į 680–709 nm juostą, kuri patenka į žmogaus kūno pralaidumo juostą.



10 pav. $Gd_{0,85}Eu_{0,15}PO_4 \cdot H_2O$ mėginių, susintetintų naudojant skirtingus tirpiklio (H_2O) kiekius, emisijos spektrai.

2 lentelė ${}^5D_0 \rightarrow {}^7F_2 / {}^5D_0 \rightarrow {}^7F_1$ emisijos smailės ir ${}^5D_0 \rightarrow {}^7F_4$ emisijos dalis procentais visame emisijos spektre.

Mėginys	${}^5D_0 \rightarrow {}^7F_2 / {}^5D_0 \rightarrow {}^7F_1$	${}^5D_0 \rightarrow {}^7F_4 /$ bendra emisija
V = 10 ml	1,0	40,6
V = 20 ml	1,0	40,6
V = 30 ml	0,9	38,3
V = 40 ml	0,8	40,3
V = 50 ml	0,8	38,4
V = 60 ml	0,9	38,3

3 lentelė Išmatuotas nanodalelių ilgio, pločio ir ilgio bei pločio santykis.

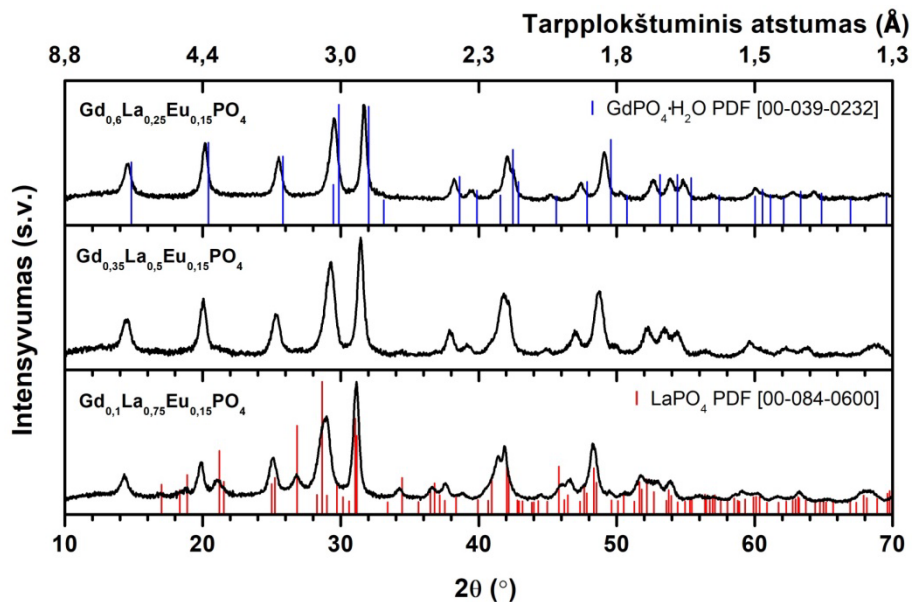
Mėginys	Ilgis, nm	Standartinis nuokrypis, nm	Plotis, nm	Standartinis nuokrypis, nm	Ilgio ir pločio santykis
V = 10 ml	194	71	58	14	3.3
V = 20 ml	835	268	103	28	8.1
V = 30 ml	455	157	178	64	2.6
V = 40 ml	658	276	224	104	2.9
V = 50 ml	1121	381	207	89	5.4
V = 60 ml	865	349	124	85	7.0

Mėginys, susintetintas, kai tūris $V = 40$ ml, pasižymi intensyviausia emisija. Apskaičiavus visų mėginių vidutines dalelių ilgio ir pločio reikšmes, gauta, kad tūryje $V = 40$ ml susintetintų dalelių plotis yra didžiausias 223 nm. Be to, taip pat buvo apskaičiuoti vidutiniai dalelių ilgio ir pločio santykiai visiems mėginiams, susintetintiems skirtingomis sąlygomis. Mažiausios santykio reikšmės (3 lentelė) (atitinkamai 2,6 ir 2,9) gautos mėginiams, susintetintiems, kai tūris $V = 30$ ml ir tūris $V = 40$ ml, o tai rodo, kad šių mėginių dalelių liuminescenciniai centrai yra labiau tūryje nei paviršiuje lyginant su kitais mėginiais.

Mėginių, susintetintų, kai tūris $V = 30$ ml ir $V = 50$ ml, emisijos intensyvumas yra beveik toks pat, nors skiriasi dalelių dydis ir ilgio bei pločio santykis. Apibendrinant galima teigti, kad yra, tarsi, konkurencija tarp dalelių dydžio (ilgio) ir ilgio ir pločio santykio, tačiau, tikėtina, plotis yra svarbiausias veiksnys. Mėginio, susintetinto $V = 40$ ml, dalelės demonstruoja optimalų tiriamų mėginių dydį ir geriausią santykio vertę, dėl kurios susidaro intensyviausia emisija.

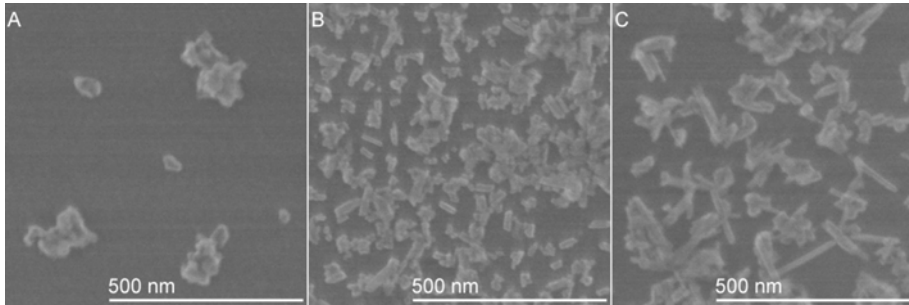
3. Legiravimo lantanu poveikis $Gd_{0,85-y}La_yPO_4:15\%Eu$ struktūrai ir liuminescencinėms savybėms

Siekiant dar labiau pagerinti liuminescencines savybes, mėginiai buvo papildomai legiruoti lantanu, tikintis stabilizuoti monoklininę struktūrą. Buvo paruošti trys skirtingi La legiruoti mėginiai, kuriuose būtų 25%, 50% ir 75% lantano. Gautų mėginių difraktogramos pavaizduotos 11 paveiksle.



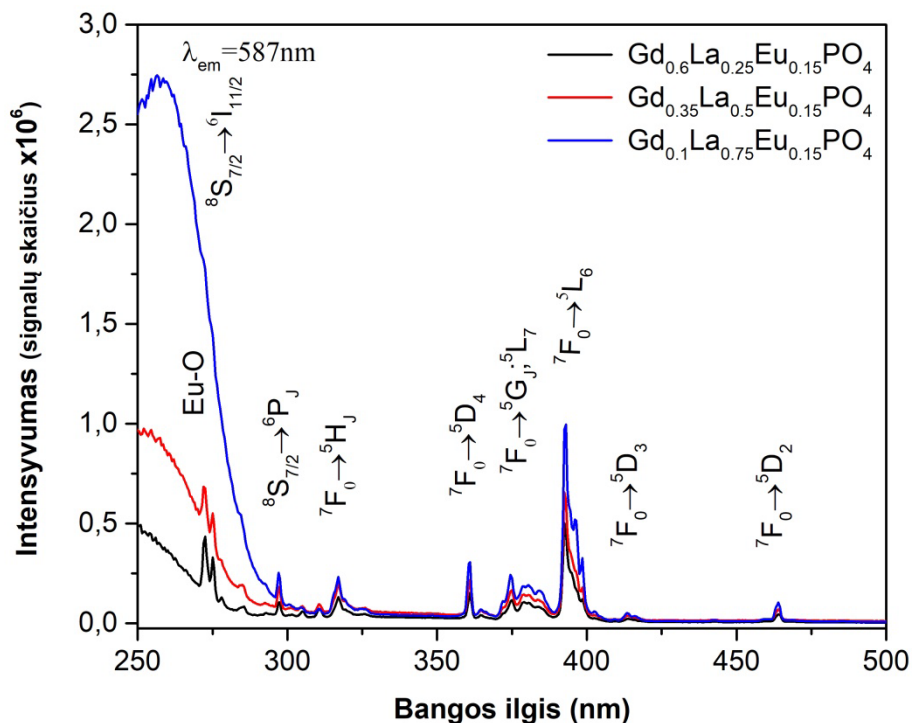
11 pav. $Gd_{0,85-y}La_yPO_4:15\%Eu$ mėginių, kuriuose yra skirtingas lantano kiekis, rentgeno spindulių difraktogramos.

Iš pateiktų rentgeno spindulių difraktogramų rezultatų matome, kad kai kurie susintetinti junginiai nėra vienfaziai, o dviejų skirtingų kristalinių fazių mišinys. $Gd_{0,1}La_{0,75}Eu_{0,15}PO_4$ mėginys yra dviejų monoklininės (PDF ICDD 00-084-0600) ir heksagoninės (PDF ICDD 00-039-0232) fazių mišinys. Sumažinus La ir atitinkamai padidinus Gd kiekį mėginyje, vis tiek turime dvifazį junginį. $Gd_{0,35}La_{0,5}Eu_{0,15}PO_4$ mėginyje, ties 21° , 27° ir 34° 2θ reikšmėmis, matomos papildomos mažos smailės, atitinkančios monoklininę kristalinę struktūrą. Sumažėjus La kiekiui iki 25% $Gd_{0,6}La_{0,25}Eu_{0,15}PO_4$ mėginyje, papildomų smailių neidentifikuota. Tai rodo vienfazės heksagoninės kristalinės fazės susidarymą. Smailių plotis nesikeičia. Tai rodo, kad lantano įvedimas neturi įtakos kristalitų dydžiui. SEM vaizdai pateikti 12 paveiksle. Matomos dalelių sanglaudos. Tam tikrose vietose taip pat galima rasti atskirų pavienių dalelių. Sulipusių ir atsiskyrusių dalelių dydis buvo matuojamas naudojant Fiji programinę įrangą. Vidutinis dalelių dydis $Gd_{0,6}La_{0,25}PO_4:15\%Eu$, $Gd_{0,35}La_{0,5}PO_4:15\%Eu$ ir $Gd_{0,1}La_{0,75}PO_4:15\%Eu$ yra atitinkamai 115 nm, 92 nm ir 122 nm. Visos atskiros dalelės yra nanostrypelio formos.



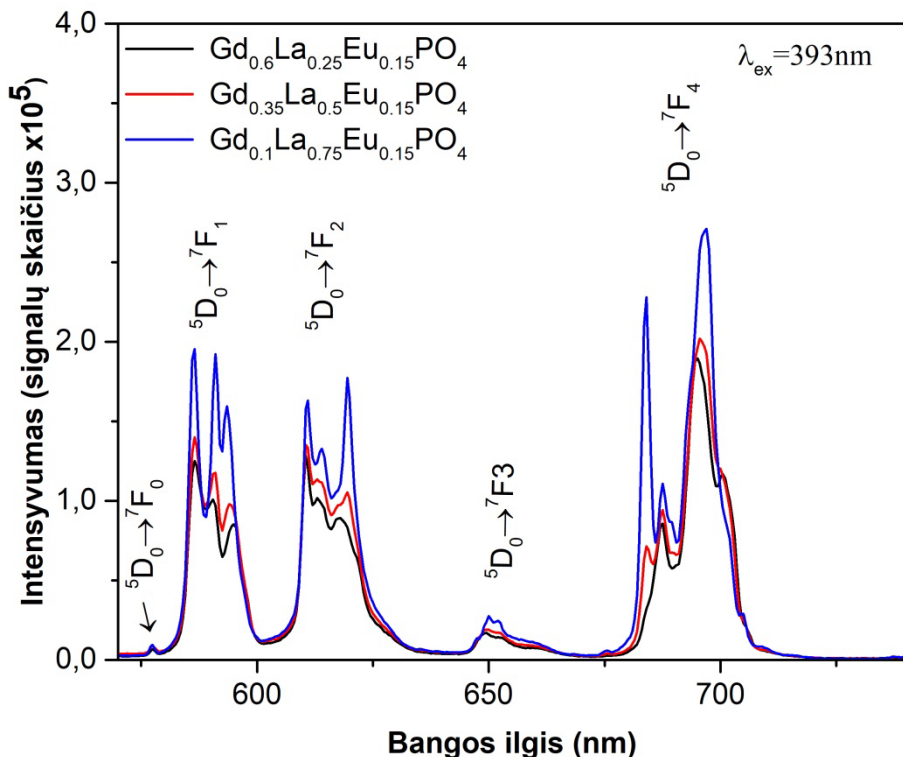
12 pav. (A) $\text{Gd}_{0,6}\text{La}_{0,25}\text{PO}_4:15\%\text{Eu}$, (B) $\text{Gd}_{0,35}\text{La}_{0,5}\text{PO}_4:15\%\text{Eu}$, (C) $\text{Gd}_{0,1}\text{La}_{0,75}\text{PO}_4:15\%\text{Eu}$ mėginių SEM vaizdai.

Taip pat buvo tiriamos $\text{Gd}_{0,85-y}\text{La}_y\text{PO}_4:15\%\text{Eu}$ mėginių liuminescencinės savybės. Sužadinimo spektrai buvo matuoti diapazone nuo 250 nm iki 500 nm, kai emisijos bangos ilgis $\lambda_{em} = 587$ nm (13 pav.). Sužadinimo spektruose yra plati juosta didesnės energijos srityje iki 270 nm. Taip yra dėl krūvio pernašos iš O^{2-} į Eu^{3+} jonus. Smailės, stebimos ties ~ 275 nm ir ~ 298 nm, priskiriamos Gd^{3+} jono ${}^8\text{S}_{7/2} \rightarrow {}^6\text{I}_{11/2}$ ir ${}^8\text{S}_{7/2} \rightarrow {}^6\text{P}_J$ perėjimams. Mėginio su mažiausiu Gd kiekiu ($\text{Gd}_{0,1}\text{La}_{0,75}\text{PO}_4:15\%\text{Eu}$) sužadinimo spektre smailės ties ~ 275 nm nesimato dėl intensyvios elektronų pernašos iš O^{2-} į Eu^{3+} . Gd^{3+} sužadinimo smailių buvimas sužadinimo spektruose, stebimuose Eu^{3+} jonui, įrodo vykstantį $\text{Gd}^{3+} \rightarrow \text{Eu}^{3+}$ energijos perdavimą. Likusios sužadinimo smailės priskiriamos Eu^{3+} jonui. Smailės ties ~ 318 nm priskiriamos ${}^7\text{F}_0 \rightarrow {}^5\text{H}_J$ perėjimams. Diapazone nuo ~ 360 nm iki ~ 400 nm matoma kelių smailių grupė, kuri priskirta ${}^7\text{F}_0 \rightarrow {}^5\text{D}_4$ ir ${}^7\text{F}_0 \rightarrow {}^5\text{G}_J$, ${}^7\text{F}_0 \rightarrow {}^5\text{G}_J$; ${}^5\text{L}_7$ perėjimams, atitinkamai. Intensyviausia smailė ties ~ 393 nm priskiriama ${}^7\text{F}_0 \rightarrow {}^5\text{L}_6$ perėjimui. Mažos smailės ties ~ 415 nm ir ~ 463 nm priskiriamos ${}^7\text{F}_0 \rightarrow {}^5\text{D}_3$, ${}^7\text{F}_0 \rightarrow {}^5\text{D}_2$ perėjimams.



13 pav. $Gd_{0,85-y}La_yPO_4:15\%Eu$ sužadavimo spektrai.

Taip pat buvo matuoti visų $Gd_{1-y}La_yPO_4:15\%Eu$ mėginių emisijos spektrai nuo 450 nm iki 800 nm. Junginiai buvo sužadinti 393 nm bangos ilgio šviesa, o oranžinės–raudonos spalvos emisijos rezultatai pateikti 14 paveiksle. Emisijos spektro smailės ties ~ 577 nm, ~ 590 nm, ~ 615 nm, ~ 650 nm ir ~ 690 nm atitinkamai priskiriamos ${}^5D_0 \rightarrow {}^7F_0$, ${}^5D_0 \rightarrow {}^7F_1$, ${}^5D_0 \rightarrow {}^7F_2$, ${}^5D_0 \rightarrow {}^7F_3$ ir ${}^5D_0 \rightarrow {}^7F_4$ elektronų perėjimams. Ties 577 nm matome labai intensyvią smailę. Esant 690 nm, stebime didžiausio intensyvumo smailę. Tai būdinga Eu^{3+} legiruotiems ortofosfatams.



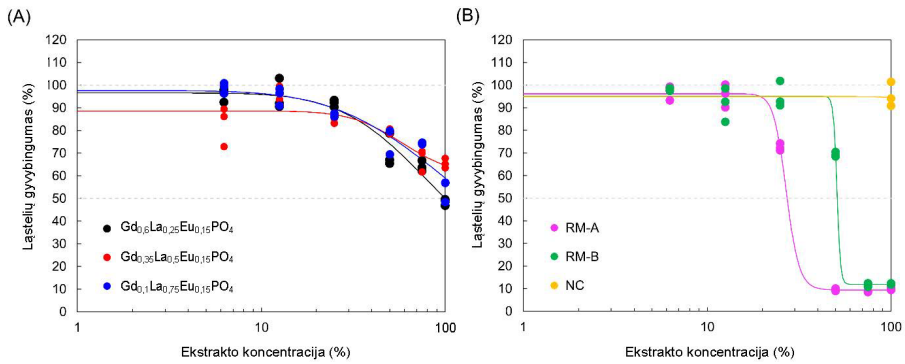
14 pav. $Gd_{0,85-y}La_yPO_4:15\%Eu$ mėginių emisijos spektrai.

4. $Gd_{0,85-y}La_yPO_4:15\%Eu$ mėginių biologinio suderinamumo įvertinimas

Citotoksiškumo bandymai reikalingi, nes naudojant nanomedžiagas biologiniam vaizdavimui ir ląstelių ženklinimui, gali būti naudojamos tik netoksiškos medžiagos. Buvo atliktas ląstelių gyvybingumo tyrimas, siekiant įvertinti, kokį poveikį ląstelėms daro $Gd_{0,85-y}La_yPO_4:15\%Eu$ mėginių ekstraktai.

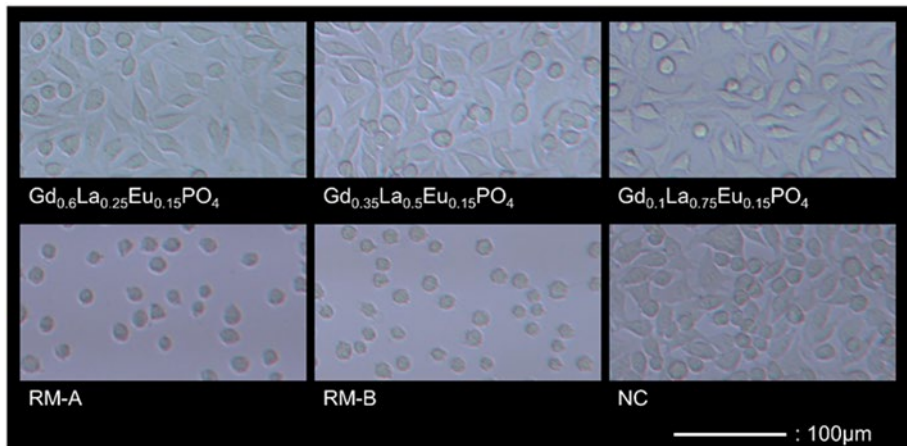
15 paveiksle pademonstruota, kad visuose mėginiuose ląstelių gyvybingumas sumažėjo didėjant ekstrakto koncentracijai. $Gd_{0,6}La_{0,25}PO_4:15\%Eu$ mėginyje gyvybingumo sumažėjimas buvo ryškesnis nei kituose dviejuose mėginiuose. Trijų kontrolinių mėginių ląstelių gyvybingumas buvo RM-A (toksiškas) < RM-B (mažiau toksiškas) < NC (netoksiškas), o tai atitiko kontrolinių mėginių citotoksiškumo tendenciją, todėl buvo nuspręsta, kad šis įvertinimas yra tinkamas. $Gd_{0,1}La_{0,75}PO_4:15\%Eu$ ir $Gd_{0,35}La_{0,5}PO_4:15\%Eu$ pademonstravo panašų citologinį suderinamumą su NC, įvertinus naudojamą IC50. Kita vertus, $Gd_{0,6}La_{0,25}PO_4:15\%Eu$, IC50, RM-A ir RM-B buvo atitinkamai 97,4%,

27,3% ir 51,1%. Tai reiškia, kad trijų mėginių citotoksiškumas buvo mažesnis nei RM-B, kurio citotoksiškumas buvo silpnas.



15 pav. Ląstelių gyvybingumas: (A) mėginiai, (B) kontrolė

16 paveiksle pavaizduoti visų 100% ekstrakto mėginių vaizdai gauti optiniu mikroskopu. RM-A ir RM-B kontroliniuose mėginiuose buvo matomos sferos formos ląstelės, ląstelės nebuvo prilipusios prie šulinėlių. O trijuose mėginiuose ir NC netoksiškame kontroliniame mėginyje matome, kad L929 ląstelės (pelių fibroblasų ląstelės) yra pailgos verpstės formos, kurių dydis buvo apie 100 μm , o ląstelės prilipusios prie šulinėlių. Šie vaizdai atitinka tipišką L929 atsaką į citotoksiškumą. Tai rodo, kad trys mėginiai buvo mažiau citotoksiški.

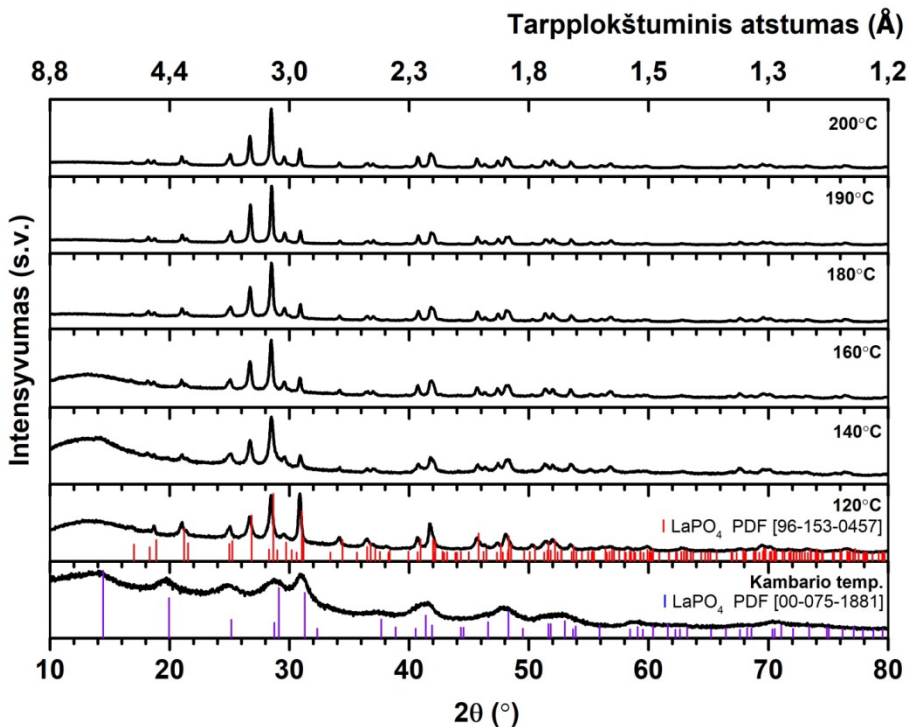


16 pav. L929 ląstelių optinės mikroskopijos vaizdai su 100% kiekvieno mėginio ekstraktu.

Šie citotoksiškumo tyrimai rodo, kad susintetinti ir išbandyti $Gd_{0,1}La_{0,75}PO_4:15\%Eu$ ir $Gd_{0,35}La_{0,5}PO_4:15\%Eu$ mėginiai yra netoksiški, o $Gd_{0,6}La_{0,25}PO_4:15\%Eu$ mėginys yra šiek tiek toksiškas.

5. Monoklininės struktūros $Gd_{0,85-y}La_yPO_4:15\%Eu$ sintezės sąlygų ir luminescencinių savybių tyrimas

Norint susintetinti monoklininės struktūros $Gd_{0,85-y}La_yPO_4:15\%Eu$, buvo nuspręsta išsiaiškinti $LaPO_4:1\%Eu$ sintezės sąlygas. Ekonominiais sumetimais nuspręsta $LaPO_4$ legiruoti 1 procentu Eu^{3+} . Visų pirma, buvo siekiama išsiaiškinti PO_4^{3-} jonų pirmtakų ir sintezės temperatūros įtaką $LaPO_4:1\%Eu$ struktūrai. Siekiant nustatyti hidroterminiame reaktoriuje susintetinto $LaPO_4:Eu$ kristalinę struktūrą ir įvertinti fazės grynumą buvo atlikta XRD analizė. Kai diamonio vandenilio fosfatas $(NH_4)_2HPO_4$ naudojamas kaip PO_4^{3-} jonų pirmtakas, 17 paveiksle matome, kad esant skirtingoms sintezės temperatūroms susidaro dvi $LaPO_4:1\%Eu$ kristalinės struktūros.



17 pav. $LaPO_4:1\%Eu$ mėginių, sintetintų naudojant $(NH_4)_2HPO_4$ ir esant skirtingomis sintezės temperatūromis, difraktogramos.

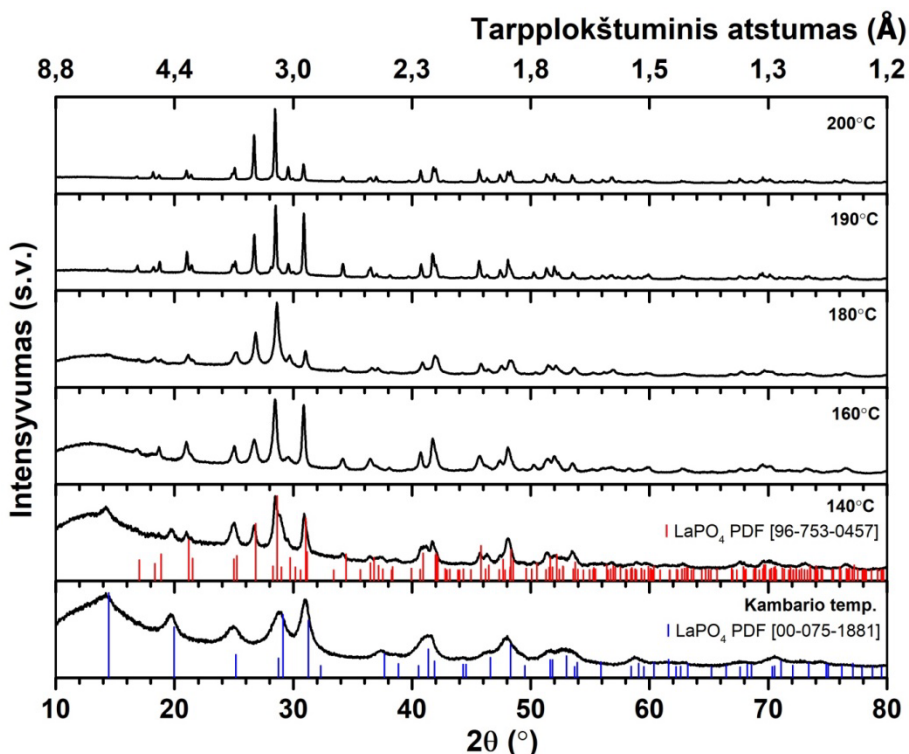
Analizuojant difraktogramas ir palyginus gautus duomenis su duomenų baze, matome, kad esant aukštesnei arba lygiai 160 °C sintezės temperatūrai eksperimentinių XRD duomenų smailės ir jų santykinis intensyvumas sutampa su duomenų bazės standartiniais monoklininės struktūros LaPO₄ smailėmis. (PDF ICCD 96-153-0457). Susidaro monoklininės kristalinės struktūros vienfazis LaPO₄:1%Eu. Esant žemesnei sintezės temperatūrai, 140 °C ir žemesnei, monoklininei fazei priskiriamos smailės vis dar dominuoja, tačiau yra stebimos smailės ties 14,4°, būdingos heksagoninei LaPO₄ kristalinei struktūrai (PDF ICCD 00-075-1881). Smailė esanti ties 28,6° kampu yra asimetriška ir išsiplečia link aukštesnių 2θ verčių, tai galima paaiškinti heksagoninės struktūros smaile esančia ties 29,1° kampu. Todėl galima teigti, kad susidaro dvifazė heksagoninė ir monoklininė LaPO₄ kristalinė struktūra. Tuo tarpu kambario temperatūroje gaunama mažo kristališkumo gryna heksagoninė fazė. Pažymėtina ir tai, kad kambario temperatūroje atliekama sintezė negali būti vadinama sinteze, atliekama hidroterminiame reaktoriuje, ją reikėtų vadinti nusodinimo reakcija.

Taip pat matoma plati juosta nuo 10° iki 20°. Jos kilmė gali būti siejama su pačios susintetintos medžiagos amorfiškumu arba amorfinio stiklo padėklo įtaka, ant kurio buvo dedama tiriamoji medžiaga. Kadangi atliekant XRD analizę visos medžiagos buvo paruoštos vienodai, difraktogramose matome, kad juosta nuo 10° iki 20° išnyksta, kai sintezės temperatūra yra aukštesnė nei 180 °C. Todėl labiau tikėtina, kad tai pačios medžiagos amorfiškumo įtaka. Apibendrinant galima teigti, kad net 120 °C temperatūra yra pakankama, kad būtų gauta dominuojanti kristalinė monoklininė LaPO₄:1%Eu fazė, tačiau gryna monoklininės kristalinės struktūros fazė gaunama tik esant 180 °C ir aukštesnėms temperatūroms, kai naudojamas diamonio vandenilio fosfatas ((NH₄)₂HPO₄) kaip PO₄³⁻ jonų pirmtakas.

Taip pat buvo atliekamos sintezės hidroterminiame reaktoriuje, naudojant amonio-divandenilio fosfatą (NH₄H₂PO₄) kaip PO₄³⁻ jonų pirmtaką. XRD analizės difraktogramos pateiktos 18 paveiksle. Difraktogramose matome, kad tik esant 200 °C sintezės temperatūrai gaunamas vienfazis monoklininės kristalinės struktūros LaPO₄:1%Eu. Šioje difraktogramoje papildomų smailių nėra. Esant žemesnei nei 200 °C sintezės temperatūrai mažo intensyvumo smailė, atitinkanti heksagoninę LaPO₄ kristalinę struktūrą (PDF ICCD 00-075-1881), matoma ties 14,4°, taip pat matome smailės asimetriją ties 29,1°.

Taigi, lyginant pirmosios serijos sintezės difraktogramas, kai diamonio vandenilio fosfatas buvo naudojamas kaip PO₄³⁻ jono pirmtakas, ir antrosios, kai amonio-divandenilio fosfatas buvo naudojamas kaip PO₄³⁻ jono pirmtakas, daroma išvada, kad jonų pirmtakas veikia temperatūrą kuriai

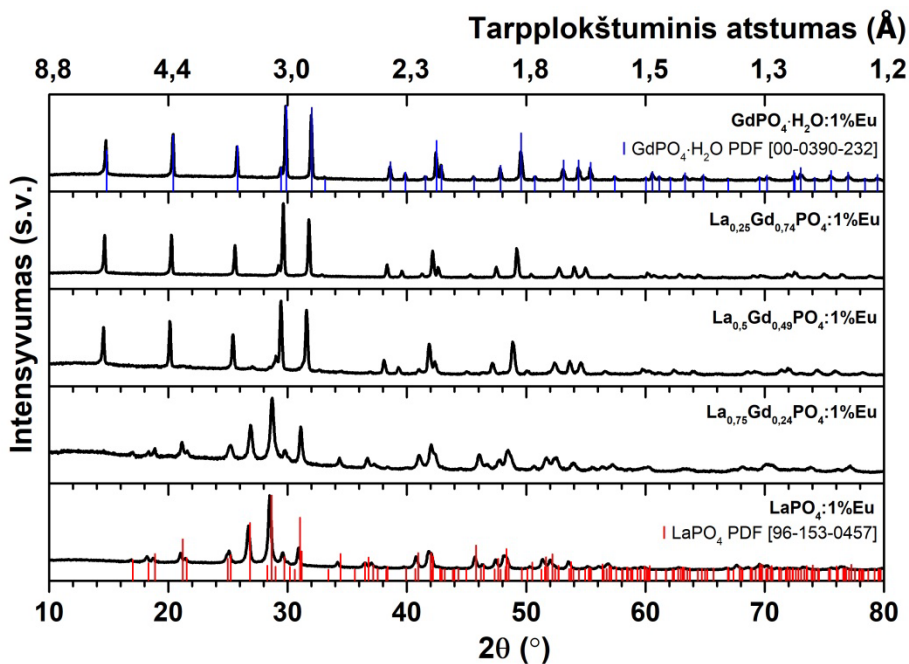
esant susidaro grynas monoklininės kristalinės struktūros galutinis susintetinto $\text{LaPO}_4:1\%\text{Eu}$ produktas. Naudojant $(\text{NH}_4)_2\text{HPO}_4$ gryna monoklininė fazė susidaro žemesnėje $180\text{ }^\circ\text{C}$ temperatūroje, o naudojant $\text{NH}_4\text{H}_2\text{PO}_4$ gryna monoklininė fazė susidaro tik esant $200\text{ }^\circ\text{C}$ sintezės temperatūrai, heksagoninės fazės priemaiša aiškiai matoma žemesnėje temperatūroje.



18 pav. $\text{LaPO}_4:1\%\text{Eu}$ mėginių, sintetintų naudojant $\text{NH}_4\text{H}_2\text{PO}_4$ ir esant skirtingomis sintezės temperatūromis, difraktogramos.

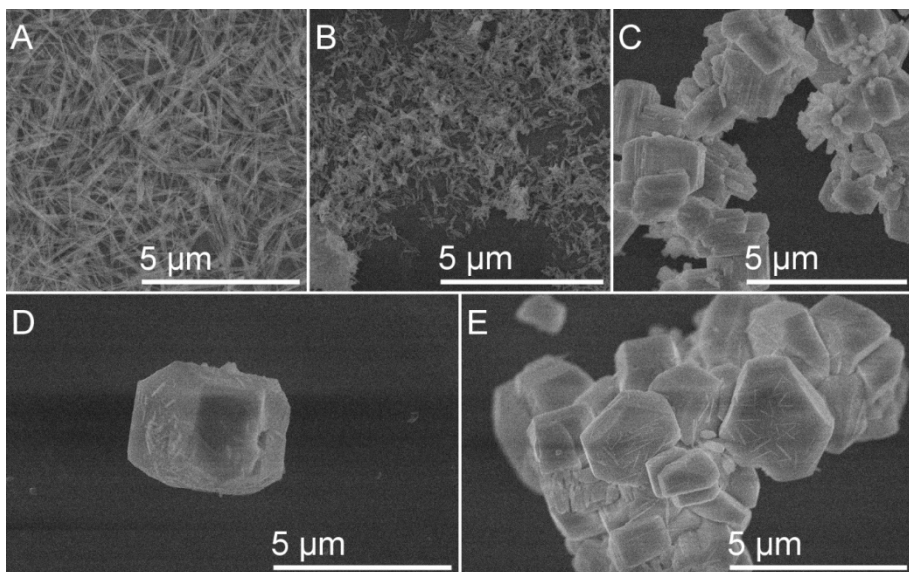
Remiantis šiais sintezės ir analizės rezultatais, nuspręsta tolesnei sintezei pasirinkti diamonio vandenilio fosfatą $(\text{NH}_4)_2\text{HPO}_4$ kaip PO_4^{3-} jonų pirmtaką ir atlikti hidroterminę sintezę $180\text{ }^\circ\text{C}$ temperatūroje, siekiant susintetinti monoklininės kristalinės struktūros dalelės. Buvo atlikta $\text{La}_x\text{Gd}_{1-x}\text{PO}_4:1\%\text{Eu}$ sintezių serija, kur $x = 1; 0,75; 0,5; 0,25; 0$. XRD analizės rezultatai pateikti 19 paveiksle. Iš difraktogramų matome, kad mėginių kai $x=0,5; 0,25, 0$ smailės atitinka heksagoninio gadolinio fosfato hidrato standarto (PDF ICDD 00-039-0232) duomenis. Tačiau $\text{La}_{0,75}\text{Gd}_{0,24}\text{PO}_4:1\%\text{Eu}$ ir $\text{LaPO}_4:1\%\text{Eu}$ difraktogramos atitinka monoklininio lantano fosfato standarto (PDF ICDD 96-153-0457) duomenis.

Nežymus fono linijos intensyvumo padidėjimas diapazone nuo 10° iki 20° , kai $x = 0,50$ ir $0,25$ rodo pačios susintetintos medžiagos amorfiškumą arba amorfinio stiklo padėklą, ant kurio buvo tiriama medžiaga, įtaką.



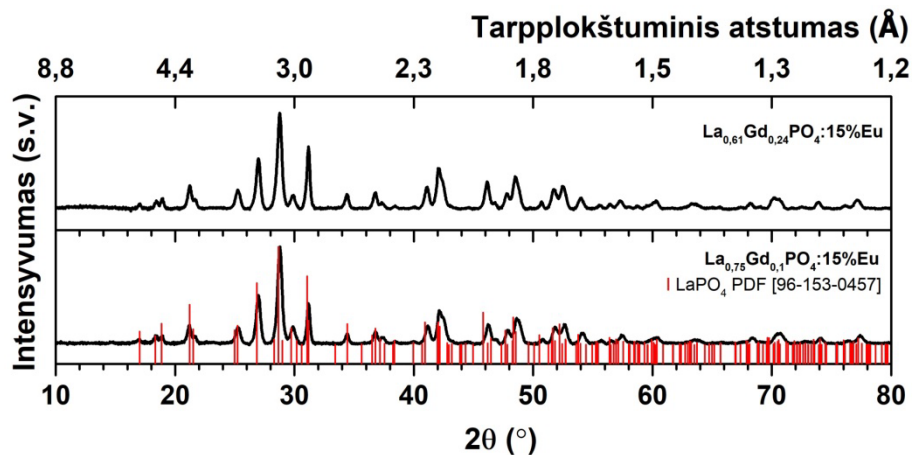
19 pav. $\text{La}_x\text{Gd}_{1-x}\text{PO}_4:1\% \text{Eu}$ mėginių difraktogramos

Šių sintezių metu gautos medžiagos taip pat buvo ištirtos SEM. Kaip matyti, susintetintų dalelių forma ir dydis kinta priklausomai nuo sudėties. $\text{LaPO}_4:1\% \text{Eu}$ (20 (A) pav.) dalelių struktūra yra gana vienoda, primenanti nanolazdeles, vidutinis dalelių ilgis 727 nm, o vidutinis plotis 80 nm. $\text{La}_{0,75}\text{Gd}_{0,24}\text{PO}_4:1\% \text{Eu}$ (20 (B) pav.) dalelės yra daug trumpesnės už anksčiau minėtas gryno lantano fosfato daleles, o vidutinis dalelių ilgis yra 216 nm, o vidutinis plotis yra 58 nm. Kai susintetintame fosfate gadolinio yra tiek pat arba daugiau nei lantano, dalelės praranda savo nanostrypelių formą ir tampa netaisyklingais, nevienodo dydžio, vientisais daugiakampiais, kurių jau nebegalima vadinti nanodalelėmis. Mikrostruktūros, kurių dydis siekia iki $5 \mu\text{m}$, SEM vaizdas pateiktas 20 (D) paveiksle, kur vidutinis dalelių ilgis yra $2,7 \mu\text{m}$, o 21E – $1,6 \mu\text{m}$.



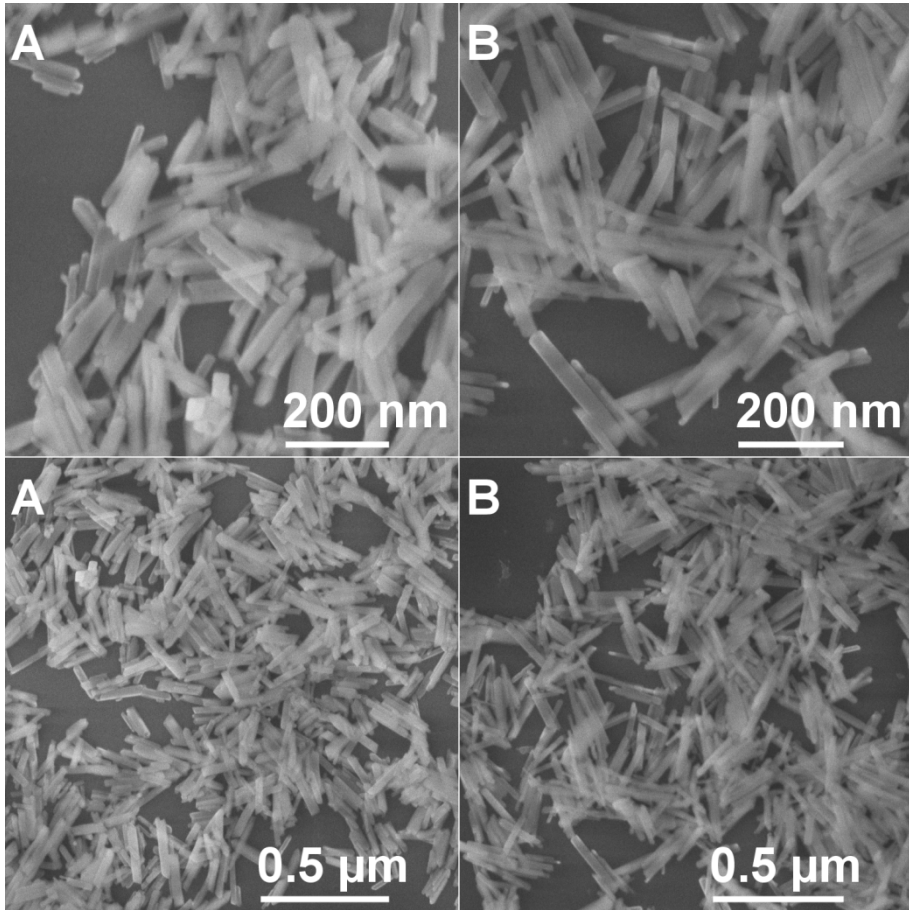
20 pav. $\text{La}_x\text{Gd}_{1-x}\text{PO}_4:1\%$ $x = 1$ (A); 0.75 (B); 0.5 (C); 0.25 (D); 0 (E); mėginių SEM vaizdai.

Remiantis 1 skyriuje atliktų tyrimų duomenimis, GdPO_4 emisija yra intensyviausia kai mėginys yra legiruotas 15% Eu^{3+} . Ir įvertinus anksčiau aprašytus sintezės ir analizės rezultatus, kai gaunamas vienfazis, monoklininės kristalinės struktūros $\text{La}_{0,75}\text{Gd}_{0,24}\text{PO}_4:1\%\text{Eu}$, buvo nuspręsta nuo 1% Eu^{3+} padidinti iki 15%, pakeičiant La arba Gd jonus. Buvo atlikti XRD tyrimai, siekiant įvertinti mėginio kristalinės struktūros fazinę sudėtį ir grynumą. Abiejų mėginių XRD difraktogramos pateiktos 21 paveiksle. Analizė pademonstravo, kad buvo gauti vienfaziai junginiai, nes mėginių difraktogramos atitinka monoklininio lantano fosfato (PDF ICDD 96-153-0457) duomenis.



21 pav. $\text{La}_{0.61}\text{Gd}_{0.24}\text{PO}_4:15\%\text{Eu}$ and $\text{La}_{0.75}\text{Gd}_{0.1}\text{PO}_4:15\%\text{Eu}$ mėginių difraktogramos

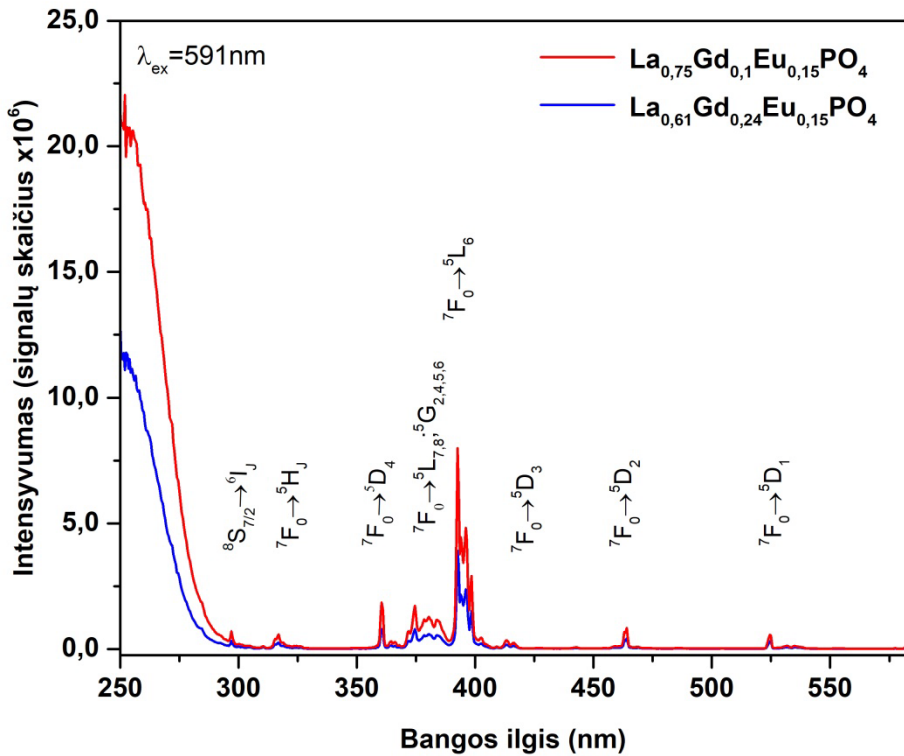
Siekiant ištirti hidroterminės sintezės būdu gautų medžiagų morfologiją ir dalelių dydį buvo atlikta SEM analizė. Abiem atvejais susintetintos nanolazdelių formos nanodalelės. Tačiau nė viename mėginyje dalelių ilgis ir storis nebuvo vienodi, kai kurios dalelės aglomeravosi viena prie kitos (22 pav.). $\text{La}_{0.75}\text{Gd}_{0.1}\text{PO}_4:15\%\text{Eu}$ mėginyje (A) susidariusios dalelės buvo šiek tiek trumpesnės ir storesnės, palyginus su $\text{La}_{0.61}\text{Gd}_{0.24}\text{PO}_4:15\%\text{Eu}$ mėginiu (B). $\text{La}_{0.75}\text{Gd}_{0.1}\text{PO}_4:15\%\text{Eu}$ dalelių ilgis svyruoja nuo 45 nm iki 150 nm. Dalelių storis svyruoja nuo 13 nm iki 35 nm, nematuoiant aglomeruotų dalelių. Susintetintų B mėginio dalelių ilgis yra nuo 120 nm iki 250 nm, o storis – nuo 10 nm iki 40 nm. Iš šių matavimų matome, kad A mėginyje susidariusios dalelės yra šiek tiek trumpesnės, palyginus su B mėginio dalelėmis, bet šiek tiek storesnės.



22 pav. $\text{La}_{0,61}\text{Gd}_{0,24}\text{PO}_4:15\%\text{Eu}$ ir $\text{La}_{0,75}\text{Gd}_{0,1}\text{PO}_4:15\%\text{Eu}$ SEM vaizdai.

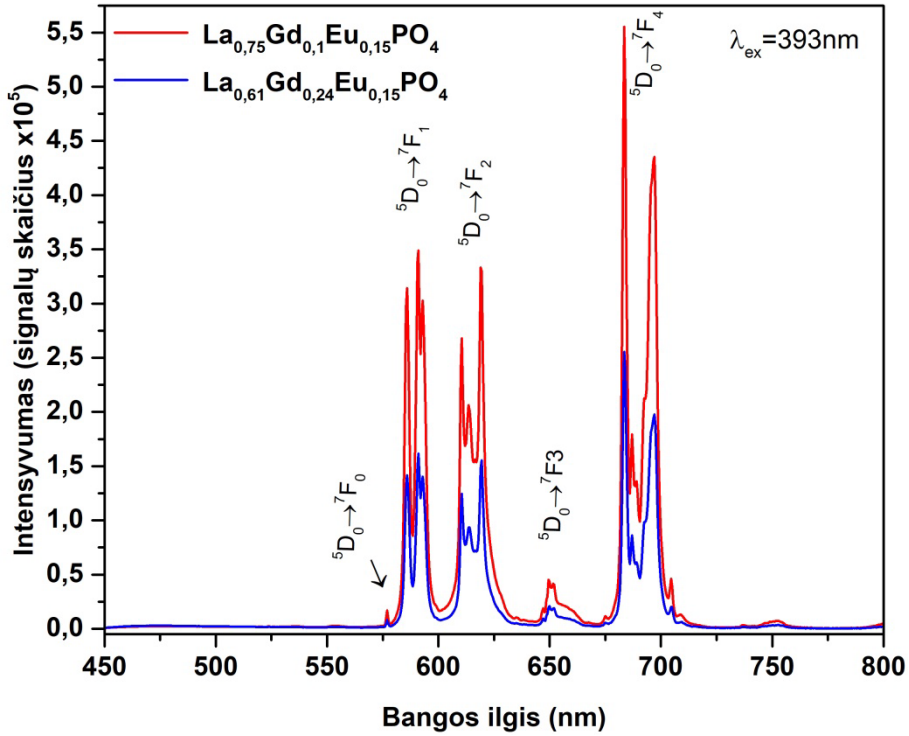
Ištirtos $\text{La}_{0,61}\text{Gd}_{0,24}\text{PO}_4:15\%\text{Eu}$ ir $\text{La}_{0,75}\text{Gd}_{0,1}\text{PO}_4:15\%\text{Eu}$ mėginių liuminescencinės savybės, pateiktos 23 ir 24 paveiksluose. Kadangi mėginiai baltos spalvos, tikimasi, kad jie turi minimalią absorbciją matomos šviesos spektre. Sužadinimo spektrai buvo matuojami nuo 250 nm iki 585 nm, kai emisijos bangos ilgis $\lambda_{\text{em}} = 591$ nm. Sužadinimo spektre matoma plati juosta, esanti nuo 250 nm iki 270 nm. Ji priskiriama krūvio pernašai, atsirandančiai dėl elektronų perėjimo iš O^{2-} į Eu^{3+} . Smailės ties ~ 298 nm priskirtos Gd^{3+} jono ${}^8\text{S}_{7/2} \rightarrow {}^6\text{P}_J$ elektronų perėjimams. Šių Gd^{3+} sužadinimo smailių buvimas sužadinimo spektruose, rodo $\text{Gd}^{3+} \rightarrow \text{Eu}^{3+}$ energijos pernašą. Likusios sužadinimo smailės buvo priskirtos Eu^{3+} jonams. Smailės ties ~ 318 nm susijusios su ${}^7\text{F}_0 \rightarrow {}^5\text{H}_J$ perėjimais, o 370 nm – 390 nm diapazone matomas kelių smailių klasteris, priskirtas ${}^7\text{F}_0 \rightarrow {}^5\text{D}_4$, ${}^7\text{F}_0 \rightarrow {}^5\text{G}_J$, ${}^7\text{F}_0 \rightarrow {}^5\text{G}_J$; ${}^5\text{L}_7$ perėjimams. Intensyviausia smailė ties 393 nm susijusi su ${}^7\text{F}_0 \rightarrow {}^5\text{L}_6$

perėjimu. Mažos smailės ties ~ 415 nm, ~ 463 nm ir ~ 527 nm buvo priskirtos atitinkamai ${}^7F_0 \rightarrow {}^5D_3$, ${}^7F_0 \rightarrow {}^5D_2$, ir ${}^7F_0 \rightarrow {}^5D_1$ perėjimams.



23 pav. $La_{0,61}Gd_{0,24}PO_4:15\%Eu$ ir $La_{0,75}Gd_{0,1}PO_4:15\%Eu$ sužadavimo spektrai.

$La_{0,61}Gd_{0,24}PO_4:15\%Eu$ ir $La_{0,75}Gd_{0,1}PO_4:15\%Eu$ mėginių liuminescencinės savybės buvo tiriamos juos sužadinant 393 nm bangos ilgiu ir išmatuojant jų emisijos spektrus. Nustatyta, kad skleidžiama spinduliuotė yra oranžinės-raudonos spalvos diapazone, o emisijos smailės buvo priskirtos įvairiems perėjimams tarp skirtingų Eu^{3+} jono energetinių lygmenų. Emisijos spektro smailės ties ~ 577 nm, ~ 590 nm, ~ 615 nm, ~ 650 nm ir ~ 690 nm priskiriamos atitinkamai ${}^5D_0 \rightarrow {}^7F_0$, ${}^5D_0 \rightarrow {}^7F_1$, ${}^5D_0 \rightarrow {}^7F_2$, ${}^5D_0 \rightarrow {}^7F_3$ ir ${}^5D_0 \rightarrow {}^7F_4$ perėjimams. Kaip ir buvo tikėtasi ir siekiama, $La_{0,75}Gd_{0,1}PO_4:15\%Eu$ emisijos intensyvumas yra žymiai didesnis ir siekia $5,5 \times 10^5$ signalų skaičių, palyginti su anksčiau susintetintais ir aptartais mėginiais su heksagonine kristaline struktūra, kur emisijos intensyvumo maksimumas yra $2,5 \times 10^5$ signalų.



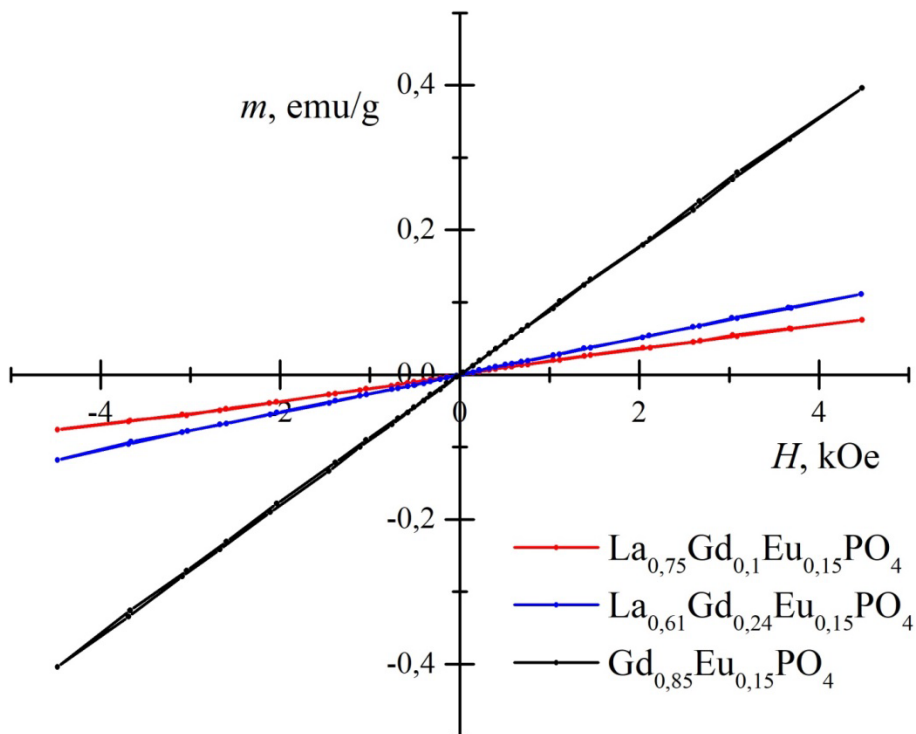
24 pav. $\text{La}_{0,61}\text{Gd}_{0,24}\text{PO}_4:15\%\text{Eu}$ ir $\text{La}_{0,75}\text{Gd}_{0,1}\text{PO}_4:15\%\text{Eu}$ emisijos spektrai.

Įmagnetinimo priklausomybė nuo taikomo magnetinio lauko stiprumo pateikta 25 paveiksle. Paramagnetikų įmagnetinimas yra proporcingas taikomo magnetinio lauko stiprumui $M=\chi H$, kur tūrio magnetinis jautrumas χ pagal Curie-Weiss dėsnį yra:

$$\chi = \frac{N}{3k_B} \cdot \frac{\mu_{eff}^2}{T+\Theta} \quad (1 \text{ lygt.})$$

N yra paramagnetinių atomų skaičius tūryje, k_B yra Boltzmanno konstanta, o Θ yra Veiso konstanta. Paramagnetinio atomo efektyvusis magnetinis momentas, kur J yra kampinio momento kvantinis skaičius, o μ_B yra Boro magnetonas. Nors pagrindinės būsenos Eu^{3+} $J = 0$, pirmoji sužadinta būsena yra artima jai kambario temperatūroje, todėl Eu^{3+} taip pat prisideda prie mėginių paramagnetizmo. Tačiau efektyvusis magnetinis momentas yra didesnis Gd^{3+} jonui, kai $J = 7/2$ ir faktorius $g = 2$. Nors magnetinis jautrumas taip pat priklauso nuo Weisso konstantos ir galimi tam tikri nukrypimai nuo Curie-Weiss dėsnio, kadangi GdPO_4 magnetinės tvarkos temperatūra $T_N = 225 \text{ K}$ yra gana artima kambario temperatūrai.

Mėginių jautrumo skirtumus daugiausia galima paaiškinti skirtingu Gd^{3+} kiekiu.



25 pav. Įmagnetinimo priklausomybė nuo magnetinio lauko stiprio kambario temperatūroje.

Visi trys tirti mėginiai pasižymėjo paramagnetinėmis savybėmis. Ir gali būti potencialiai naudojami kaip kontrastas magnetinio rezonanso tomografiją (MRT) tyrimuose. Tačiau remiantis mėginių liuminescencijos matavimus $La_{0.61}Gd_{0.24}PO_4:15\%Eu$ monoklininiai nanolazdelės pasižymi didžiausiu emisijos intensyvumu ir gali būti potencialiai naudojami multimodaliniam vaizdavimui, derinant magnetinio rezonanso tomografiją (MRT) ir liuminescencijos matavimus.

IŠVADOS

1. Dėl panašaus joninio spindulio gadolinis net iki 20% pakeičiamas europiu be reikšmingo poveikio heksagoninei kristalinei struktūrai. Be to, europio koncentracija neturi didelės įtakos susidariusių dalelių dydžiui, tačiau, skirtingai nei buvo pranešta mokslinėje literatūroje iki šiol, emisija yra intensyviausia, jei Eu^{3+} kiekis yra 15%. Viršijus europio kiekį, prasideda koncentracinis gesinimas.
2. $\text{Gd}_{0,85}\text{Eu}_{0,15}\text{PO}_4 \cdot \text{H}_2\text{O}$ nanodalelių dydis gali būti reguliuojamas keičiant hidroterminio reaktoriaus užpildymą skirtingu kiekiu tirpiklio (vandens). Gautos dalelės pasižymėjo strypelio formos morfologija, o jų dydis efektyviai kontroliuojamas.
3. Nanostrypelių liuminescencinėms savybėms turi įtakos dalelių dydis, ir ilgio bei pločio santykis. Tokiu būdu, pasirenkant reaktoriaus tūrio užpildymą, galima reguliuoti norimas liuminescencines savybes. $\text{Gd}_{0,85}\text{Eu}_{0,15}\text{PO}_4 \cdot \text{H}_2\text{O}$ mėginių emisijos intensyvumas didėja, kai yra daugiau europio jonų nanodalelės tūryje. Tyrimo metu buvo gautas optimalus dydis ir pločio bei ilgio dalelių santykis susintetintam mėginiui, kai tūris $V = 40$ ml.
4. PO_4^{3-} jonų pirmtako pasirinkimas reikšmingai paveikė $\text{LaPO}_4:1\%\text{Eu}$ kristalinę struktūrą. $(\text{NH}_4)_2\text{HPO}_4$ pirmtakas lėmė skirtingas kristalines struktūras žemesnėje temperatūroje, palyginus su $\text{NH}_4\text{H}_2\text{PO}_4$.
5. Didesnis lantano kiekis $\text{La}_x\text{Gd}_{1-x}\text{PO}_4:1\%\text{Eu}$ junginyje lemia monoklininės fazės susidarymą.
6. Padidinus Eu^{3+} kiekį iki 15% $\text{La}_{0,61}\text{Gd}_{0,24}\text{PO}_4:15\%\text{Eu}$ ir $\text{La}_{0,75}\text{Gd}_{0,1}\text{PO}_4:15\%\text{Eu}$ mėginiuose, pasireiškė sustiprinta liuminescencija. Emisijos spektrai pademonstravo ryškias smailes, atitinkančias Eu^{3+} elektronų perėjimus, o $\text{La}_{0,75}\text{Gd}_{0,1}\text{PO}_4:15\%\text{Eu}$ mėginiuose stebimas didesnis emisijos intensyvumas, lyginant su heksagoninės kristalinės struktūros analogais.
7. Įmagnetinimo tyrimai pademonstravo paramagnetinį susintetintų mėginių elgesį, veikiamą tiek Eu^{3+} tiek Gd^{3+} jonų.
8. $\text{La}_{0,61}\text{Gd}_{0,24}\text{PO}_4:15\%\text{Eu}$ monoklininės nanolazdelės pasižymi paramagnetinėmis savybėmis ir didžiausiu emisijos intensyvumu, todėl gali būti potencialiai naudojamos multimodaliniam vaizdavimui, derinant magnetinio rezonanso tomografiją (MRT) ir liuminescencijos matavimus.

ACKNOWLEDGEMENTS

I would like to extend my sincere gratitude and acknowledgments to the following individuals and entities for their invaluable contributions and support during my academic journey:

- Vilnius University and the Faculty of Chemistry and Geosciences for the exceptional opportunities they provided.
- The staff of the Department of Inorganic Chemistry for their camaraderie and unwavering assistance throughout my doctoral studies.
- The faculty and department administration for their unwavering professionalism and dedication to fostering a conducive academic environment.
- Professor Habil. Dr. Aivars Kareiva for his constructive guidance and pragmatic approach, which greatly enriched my research endeavors.
- Professor Dr. Ramūnas Skaudžius, my work supervisor, for his insightful advice and unwavering support in steering my academic pursuits.
- My laboratory colleagues, Andrius Pakalniškis, Greta Inkrataita, and Egle Buzaitytė, for their friendship, invaluable advice, and unwavering assistance throughout my academic journey.
- Professor Dr. Artūras Katelnikovas and Dr. Kęstutis Mažeika, whose guidance and support were instrumental in my practical acquisition of new research methodologies.
- My cherished friends, whose unwavering support and encouragement sustained me throughout the challenges of my PhD studies.
- Last but not least, my loving family, for their boundless patience and understanding during this demanding academic pursuit.

Your collective support and encouragement have been indispensable, and I am truly grateful for your presence in my life.

LIST OF PUBLICATIONS AND CONFERENCES PARTICIPATION

Articles in Journals

1. **Darius Budrevičius**, Ramūnas Skaudžius, „Volume dependence of the size of GdPO₄:15% Eu particles synthesized by the hydrothermal method“, Journal of Alloys and Compounds, 911 (2022) 164963. <https://doi.org/10.1016/j.jallcom.2022.164963>.
2. **Darius Budrevičius**, Noboru Kajimoto, Andrius Pakalniškis, Kanji Tsuru, Aivaras Kareiva, Ramūnas Skaudžius, „Improvement of luminescent properties of GdPO₄ doped with optimal europium concentration by Co-doping with lanthanum, Ceramics International. 49 (2023) 2373–2379. <https://doi.org/10.1016/j.ceramint.2022.09.209>.

Attended Conferences

1. **Darius Budrevičius**, Andrius Pakalniškis, Ramūnas Skaudžius, „The Dependence of the Morphology of GdPO₄ on the Synthesis Conditions“, Advanced Materials and Technologies 2020, Palanga, Lithuania, August 24-28 (2020).
2. **Darius Budrevičius**, Andrius Pakalniškis, Ramūnas Skaudžius, „The Dependence of the Morphology of GdPO₄ on the Synthesis Conditions“, Nanostructured Bioceramic Materials 2020 , Vilnius, Lithuania, December 1-3 24-28 (2020).
3. **Darius Budrevičius**, Ramūnas Skaudžius, „Synthesis of Controlled Size GdPO₄·H₂O Nanorods“, Advanced Materials and Technologies 2021, Palanga, Lithuania, August 23-27 (2020)..
4. **Darius Budrevičius**, Andrius Pakalniškis, Aivaras Kareiva, Ramūnas Skaudžius, „The Optimal Eu concentration for luminesces properties of GdPO₄“, Functional Inorganic Materials 2022, Vilnius, Lithuania, October 6-8 (2022).
5. **Darius Budrevičius**, Andrius Pakalniškis, Aivaras Kareiva, Ramūnas Skaudžius, „Improvement of Luminescent Properties of GdPO₄ Doped with Europium“, Chemistry and Chemical Technology 2023“, Vilnius, Lithuania, March 10 (2023).

CURRICULUM VITAE

Personal Information	
Name, Surname	Darius Budrevičius
Data of birth	1978 October 16
E-mail	Darius.budrevicius@gmail.com

Education	
2018 – to present	Doctoral studies, Department of Inorganic Chemistry Institute of Chemistry, Faculty of Chemistry and Geoscience, Vilnius University
2007 – 2008	Additional courses in Management and Business Administration, Faculty of Economics, Vilnius University
2001 – 2006	Master's degree in Materials Science, Faculty of Physics, Vilnius University
1997 – 2001	Bachelor of Physics, Faculty of Physics, Vilnius University

Work experience	
2018 – to present	“Sanovus” UAB, Service manager
2013 – 2018	“Laisva linija” UAB, Service manager
2002 – 2013	“Laisva linija” UAB, Service engineer

Vilniaus universiteto leidykla
Saulėtekio al. 9, III rūmai, LT-10222 Vilnius
El. p. info@leidykla.vu.lt, www.leidykla.vu.lt
bookshop.vu.lt, journals.vu.lt
Tiražas 10 egz.